



**HAL**  
open science

# Numerical and experimental analysis of flows generated by temperature fields in rarefied gas: application to the design of Knudsen micropumps

Jie Chen

► **To cite this version:**

Jie Chen. Numerical and experimental analysis of flows generated by temperature fields in rarefied gas: application to the design of Knudsen micropumps. Fluid mechanics [physics.class-ph]. INSA de Toulouse, 2016. English. NNT : 2016ISAT0009 . tel-01511683

**HAL Id: tel-01511683**

**<https://theses.hal.science/tel-01511683>**

Submitted on 21 Apr 2017

**HAL** is a multi-disciplinary open access archive for the deposit and dissemination of scientific research documents, whether they are published or not. The documents may come from teaching and research institutions in France or abroad, or from public or private research centers.

L'archive ouverte pluridisciplinaire **HAL**, est destinée au dépôt et à la diffusion de documents scientifiques de niveau recherche, publiés ou non, émanant des établissements d'enseignement et de recherche français ou étrangers, des laboratoires publics ou privés.

Université Fédérale



Toulouse Midi-Pyrénées

# THÈSE

En vue de l'obtention du

## DOCTORAT DE L'UNIVERSITÉ DE TOULOUSE

**Délivré par** Institut National des Sciences Appliquées de Toulouse (INSA de Toulouse)

**Discipline ou spécialité :** *Énergétique et transferts*

---

**Présentée et soutenue par** *Jie CHEN*

**Le** *lundi 21 mars 2016*

**Titre :**

Numerical and experimental analysis of flows generated by temperature fields  
in rarefied gas: application to the design of Knudsen micropumps

---

### JURY

*Aldo FREZZOTTI, Professeur à l'École Polytechnique de Milan, Rapporteur*

*Gian Luca MORINI, Professeur à l'Université de Bologne, Rapporteur*

*Stéphane COLIN, Professeur à l'INSA de Toulouse, Examineur*

*Lucien BALDAS, Maître de conférences, HDR à l'INSA de Toulouse, Examineur*

*Juergen BRANDNER, Professeur à Karlsruhe Institute of Technology, Examineur*

*Irina GRAUR, Professeur à Université d'Aix-Marseille, Examineur*

*Stefan KANCHEV STEFANOV, Professeur à Bulgarian Academy of Sciences, Examineur*

---

**Ecole doctorale :** *MEGEP*

**Unité de recherche :** *Institut Clément Ader*

**Directeur(s) de Thèse :** *Stéphane COLIN et Lucien BALDAS*



“学而不思则罔，思而不学则殆”

——《论语·为政》

*Learning without thought is labour lost,  
thought without learning is perilous.*

——Confucius



# Acknowledgements

I would like to gratefully and sincerely thank my supervisors, Stephane Colin and Lucien Baldas, for their guidance, patience and continuous support of my Ph.D research in INSA Toulouse. Besides being a preeminent researcher in microfluidics, Prof. Stephane Colin is also an excellent advisor, who gave me the opportunity to fully develop my individuality. Associate Prof. Lucien Baldas, outstanding researcher in flow control research field, also gave me great suggestions on my topic. They gave me advices and help in a lot of aspects, from living in France to doing research. I benefited from my supervisors not only in their immense scientific knowledge, but also rigorous scholarship and modesty. I feel very honored and lucky to do my Ph.D research under their supervision. I am also very grateful to professor Stefan K Stefanov for his help and guidance on direct simulation Monte Carlo.

I would like to thank the defense committee: Prof. Aldo Frezzotti, Prof. Gian Luca Morini, Prof. Stefan K Stefanov, Prof. Juergen Brandner, Prof. Irina Graur, for their encouragement, insightful comments, and interesting questions.

I would also like to thank all of the members of the group of microfluidics and they gave me lots of help during my Ph.D study. I am very grateful to Marcos Rojas-Cardenas and Christine Barrot for very useful discussions and technical advices on experiments. I would like to give my special thanks to Nicolas Laurien for helping with the construction of the new experimental set-up. I also thank Pascale Magaud, Hacene Si Hadj Mohand, Dominique Fratantonio, Ernane Silva for interesting talks on science and nature in those coffee breaks.

I would also like to thank the members of Institut Clément Ader and Ecole Doctorale MEGeP. I enjoyed my research experiences at Institut Clément Ader with those outstanding researchers. Additionally, I am very grateful for the friendship with other Ph.D students in my laboratory, especially Hacene Si Hadj Mohand, Jean-Emmanuel Chambe, Ksentini Olfa, Shiqi Wang, Jian Fu, Yiwei Wang, Yanfeng Gao, Donghai Qiu and Tao Li.

I acknowledge the scholarship of China Scholarship Council (CSC) which awarded a scholarship for my studies in France.

Most importantly, I would like to thank my husband, my parents and his parents. Their love, support and encouragement provide me endless power and energy to pursue my scientific dream.

# Abstract

This thesis presents a numerical and experimental analysis of internal rarefied gas flows induced by temperature fields. In rarefied gases, a flow can be generated by solely applying a tangential temperature gradient along a wall: without any initial pressure gradient, the gas macroscopically moves from the cold toward the hot region. This phenomenon is the so-called thermal creep or thermal transpiration effect. It is the main operating principle of the Knudsen pump, which can generate gas pumping without the need of any moving parts. The main aspect of this work is centered on numerical investigations of thermal transpiration flows in three new possible configurations of Knudsen pumps. For that goal, a numerical model for slip flows has been developed in which the appropriate slip boundary conditions are implemented in a commercial CFD code and a DSMC code has been adapted for studying transition flows in complex geometries. The pumping effect of curved-channel Knudsen pumps, the thermal transpiration flows through tapered channels and between two ratchets surfaces at different uniform temperatures have been investigated. In addition, an experimental study of thermal transpiration flow through a single micro-tube has been carried out on a new experimental set-up designed to be adaptable for testing thermally driven flows through various kinds of microchannels or generated by autonomous Knudsen compressors.

**Keywords:** Microfluidics, gas microflows, thermal transpiration, Knudsen pump, CFD, DSMC



# Résumé long en français

Cette thèse présente une étude numérique et expérimentale d'écoulements gazeux raréfiés confinés induits par gradients thermiques ainsi que trois nouvelles configurations de pompe Knudsen.

En raison de la tendance à la miniaturisation des systèmes électromécaniques, des micropompes à gaz sont nécessaires notamment pour une large gamme de microsystèmes de détection et d'analyse, tels que les nez électroniques, les spectromètres de masse ou encore les chromatographes en phase gazeuse (Pham-Van-Diep et al. 1995). L'une des pompes à vide miniaturisées les plus attrayantes est la pompe Knudsen qui fonctionne sur le principe de la transpiration thermique (Vargo et al. 1999). Après avoir analysé divers microsystèmes impliquant des écoulements gazeux confinés, il apparaît clairement que les effets de raréfaction qui résultent de la réduction de taille de l'appareil ne peuvent pas, dans presque tous les cas, être négligés (Colin 2013). L'un des paramètres les plus couramment utilisés pour caractériser le niveau de raréfaction est le nombre de Knudsen qui est défini par le rapport du libre parcours moyen des molécules de gaz (c'est-à-dire la distance moyenne parcourue entre deux collisions successives) à une longueur interne caractéristique du système. Le nombre de Knudsen permet une classification des régimes d'écoulement gazeux. En général, quatre régimes d'écoulement gazeux sont considérés : le régime continu, le régime d'écoulement glissant, le régime de transition et le régime moléculaire libre. Des modèles appropriés doivent être choisis en fonction du régime d'écoulement rencontré.

L'écoulement d'un gaz raréfié peut être généré simplement en appliquant un gradient tangentiel de température le long d'une paroi. Ainsi, sans gradient initial de pression, le gaz peut se déplacer de la région froide vers la région chaude. Ce phénomène, appelé transpiration thermique, est à la base du fonctionnement de la pompe Knudsen qui est capable de générer un pompage du gaz sans utiliser de pièces mécaniques mobiles. Plusieurs modèles différents de pompes Knudsen ont été étudiés au cours des dernières années, à la suite du travail fondateur de Knudsen lui-même (Knudsen 1909). La pompe Knudsen typique est basée sur un système en cascade dans lequel une unité de base se compose d'un micro-canal (McNamara et al. 2005, Gupta et al. 2012, An et al. 2014) ou d'un milieu microporeux (Han et al. 2007, Gupta et al. 2011) reliant deux mini chambres à températures différentes. D'autres configurations ont été proposées et étudiées numériquement,

comprenant des micro-canaux courbes et rectilignes connectés en alternance (Aoki et al. 2009) ou des micro-canaux courbes ayant des rayons différents (Bond et al. 2016). Dans ces conceptions cependant, la difficulté pratique principale provient de la nécessité de contrôler précisément le gradient de température le long des parois.

L'apport principal de ce travail est relatif à l'étude numérique de l'écoulement de transpiration thermique dans trois nouvelles configurations de pompe Knudsen.

Dans ce but, une méthode numérique pour la simulation d'écoulements dans le régime de glissement a été développée ; elle implémente des conditions aux limites de saut de vitesse et de température spécifiques à l'aide de "User Defined Functions" (UDF), dans un code CFD commercial. Par rapport aux méthodes cinétiques ou aux simulations de type Monte-Carlo (DSMC), ce modèle a un coût de calcul largement réduit, ce qui facilite la conception et l'optimisation des pompes, du point de vue de la géométrie et des conditions de fonctionnement. Parallèlement, un code DSMC a été mis en œuvre pour étudier des écoulements plus fortement raréfiés dans les géométries les plus complexes. Grâce à ces modèles numériques, des écoulements de transpiration thermique générés dans des canaux courbes, dans des canaux convergents/divergents ou entre deux surfaces spécialement micro-texturées ont ainsi été étudiés.

Les simulations numériques ont montré qu'une pompe Knudsen à plusieurs étages constitués de canaux courbes et droits en alternance peut être efficace dans le régime d'écoulement glissant. Une analyse paramétrique menée sur un étage unique de cette pompe Knudsen a permis d'élaborer des lignes directrices pour améliorer l'efficacité de la pompe qui doit avoir une partie semi-circulaire de forte courbure et devrait fonctionner sous une différence de température élevée et dans des conditions de raréfaction assez fortes. Un premier prototype d'une pompe Knudsen de ce type à l'échelle millimétrique, comprenant 50 étages, a été conçu et fabriqué à l'Institut de Technologie de Karlsruhe (KIT) et ses performances ont été estimées numériquement sur la base d'une configuration 2D simplifiée. Ce prototype sera examiné expérimentalement dans le futur à l'aide d'un nouveau banc expérimental lorsque les problèmes d'étanchéité au niveau de la structure et des raccords auront été résolus.

L'analyse des écoulements de transpiration thermique dans des canaux coniques a montré qu'un effet diode existe dans les canaux divergents / convergents soumis à un gradient de température.

Dans les mêmes conditions de pression et de gradient thermique, le canal convergent génère une différence de pression plus grande que celle générée par le canal divergent. L'étude numérique démontre également la possibilité de concevoir une pompe Knudsen à base de canaux coniques en profitant de cet effet diode. Par rapport aux modèles classiques, cette pompe Knudsen présente plusieurs avantages importants en termes de conception et de contrôle des contraintes thermiques.

Une nouvelle configuration de pompe Knudsen, qui ne nécessite que des parois isothermes, chaudes ou froides, et qui par conséquent est beaucoup plus facile à contrôler thermiquement qu'une pompe classique nécessitant un gradient de température le long d'une surface, a été étudiée par des simulations CFD basées sur l'approche continue ainsi que par des calculs DSMC. L'élément de pompage est constitué de deux surfaces en dents de scie asymétriques, isothermes et à températures différentes, se faisant face. Un débit massique net a été observé et le fonctionnement de ce nouveau type de pompe Knudsen a été prouvé numériquement. L'influence des principaux paramètres géométriques et des conditions de fonctionnement, comme le nombre de Knudsen et la différence de température, a été étudiée et des lignes directrices pour la conception d'un prototype ont été élaborées.

D'autre part, un nouveau dispositif expérimental a été conçu pour l'étude des écoulements de transpiration thermique dans différents types de micro-canaux ainsi que pour le test de micro-pompes Knudsen. Les premières données expérimentales obtenues pour un écoulement de transpiration thermique dans un micro-tube ont été comparées avec succès, pour un petit nombre de Knudsen, à un modèle théorique d'écoulement glissant, ce qui a permis la validation du banc d'essais.

**Mots-Clés :** Microfluidique, micro-écoulements gazeux, transpiration thermique, pompe Knudsen, CFD, DSMC

**Références :**

An, S., Gupta, N. K. and Gianchandani, Y. B. (2014). "A Si-micromachined 162-stage two-part Knudsen pump for on-chip vacuum." *Journal of Microelectromechanical Systems* 23(2): 406-416.

- Aoki, K., Degond, P. and Mieussens, L. (2009). "Numerical simulations of rarefied gases in curved channels: thermal creep, circulating flow, and pumping effect." *Communications in Computational Physics* 6(5): 911-954.
- Bond, D. M., Wheatley, V. and Goldsworthy, M. (2016). "Numerical investigation into the performance of alternative Knudsen pump designs." *International Journal of Heat and Mass Transfer* 93: 1038-1058.
- Colin, S. (2013). *Single-phase gas flow in microchannels. Heat transfer and fluid flow in minichannels and microchannels*, Elsevier: 11-102.
- Gupta, N. K., An, S. and Gianchandani, Y. B. (2012). "A Si-micromachined 48-stage Knudsen pump for on-chip vacuum." *Journal of Micromechanics and Microengineering* 22(10): 105026.
- Gupta, N. K. and Gianchandani, Y. B. (2011). "Porous ceramics for multistage Knudsen micropumps—modeling approach and experimental evaluation." *Journal of Micromechanics and Microengineering* 21(9): 095029.
- Han, Y.-L., Phillip Muntz, E., Alexeenko, A., et al. (2007). "Experimental and Computational Studies of Temperature Gradient-Driven Molecular Transport in Gas Flows through Nano/Microscale Channels." *Nanoscale and Microscale Thermophysical Engineering* 11(1-2): 151-175.
- Knudsen, M. (1909). "Eine Revision der Gleichgewichtsbedingung der Gase. Thermische Molekularströmung." *Annalen der Physik* 336(1): 205-229.
- McNamara, S. and Gianchandani, Y. B. (2005). "On-Chip Vacuum Generated by a Micromachined Knudsen Pump." *Microelectromechanical Systems, Journal of* 14(4): 741-746.
- Pham-Van-Diep, G., Keeley, P., Muntz, E. P., et al. (1995). "A micromechanical Knudsen compressor." *Rarefied gas dynamics* 1: 715-721.
- Vargo, S., Muntz, E. and Tang, W. (1999). *The MEMS Knudsen Compressor as a Vacuum Pump for Space Exploration Applications. 2nd International Conference on Integrated Micro/Nanotechnology for Space Applications. Pasadena, California, USA.*

# Contents

<b>Nomenclature</b> .....	i
<b>Introduction</b> .....	1
<b>Chapter 1 Thermal transpiration flows and Knudsen pumps</b> .....	5
1.1. Thermal transpiration flow .....	5
1.1.1. Fundamental demonstration of flow induced by temperature fields .....	7
1.1.2. Quantitative measurements on thermal transpiration flow .....	9
1.1.3. Analytical and numerical investigations .....	14
1.2. Knudsen pumps.....	15
1.2.1. Knudsen pumps with nanoporous materials .....	15
1.2.2. Knudsen pumps with micromachined channels .....	17
1.2.3. Knudsen pumps in laboratory conditions and experimental set-ups....	18
References .....	21
<b>Chapter 2 Modeling of thermal transpiration flow</b> .....	25
2.1. General points about gas microflows modeling.....	25
2.1.1. The simple dilute gas .....	25
2.1.2. Molecular collision models.....	26
2.1.3. Thermodynamic equilibrium .....	30
2.1.4. Gas flow regimes and main models.....	30
2.2. Slip flow regime.....	31
2.2.1. Boundary conditions .....	31
2.2.2. Analytical method .....	34
2.2.3. Numerical method .....	37
2.3. Transitional regime - DSMC simulation.....	45
2.3.1. DSMC simulation.....	45
2.3.2. dsmcFoamStrath.....	46

2.3.3. DSMC with decomposition of the solution into ballistic and collision parts.....	46
2.3.4. Validation: thermally-driven flow in a closed rectangular channel .....	48
2.4. Summary .....	50
References .....	50
<b>Chapter3 Thermal transpiration flow in tapered channels.....</b>	<b>53</b>
3.1. Introduction.....	53
3.2. Isothermal flow .....	55
3.3. Thermal transpiration flow .....	57
3.3.1. Mass flowrate at constant pressure (open reservoir configuration) ....	59
3.3.2. Pressure difference at zero mass flowrate (closed reservoir configuration at equilibrium).....	61
3.3.3. Tapered-channel Knudsen pump.....	65
3.4. Summary .....	68
References .....	68
<b>Chapter 4 Curved-channel Knudsen pumps.....</b>	<b>71</b>
4.1. Introduction.....	71
4.2. Numerical design .....	73
4.2.1. Simulation of multi-stage pumps .....	73
4.2.2. Parametric analysis of a single-stage micropump .....	76
4.3. A prototype of serpentine Knudsen pump .....	85
4.3.1. Description of the pump system.....	85
4.3.2. Numerical estimation of performance.....	86
4.4. Summary .....	91
References .....	91
<b>Chapter 5 Ratchet Knudsen pumps</b>	
5.1. Introduction.....	93
5.2. Study in the slip flow regime .....	96
5.2.1. Problem statement.....	96
5.2.2. Influence of the mesh on the calculations accuracy .....	97

5.2.3. Comparison of the three configurations .....	99
5.2.4. Parameter analysis.....	101
5.3. DSMC Simulation.....	107
5.3.1. Problem statement .....	107
5.3.2. Reference configuration .....	108
5.3.3. Temperature distribution and flow characteristics .....	109
5.3.4. Influence of the Knudsen number.....	112
5.3.5. Influence of the accommodation coefficients .....	116
5.3.6. Influence of geometric parameters .....	118
5.3.7. Decomposition solution into ballistic and collision parts .....	121
5.4. Summary .....	123
References .....	124
<b>Chapter6 Experimental study of thermal transpiration flow through a microtube.....</b>	<b>127</b>
6.1. Description of the experiment set-up.....	127
6.1.1. Test section.....	128
6.1.2. Measurement ring.....	129
6.1.3. Temperature control and measurements .....	131
6.2. Measurement procedure.....	135
6.3. Results and discussion .....	136
6.3.1. Final equilibrium state.....	136
6.3.2. Analysis of the unsteady pressure variation process .....	138
6.4. Summary.....	145
References .....	145
<b>Conclusions and perspectives.....</b>	<b>147</b>



---

# Nomenclature

## Symbols

$a$	Microtube radius (m)
$A$	Area normal vector
$A_p$	Amplitude of pressure fluctuation (Pa)
$A_p^*$	Fluctuating pressure gain
$b$	Intermolecular distance (m)
$\bar{c}$	Mean thermal velocity ( $\text{ms}^{-1}$ )
$c_r$	Relative velocity between two molecules ( $\text{ms}^{-1}$ )
$d$	Mean molecular diameter (m) (Chapter 2)
$d$	Ratchet height (m) (Chapter 5)
$D$	Tube diameter (m)
$D_h$	Hydraulic diameter (m)
$E$	Diode efficiency
$F_N$	Number of real molecules represented by a simulator in DSMC
$G_p$	Pressure gain
$G_\rho$	Density gain
$h$	Heat transfer coefficient ( $\text{W m}^{-2} \text{K}^{-1}$ ) (Chapter 6)
$h$	Distance between two ratchet surfaces (m) (Chapter 5)
$H$	Channel height (m)
$I_j$	Simulator indicator
$k$	Boltzmann constant ( $1.381 \times 10^{-23} \text{ J K}^{-1}$ )
$k_2$	Mean free path coefficient
$Kn$	Knudsen number

---

$L$	Channel length (m)
$L_c$	Characteristic length (m)
$L_m$	Misalignment distance in ratchet pumps (m)
$L_s$	Length of channel straight part in curved-channel Knudsen pump (m)
$L_s$	Length of channel centerline of the curved part in curved-channel Knudsen pump (m)
$L_t$	Total channel length in curved-channel Knudsen pump (m)
$L_{sv}$	Characteristic length of a sampling volume (m)
$L_z$	Length of heating/cooling zone (m)
$m$	Molecular mass (kg)
$M$	Molecular weight ( $\text{kg mol}^{-1}$ )
$\dot{m}$	Mass flowrate ( $\text{m s}^{-1}$ )
$n$	Number density ( $\text{m}^{-3}$ )
$n$	Coordinate in the direction normal to the wall (m)
$N$	Number of test molecules in a DSMC cell
$N_s$	Number of pump stages
$N_{NTC}$	Maximum number of collisions in a DSMC cell
$P$	Dimensionless logarithmic pressure gradient
$p_s$	Perimeter (m)
$P$	Pressure (Pa)
$Pr$	Prandtl number
$\bar{q}$	Average volume flowrate ( $\text{m}^3 \text{s}^{-1}$ )
$q$	Heat flux ( $\text{W m}^{-2}$ )
$Q_p$	Dimensionless pressure driven volume flowrate

---

$Q_T$	Dimensionless temperature driven volume flowrate
$r$	Curvature radius (m)
$R$	Specific gas constant ( $\text{J kg}^{-1}\text{K}^{-1}$ )
$R_c$	Radius of curvature in serpentine Knudsen pump (m)
$R_1$	Radius of inner cylinder (m)
$R_2$	Radius of outer cylinder (m)
$s$	Coordinate in the direction tangent to the wall (m)
$S$	Cross-sectional area ( $\text{m}^2$ )
$t$	Time (s)
$T$	Temperature (K)
$T_c$	Cold temperature (K) in a reservoir, on a surface or at a point
$T_h$	Hot temperature (K) in a reservoir, on a surface or at a point
$TPD$	Thermomolecular pressure difference (Pa)
$TPR$	Thermomolecular pressure ratio
$u_s$	Tangential velocity ( $\text{m s}^{-1}$ )
$u_n$	Normal velocity ( $\text{m s}^{-1}$ )
$V$	Volume of a reservoir ( $\text{m}^3$ )
$W$	Channel width (m)
$z$	Axial coordinate (m)

### **Greek Symbols**

$\alpha$	Collision coefficient for VSS model
$\alpha_v$	Tangential momentum accommodation coefficient
$\alpha_T$	Thermal accommodation coefficient
$\alpha_I$	Accommodation coefficient of inclined wall for ratchet surface

---

$\alpha_v$	Accommodation coefficient of vertical wall for ratchet surface
$\beta$	Ratchet angle ( $^\circ$ )
$\varepsilon$	Dimensionless ratio of temperature over pressure variations
$\gamma$	Specific heats ratio
$\mu$	Dynamic viscosity (Pa s)
$\zeta$	Index relating pressure and temperature ratios
$\sigma_p$	Viscous slip coefficient
$\sigma_T$	Thermal slip coefficient
$\sigma_t$	Total collision cross-section ( $\text{m}^2$ )
$\xi_T$	Temperature jump coefficient
$\lambda$	Mean free path (m)
$\lambda_e$	Equivalent mean free path (m)
$\lambda_g$	Thermal conductivity ( $\text{W m}^{-1} \text{K}^{-1}$ )
$\delta$	Mean molecular spacing (m)
$\rho$	Gas density ( $\text{kg m}^{-3}$ )
$\tau$	Time constant (s)
$\tau _{wall}$	Shear stress at the wall (Pa)
$\theta$	Dimensionless logarithmic temperature gradient (Chapter 1)
$\theta$	Angle between Cartesian and local coordinate systems (rad) (Chapter 2)
$\nu$	Mean collision rate ( $\text{s}^{-1}$ )
$\varphi$	Angle of tapered channel ( $^\circ$ )
$\dot{\Phi}$	Heat rate per unit volume ( $\text{W m}^{-3}$ )
$\Phi_s$	Heat rate (W)
$\omega$	Collision coefficient for VHS or VSS model
$\omega_1$	Angular velocity of a cylinder ( $\text{rad s}^{-1}$ )

---

$\chi$  Deflection angle (rad)

### **Acronyms**

BGK Bhatnagar–Gross–Krook

CFD Computational Fluid Dynamics

DSMC Direct Simulation Monte Carlo

HS Hard Sphere

LPBS Low Pressure Boundary Slip

NTC No Time Counter

TMAC Tangential Momentum Accommodation Coefficient

UDF User Defined Function

VHS Variable Hard Sphere

VSS Variable Soft Sphere



# Introduction

---

## *Gas Microflows*

Due to the trend of miniaturization of electromechanical systems, gas micropumps are required in a wide range of sensing and analysis related microsystems, such as electronic noses, mass spectrometers, gas chromatographs (Pham-Van-Diep et al. 1995). One of the attractive candidates of miniaturized vacuum pump is the Knudsen pump which operates according to the thermal transpiration effect (Vargo et al. 1999). After analyzing various microsystems involving confined gas flow, it is clear that the rarefaction effects which result from shrinking down the device size cannot, in almost every case, be neglected (Colin 2013). One of the most commonly used parameters chosen to characterize the rarefaction level is the Knudsen number  $Kn$  which is defined as the ratio of the mean free path  $\lambda$  of the gas molecules (i.e., the average distance travelled between two successive collisions) to the internal characteristic length  $L$  of the system. The Knudsen number allows a classification of the gas flow regimes. In general, four different types of gas flow regimes –continuum, slip, transitional, and free molecular– are considered. The appropriate methods must be chosen according to the encountered flow regime.

## *Thermal transpiration flows and Knudsen pumps*

In rarefied gases, flows can be generated by a tangential temperature gradient along a wall, without any initial pressure gradient. This well-known phenomenon is the so-called thermal creep, or thermal transpiration, effect. This phenomenon was first analyzed independently by Reynolds (Reynolds 1879) and Maxwell (Maxwell 1879) in 1879. The thermal transpiration is the basis of the Knudsen pump operation principle: it allows gas pumping without any moving part when the gas is under rarefied conditions, either due to small dimensions or to low pressures. Several different designs of Knudsen pumps have been studied in the past years, following the seminal work of Knudsen itself (Knudsen 1909). The typical Knudsen micropump is based on a cascade system in which a basic unit is composed of a microchannel (McNamara et al. 2005, Young et al. 2005, Gupta et al. 2012, An et al. 2014) or of a

microporous medium (Han et al. 2007, Gupta et al. 2011) connecting two mini chambers with different temperatures. Alternative configurations have been proposed and numerically studied, consisting of alternately connected curved and straight microchannels (Aoki et al. 2009) or curved microchannels with different curvature radii (Bond et al. 2016). In these designs, however, the main practical difficulty comes from the necessity to accurately control the temperature gradient generated along the walls.

### *Structure of the thesis manuscript*

The present thesis is devoted to the investigation of thermal transpiration flows using analytical and numerical approaches as well as experimental measurements, with a view to an application to the design of novel Knudsen pumps, more efficient and/or easier to manufacture and control.

In Chapter 1, the thermal transpiration phenomenon and the derived Knudsen pumps are introduced by reviewing the main works published in the literature on this subject. Recently reported prototypes of Knudsen pumps using nanoporous materials or etched microchannels are introduced. The main limitations of the already studied Knudsen pump configurations are summarized and current needs of efficient numerical tools and accurate experimental data are highlighted.

In Chapter 2, several basic concepts -including the dilute gas assumption and molecules collision models required for modeling rarefied gas microflows- are firstly introduced and the models developed in this work for slip and transition flows are presented. A numerical method using the CFD code ANSYS Fluent®, in which User Defined Functions (UDF) are implemented to simulate accurate boundary conditions are developed. Finally, the DSMC method is introduced and an open source code named `dsmcFoamStrath`, as well as a code allowing a novel decomposition of the solution into ballistic and collision parts, are presented.

Chapter 3 presents a numerical investigation of thermal transpiration flows in tapered microchannels. An isothermal pressure-driven flow through a tapered channel is first studied and the numerical results are compared with existing experimental data. Then the thermal transpiration flow in convergent and divergent channels is investigated and the observed diode effect is analyzed. With a principle based on this

diode effect, a novel Knudsen pump with tapered channels is proposed and numerically tested.

Chapter 4 presents a numerical design of a serpentine Knudsen pump, the principle of which is based on the transpiration effect in curved and straight channels in the slip flow and early transition regimes. This pump is constructed by alternatively connecting a series of curved and straight channels with the same uniform cross-section. A parameter analysis for a single-stage micropump and the performance of multi-stage micropumps are presented. A first prototype of a multi-stage curved-channel Knudsen pump at millimetric scale designed and fabricated at the Karlsruhe Institute of Technology is presented and its performances are evaluated through a series of numerical simulations.

In Chapter 5, the performance of a new type of Knudsen pump, which only requires isothermal hot or cold walls and is consequently much easier to control than a classic pump with temperature gradient along a surface, is investigated. The pumping element consists of two facing isothermal ratchet surfaces with different uniform temperatures. The asymmetric saw-tooth like surfaces leads to a rectified Knudsen flow along the walls. A numerical investigation with both CFD and DSMC simulations is presented.

Chapter 6 presents a new experimental set-up for investigating a thermal transpiration flow through a single micro-tube. The experimental apparatus has been designed to be adaptable for investigating various channel configurations as well as autonomous Knudsen compressors. The experimental set-up and the experimental procedure are detailed. Then the first experimental results are shown and discussed with comparison to theoretical data.

Finally, conclusions and perspectives of this work are proposed at the end of the manuscript.

## **References**

- An, S., Gupta, N. K. and Gianchandani, Y. B. (2014). "A Si-micromachined 162-stage two-part Knudsen pump for on-chip vacuum." *Journal of Microelectromechanical Systems* 23(2): 406-416.
- Aoki, K., Degond, P. and Mieussens, L. (2009). "Numerical simulations of rarefied gases in curved channels: thermal creep, circulating flow, and pumping effect." *Communications in Computational Physics* 6(5): 911-954.

- Bond, D. M., Wheatley, V. and Goldsworthy, M. (2016). "Numerical investigation into the performance of alternative Knudsen pump designs." *International Journal of Heat and Mass Transfer* 93: 1038-1058.
- Colin, S. (2013). *Single-phase gas flow in microchannels. Heat transfer and fluid flow in minichannels and microchannels*, Elsevier: 11-102.
- Gupta , N. K., An, S. and Gianchandani, Y. B. (2012). "A Si-micromachined 48-stage Knudsen pump for on-chip vacuum." *Journal of Micromechanics and Microengineering* 22(10): 105026.
- Gupta, N. K. and Gianchandani, Y. B. (2011). "Porous ceramics for multistage Knudsen micropumps—modeling approach and experimental evaluation." *Journal of Micromechanics and Microengineering* 21(9): 095029.
- Han, Y.-L. and Muntz, E. P. (2007). "Experimental investigation of micro-mesoscale Knudsen compressor performance at low pressures." *Journal of Vacuum Science & Technology B: Microelectronics and Nanometer Structures* 25(3): 703-714.
- Knudsen, M. (1909). "Eine Revision der Gleichgewichtsbedingung der Gase. Thermische Molekularströmung." *Annalen der Physik* 336(1): 205-229.
- Maxwell, J. C. (1879). "On stresses in rarefied gases arising from inequalities of temperature." *Phil. Trans. R. Soc.* 170: 231-256.
- McNamara, S. and Gianchandani, Y. B. (2005). "On-Chip Vacuum Generated by a Micromachined Knudsen Pump." *Microelectromechanical Systems, Journal of* 14(4): 741-746.
- Pham-Van-Diep, G., Keeley, P., Muntz, E. P., et al. (1995). "A micromechanical Knudsen compressor." *Rarefied gas dynamics* 1: 715-721.
- Reynolds, O. (1879). "On Certain Dimensional Properties of Matter in the Gaseous State. Part I. Experimental Researches on Thermal Transpiration of Gases through Porous Plates and on the Laws of Transpiration and Impulsion, Including an Experimental Proof That Gas is Not a Continuous Plenum. Part II. On an Extension of the Dynamical Theory of Gas, Which Includes the Stresses, Tangential and Normal, Caused by a Varying Condition of Gas, and Affords an Explanation of the Phenomena of Transpiration and Impulsion." *Philosophical Transactions of the Royal Society of London* 170: 727-845.
- Vargo, S., Muntz, E. and Tang, W. (1999). *The MEMS Knudsen Compressor as a Vacuum Pump for Space Exploration Applications. 2nd International Conference on Integrated Micro/Nanotechnology for Space Applications. Pasadena, California, USA.*
- Young, M., Han, Y. L., Muntz, E. P., et al. (2005). "Characterization and Optimization of a Radiantly Driven Multi - Stage Knudsen Compressor." *AIP Conference Proceedings* 762(1): 174-179.

# Chapter 1

## Thermal transpiration flows and Knudsen pumps

---

In this chapter, the thermal transpiration phenomenon and the derived Knudsen pumps are introduced by reviewing the main works published in the literature on this subject. The thermal transpiration phenomenon was first observed by Reynolds in the early 1900s and a series of works have followed this seminal observation, including experimental measurements as well as analytical and numerical investigations. Meanwhile, since 1909 when Knudsen reported the first gas pump based on the transpiration phenomenon, various researchers have contributed to the development of the so-called Knudsen pumps. Some of these pumps have been constructed using porous materials and micromachined Knudsen pumps were also recently reported and experimentally tested.

### 1.1. Thermal transpiration flow

In rarefied gases, i.e. in low pressure and/or highly confined configurations, flows can be generated by only a tangential temperature gradient applied along a wall, without any initial pressure gradient. This now well-known phenomenon is the so-called thermal creep, or thermal transpiration, effect. The phenomenon of thermal transpiration was first analyzed independently by Reynolds (Reynolds 1879) and Maxwell (Maxwell 1879) in 1879. Maxwell investigated stresses and motions of gas molecules induced by temperature gradients and proposed the reference Maxwell boundary condition which will be discussed in the second chapter in detail. Analyzing the momentum transfer between the gas molecules and the wall, Sone (Sone 2007) has proposed an explanation of the physical mechanism of the thermal transpiration phenomenon. The asymmetry in the momentum flux from the hot and the cold sides of a narrow channel is primarily responsible for the thermal transpiration flow. As shown in Fig. 1.1, let us consider a point **A** of a wall submitted to a tangential temperature gradient and the molecules impinging a small region of area  $dS$  around this point, and issued from various directions. The average velocity of the molecules coming from the hotter region is larger than the average velocity of the molecules

coming from the colder region, which induces a net momentum transferred to  $dS$ . This momentum has a component in the opposite direction of the temperature gradient. In reaction, the gas is subject to a net force in the direction of the temperature gradient and a flow is finally induced in this direction.

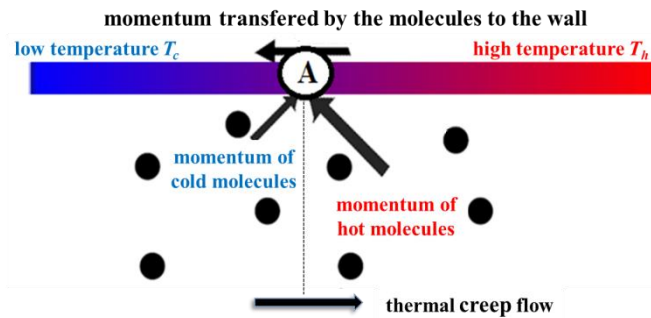


Figure 1.1 Physical mechanism of thermal transpiration, following (Aoki et al. 2009)

Reynolds (Reynolds 1879) experimentally investigated first the thermal transpiration flow with his instrument which essentially consisted of two chambers separated by a plate of porous material; the two chambers were kept at constant pressure but different temperatures. By both experimental and theoretical observations, Reynolds drew several important conclusions: 1) When gas exits at equal pressure on each side of a porous plate across which the temperature varies, the gas will transpire through the plate from the colder to the hotter side, with velocities depending on the absolute temperature and chemical nature of the gas, the relation between the density of the gas and the fineness of the pores, the thickness of the plate and the temperature difference between the two sides of the plate. 2) In order to prevent transpiration through the plate, the pressure on the hotter side must be greater than the pressure on the colder side. This pressure difference, at which the transpiration is zero, depends on parameters such as the temperature difference and the chemical nature of the gas but not on the thickness of the plate. The difference of pressure also depends on the rarefaction of gas and reaches a maximum between free molecular and hydrodynamic regimes.

Almost every experiment on thermal transpiration flows described in the literature was based on a similar configuration (see Fig. 1.2), in which the porous plate between the two chambers could be replaced with a microchannel or a microtube. In these

experiments, the two chambers were at the same initial pressure and at a different temperature. The final zero-flow state related to several characteristic values such as the final pressure difference between the two chambers was investigated in details and the unsteady flow from the initial state to the final zero-flow was also studied (see Section 1.1.2). Before that, some fundamental experiments designed to prove the existence of flows induced by temperature fields were published (see Section 1.1.1).

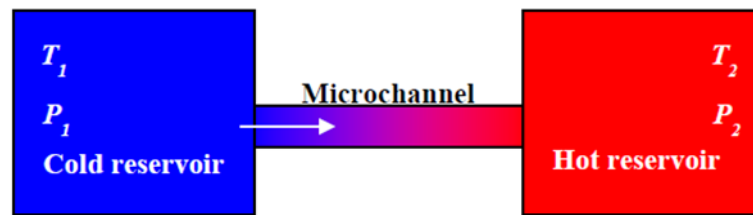


Figure 1.2 Configuration of classical thermal transpiration flow

### 1.1.1. Fundamental demonstration of flow induced by temperature fields

The rotation of the windmill in the famous Crookes radiometer is a consequence of a thermal transpiration flow (Kennard 1938). However, the Crookes radiometer does not provide a direct demonstration that a flow can be induced along a wall with a temperature gradient.

An experimental apparatus, as shown in Fig. 1.3, was devised by Sone to directly show the thermal transpiration flow (Sone 1991). A rectangular glass plate was positioned with its longer side in the vertical direction and an electric Nichrome heater was placed near the lower end of the plate. A windmill with cellophane vanes designed to detect any vertical flow was placed in front of the plate. The whole system was put in a cylindrical vacuum chamber made of a glass bell jar on a steel base, where the pressure could be controlled between atmospheric pressure and a few Pa. When the plate was heated, its temperature was about 34 °C near its upper end and 140 °C in the heated region. When the gas was at atmospheric conditions, the windmill rotated at 110 rpm, revealing a flow which was attributed to natural convection. As pressure decreased, the rotation of windmill became gradually slower and stopped at about 1.4 kPa. At lower pressure, it started rotating again at about 40 Pa but in the opposite direction, and its speed increased and reached about 60 rpm at 13 Pa and 140 rpm at 3 Pa. From the direction of rotation of the windmill, it was

deduced that the flow was in the direction of the temperature gradient. This experiment qualitatively showed a thermal transpiration flow in a rarefied gas and demonstrated a strong contrast with the natural convection observed in atmospheric conditions.

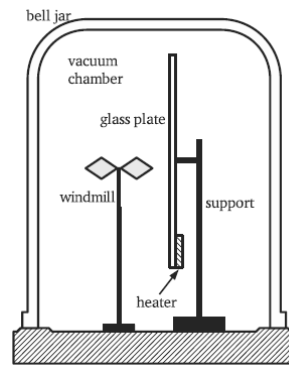


**Figure 1.3** Experimental apparatus for demonstration of thermal transpiration flow (Sone 1991)

This simple experiment is very helpful to prove the existence of flow generation with a new design and gives some rough qualitative results. Sone et al. used an experimental apparatus similar to the one shown in Fig. 1.4 to demonstrate one-way flow (Sone et al. 1996) and the so-called thermal edge flow (Sone et al. 1997). In the first apparatus (Fig. 1.4a), a duct consisting of two circular pipes of different diameters connected and heated at the level of their common section in the middle part of the duct, a flow from the thinner pipe to the wider one was detected by a windmill. This flow, induced through a pipe without average pressure and temperature gradients only by devising the shape of the pipe, is the so-called one-way flow. Similar experiments were done in a pipe equipped with one or several shelves (Sone 2007). In the second apparatus (Fig. 1.4b), a plate was set vertically in a vacuum chamber and the whole plate was heated at about 45 °C. In an operating pressure range of 5-20 Pa, a steady flow was observed with the rotation of the windmill: this flow was induced owing to the non-uniform temperature field expressed by sharply curved isothermal lines around the edges of the plate. The flow predicted by some previous numerical simulations was observed by this experiment. Through these simple experiments and related numerical simulations (Sone et al. 1996, Aoki et al. 1998), Knudsen pumps based on thermal edge flows (Sugimoto et al. 2005) and a



An equilibrium state between the two reservoirs is finally achieved when

$$\frac{P_2}{P_1} = \left( \frac{T_2}{T_1} \right)^\zeta, \quad (1.1)$$

where  $\zeta$  is an index which depends on the operating conditions.

In this whole process, several interesting quantities are involved:

- 1) the characteristic parameters at the steady equilibrium state, such as the thermomolecular pressure difference  $TPD = P_2 - P_1$ , the thermomolecular pressure ratio  $TPR = P_2/P_1$  and the index  $\zeta$ ;
- 2) the mass flowrate  $\dot{m}_T$  generated by the thermal transpiration effect;
- 3) the characteristic time of the unsteady pressure variation process.

#### Characteristic parameters at steady equilibrium state

The thermomolecular pressure difference  $TPD$ , the thermomolecular pressure ratio  $TPR$  and the index  $\zeta$  have been measured with some recent experiments (Porodnov et al. 1978, Han et al. 2007a, Han et al. 2007b, Rojas-Cardenas et al. 2011, Yamaguchi et al. 2014). The information on the tested channels, the imposed temperature differences and the range of investigated Knudsen numbers in these experiments are listed in Table 1.1. The Knudsen number  $Kn$ , defined as the ratio of the mean free path of the gas molecules over the hydraulic diameter of the microchannel, allows quantifying the degree of rarefaction of the flow. It increases either when the pressure or the channel hydraulic diameter is decreased. Its role on the thermal transpiration phenomenon is crucial and is discussed in details in Chapter 2. In the reported experiments, the microchannels were made of low thermal conductivity materials, such as silica or Polyether ether ketone (PEEK), which permit a better control of the temperature gradient along the channel with a minimum heat loss. They were tested under low pressure conditions corresponding to a Knudsen number ranging from 0.01 to 1, for microchannel sections with characteristic lengths of several hundred of micrometers. In order to measure  $TPD$ , either a differential capacitance micro-manometer (Porodnov et al. 1978, Han et al. 2007a) or two capacitance diaphragm gauges (Rojas-Cardenas et al. 2011, Yamaguchi et al. 2014) were used to monitor the pressures.

**Table 1.1 Quantitative experiments on thermal transpiration flows**

Reference	Channel characteristics - length $L$ and diameter $D$ or height $H$ and width $W$	Temperatures	$Kn$
(Porodnov et al.1978)	Single glass capillary $D = 1.292$ mm , $L/D = 125$	$T_2 = 293$ K , $T_1 = 273.2$ K	0.01 – 1
(Han et al.2007)	Aerogel membrane with capillaries $D = 0.21$ mm , or rectangular channels $H = 0.5$ mm	Unknown (the hot side is heated by an incident flux of $125$ mW cm <sup>-2</sup> )	0.01 – 10
(Rojas-Cardenas et al. 2013)	single glass capillary $D = 0.485$ mm , $L/D = 109$	$T_2 = [336; 353.5; 372]$ K  $T_1 = 300 \pm 1$ K	0.01 – 1
(Yamaguchi et al. 2014)	Single PEEK rectangular microchannel $H = 0.22$ mm , $W = 6$ mm , $L/H = 332$	$T_2 = 346$ K , $T_1 = 289$ K	0.01 – 10

The experimental set-ups described in (Han et al. 2007b, Rojas-Cardenas et al. 2011, Yamaguchi et al. 2014) were similar: two pressure gauges were connected to the cold and hot reservoirs for monitoring the pressure variation and the two reservoirs were connected in addition by a tube equipped with a valve, for two purposes: balancing pressure in reservoirs at the beginning of the test when the valve was open and launching the measurement process when it was turned to be closed. A toggle valve was used in (Han et al. 2007b) and an electrically controlled microvalve was used in (Rojas-Cardenas et al. 2011, Yamaguchi et al. 2014). Besides, a differential pressure gauge was used in (Han et al. 2007a) to measure the pressure difference.

The following main results were obtained by those experiments:

1)  $TPD$  first increases with  $Kn$  and reaches a maximum value for  $0.25 \leq Kn \leq 0.5$  and decreases with  $Kn$  for higher values. The value of  $TPD$  also depends on the molecular weight of the gas and on the applied temperature difference. Furthermore, the results obtained with a rectangular microchannel or a microtube are in good agreement for the characteristic lengths.

2) The experimental value of index  $\zeta$  increases from 0 to 0.3 when the Knudsen number increases from 0.01 to 1. It is dependent on the walls nature and roughness but does not depend on the temperature difference  $T_2 - T_1$  or on the gas species.

3)  $TPR$  decreases in a small range from 1 to 0.95 as the Knudsen number increases from 0.01 to 1. In addition,  $TPR$  decreases when the temperature difference increases but it does not depend on the gas species.

Pressure variation and characteristic time

The pressure variations in each reservoir closely follow an exponential fit

$$P = (P_f - P_i)(1 - \exp[-t/\tau]) + P_i \quad (1.2)$$

where  $\tau$  is the characteristic time of the process and  $P_i$  and  $P_f$  are the initial and final pressures, respectively. The value of  $\tau$  is given by an equation proposed by (Han et al. 2007b) or chosen according to the pressure variation rate with time (Rojas-Cárdenas 2012). From the published experimental data,  $\tau$  was in the order of a few tens of seconds, but of course the pressure variation is related to the Knudsen number, the gas species, the size of the reservoirs and the applied temperature difference.

Mass flowrate of thermal transpiration flow

Porodnov et al. (Porodnov et al. 1978) theoretically obtained from a kinetic approach the non-dimensional volume flowrate of a thermal transpiration flow through a capillary and separated the contribution of the temperature driven flow (thermal transpiration),

$$Q_T = \frac{\sqrt{\frac{2m}{kT}}}{\theta S} \bar{q}_T, \quad (1.3)$$

from the contribution of the pressure driven flow (Poiseuille flow):

$$Q_p = -\frac{\sqrt{\frac{2m}{kT}}}{pS} \bar{q}_p. \quad (1.4)$$

In Eqs. (1.3) and (1.4),  $k = 1.381 \times 10^{-23} \text{ J K}^{-1}$  is the Boltzmann constant,  $m$  is the molecular mass,  $S$  is the cross-sectional area of the capillary,  $\bar{q}_T$  (respectively  $\bar{q}_P$ ) are the average volume flowrates due to the temperature (respectively pressure) gradients along the capillary, and

$$\theta = \frac{D}{2T} \frac{dT}{dz} ; \quad p = \frac{D}{2P} \frac{dP}{dz} \quad (1.5)$$

are respectively the logarithmic temperature and pressure gradients in direction  $z$ , along the capillary of radius  $D/2$ . In the final steady state, the total average flowrate is zero, i.e.  $\bar{q}_T + \bar{q}_P = 0$ . Thus, it is easy to deduce:

$$\frac{dP}{P} = \left( \frac{Q_T}{Q_P} \right) \frac{dT}{T}. \quad (1.6)$$

By integrating Eq. (1.6) along the capillary between the two reservoirs, we obtain:

$$\frac{P_2}{P_1} = \exp \left[ \int_{T_1}^{T_2} \left( \frac{Q_T}{Q_P} \right) \frac{dT}{T} \right]. \quad (1.7)$$

When  $T_2 \approx T_1$ , the integration of Eq. (1.7) gives as a first approximation

$$\frac{P_2}{P_1} = \left( \frac{T_2}{T_1} \right)^{\frac{Q_T}{Q_P}}, \quad (1.8)$$

which is similar to Eq. (1.1), with

$$\zeta = \frac{Q_T}{Q_P}. \quad (1.9)$$

Therefore, in experiments with small temperature difference, the parameter  $\zeta$  can be approximated by  $\zeta = \ln(P_2/P_1) / \ln(T_2/T_1)$  and the dimensionless volume flowrate  $Q_p$  due to the pressure gradient is calculated by classic models, as detailed in Chapter 2. Using Eq. (1.9), the dimensionless thermal transpiration flow rate is then obtained.

The mass flowrate of a steady thermal transpiration flow was also measured directly using the constant volume method (Rojas-Cardenas et al. 2011). As previously described, the complete flow evolution from the initial equilibrium state to

the final equilibrium state may be characterized by two stages. At the beginning, the pressure in the hot reservoir increases quasi linearly and the pressure variation rate  $dP/dt$  is constant and the mass flowrate can be calculated by deriving the equation of state  $PV = mRT$  of an ideal gas:

$$\dot{m} = \frac{V}{RT} \frac{dP}{dt} \left( 1 - \frac{dT/T}{dP/P} \right), \quad (1.10)$$

where  $V$ ,  $R$  and  $m$  are the volume of the reservoir, the specific gas constant and the mass of the gas in the reservoir, respectively. In order to be able to use the so-called constant volume measurement technique and to calculate the stationary mass flow rate in an isothermal constant volume reservoir, the parameter  $\varepsilon = (dT/T)/(dP/P)$  should be small compared with unity, which was the case in the experiments from Rojas Cardenas et al., where  $\varepsilon$  was always lower than  $10^{-3}$ . The uncertainty on the mass flowrate was of the order of 4 %. The thermal transpiration mass flow rates measured in the range of rarefaction investigated were of the order of  $10^{-12}$  to  $10^{-11}$  kg s<sup>-1</sup>, for argon, helium and nitrogen.

### 1.1.3. Analytical and numerical investigations

The main analytical and numerical investigations about thermal transpiration flow are related to a configuration similar to that shown in Fig. 1.2. A complete analytical solution based on the Navier-Stokes equations has been derived in (Méolans et al. 2008) for the thermal transpiration flow in rectangular microchannels with large aspect ratio for Knudsen numbers smaller than 0.25. The mass flowrates of a rarefied gas through a long rectangular channel (Sharipov 1999) or a long tube (Sharipov 1997) driven by both pressure and temperature differences were calculated by Sharipov, applying the S-model kinetic equation. The model could be applied to the whole range of Knudsen number, with any pressure ratio or/and temperature ratio applied at the channel ends. The model was also extended to the cases of a long tube of variable radius (Sharipov et al. 2005), of a long rectangular channel with variable cross section (Graur et al. 2014) and of a long pipe with elliptic cross section (Graur et al. 2008). The results from (Graur et al. 2008) have been compared with a series of experimental results for thermal transpiration flow in a long glass tube (Rojas-Cárdenas et al. 2013) and a good agreement has been found. This type of flow has

also been studied by Direct Simulation Monte Carlo (DSMC) (Masters et al. 2007, Akhlaghi et al. 2014) and the kinetic equation with the Bhatnagar–Gross–Krook (BGK) model (Huang et al. 2012, Bond et al. 2016).

## **1.2. Knudsen pumps**

The Knudsen pump, the principle of which is based on the phenomenon of thermal transpiration, is a motionless pump which does not have any moving part and is free of working fluids or lubricants. The first functional Knudsen pump was reported by Knudsen himself in 1909 (Knudsen 1909). He achieved a compression ratio of ten across a set of ten capillaries (with an inner diameter of 374  $\mu\text{m}$ ) connected in series, each of which containing a small constriction and a hot point maintained at a higher temperature than the ambient temperature. Due to the technological constraints one century ago, Knudsen's device was limited to operations far below the atmospheric pressure. Since 1909, various researchers have contributed towards the development and improvement of the Knudsen pump.

### **1.2.1. Knudsen pumps with nanoporous materials**

Pham-Van-Diep et al. (Pham-Van-Diep et al. 1995) described a thermal transpiration compressor that combines a modern version of Reynolds' single porous stage with Knudsen's multistage compressor. Vargo et al. (Vargo et al. 1999) proposed the use of porous membranes instead of using individual capillaries, because nanoporous materials with a low thermal conductivity allow the construction of Knudsen compressors that can operate under high Knudsen number conditions over a much wider and more useful pressure range (from  $10^{-1}$  to  $10^5$  Pa). Later, the same group discussed the feasibility of using nanoporous aerogels (an aerogel is a supercritically dried silica gel with pore sizes of the order of 20 nm) for Knudsen pumping at atmospheric pressure (Vargo et al. 2001). This kind of compressor could generate a maximal pressure drop of about 15 kPa with helium for an input power of 1.7 W. A 15-stage Knudsen pump using an aerogel transpiration membrane was reported in (Young et al. 2005); it can achieve a pressure drop of about 16 kPa at atmospheric pressure with an input radiant power of 20.9  $\text{mW}/\text{cm}^2$ . Mechanically machined aerogel membranes with either capillaries or rectangular channels were

used to design a Knudsen pump which was experimentally studied by Han et al. (Han et al. 2007a, Han et al. 2007b).

A zeolite-based Knudsen pump using clinoptilolite, which is a natural zeolite comprising a nanoporous arrangement of silica and alumina tetrahedral, was built by Gupta et al. (Gupta et al. 2008) who demonstrated the feasibility of Knudsen pumps using bulk nanoporous ceramics. Then a 9-stage Knudsen pump (Gupta et al. 2011) with a clay-based 15PC<sup>1</sup> ceramic was constructed and it was demonstrated that the pump could generate a maximum pressure head of 12 kPa while operating at 55 K above room temperature. Higher gas flow generation capabilities have been demonstrated using thermal transpiration through nanoporous cellulose ester polymer membranes (Gupta et al. 2010), which have a large porosity (~ 70 %) and a low thermal conductivity (~ 0.2 W m<sup>-1</sup>K<sup>-1</sup>). A single stage Knudsen pump with a 11.5 mm diameter and 105 μm thick polymer membrane could work with an input power of 1.4 W, had a temperature variation of 30 K across the membrane and provided 0.4 sccm flow against a 330 Pa pressure head.

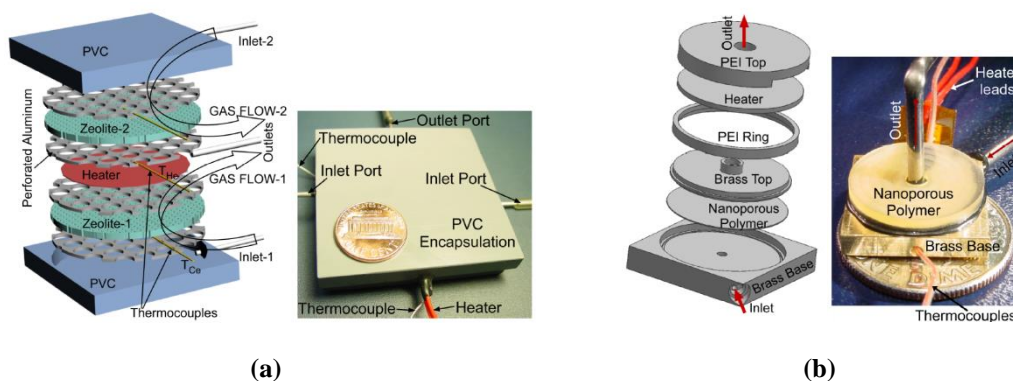


**Figure 1.5 Exploded views and photos of Knudsen pumps based on:**  
**(a) nanoporous ceramics (Gupta et al. 2008); (b) nanoporous cellulose ester polymer (Gupta et al. 2011).**

Recently, Knudsen pumps using thermoelectric materials were designed and experimentally studied (Kunal et al. 2010). The thermoelectric material maintains a high temperature difference which favors thermal transpiration and it also provides a possibility of bidirectional operation of the pumps. Since the hot and cold sides of the thermoelectric material are reversible, the direction of the pump may be changed by

<sup>1</sup> A 15 bar microporous ceramic (denoted 15PC) is a clay-based porous ceramic with air entry value of 15 bar. The air entry value is the pressure at which air will break through a wetted pore channel.

reversing the electrical current direction. Figure 1.6 presents the schematic of two designs where thermoelectric modules are thermally coupled to a nanoporous material (Mixed Cellulose Ester) with the use of a top and a bottom plate. The radial design (Fig. 6b) generated a larger pressure difference than the lateral design (Fig. 6a) because of a higher achieved temperature difference and a more uniform temperature distribution.

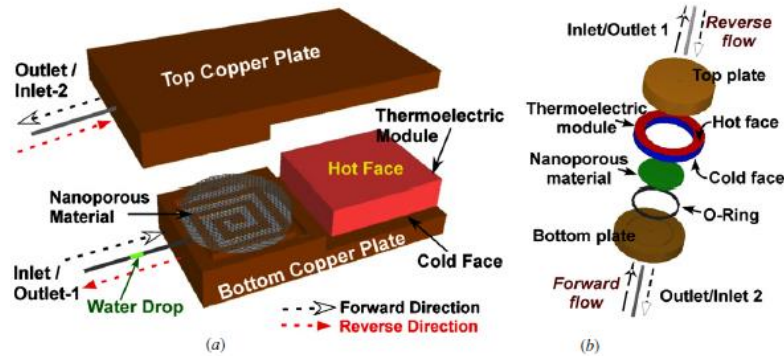


**Figure 1.6** Schematic of two designs of Knudsen pumps with thermoelectric modules (Kunal et al. 2010): (a) lateral design; (b) radial design.

### 1.2.2. Knudsen pumps with micromachined channels

Mc-Namara and Gianchandani (McNamara et al. 2005) reported a single-chip micromachined Knudsen pump which can operate at atmospheric pressure. A six-mask microfabrication process was used to fabricate the pump using a glass substrate and a silicon wafer. The Knudsen pump and two integrated pressure sensors only occupy an area of  $1.5 \times 2 \text{ mm}^2$ . The measurements showed that this Knudsen pump could achieve a pressure drop of about 54.7 kPa with a 80 mW input power.

Gupta et al. (Gupta et al. 2012) reported a 48-stage micromachined Knudsen pump with integrated Pirani gauges, using a five-mask, single-wafer structure. Using a serially cascaded multistage design (see Fig. 1.7a and b), a pressure drop of about 95 kPa was achieved with air at atmospheric pressure for an input power of 1.35 W. Later, the same group reported a 162-stage Knudsen pump (An et al. 2014) with a two-part architecture in which the first part included 54 stages designed for decreasing pressure from 101 kPa to 7 kPa and the second part included 108 stages designed for reaching lower pressures. The heights of the narrow channels of the two parts were  $0.1 \mu\text{m}$  and  $1 \mu\text{m}$  (see Fig. 1.7c), respectively. This approach provided greater

compression ratio and speed than an approach using a uniform design for each stage. The experimental results showed that the pump was able to decrease the pressure in a chamber from 101 kPa to 120 Pa, using an input power of 0.39 W.

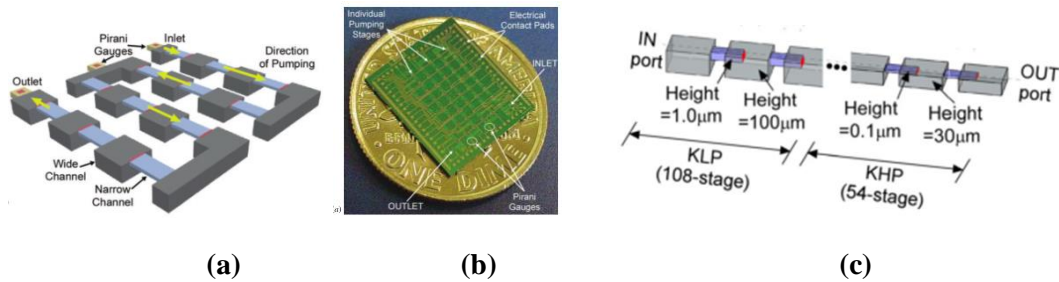


**Figure 1.7** Schematic (a) and photo (b) of a 48-stage Knudsen pump (Gupta et al. 2012) and schematic of 162-stage Knudsen pump (c) (An et al. 2014)

### 1.2.3. Knudsen pumps in laboratory conditions and experimental set-ups

In a purpose of fundamental research about thermal transpiration and Knudsen pumping, several Knudsen pumps were constructed as laboratory demonstrators and specific experimental set-ups were built to examine their performance.

Sone et al. (Sone et al. 2003) constructed and tested a Knudsen pump of ten stages based on their previous study about the so-called one way flow (Sone et al. 1996, Sone et al. 2000, Sone et al. 2001). Figure 1.8 shows photos of the pump. For each stage –or unit– of the pump, a bundle of 18 glass pipes of inner diameter 1.6 mm and length 15 mm is inserted in a half part of a circular glass pipe of inner diameter 15 mm and length 30 mm (Fig. 1.8a). A heater of Nichrome wire is wound around one end of each thin pipe and it is situated in the central part of the pipe of length 30 mm. In addition, a copper plate with a thickness of 1 mm is attached at both ends of each unit. It plays two roles: it is the joint to the next unit and the support, which is fixed to the base of a thick copper plate; the support serves to keep the temperature of the ends of the pipe unit at a constant temperature close to the room temperature. The set-up developed by Sone et al. is shown in Fig. 1.8b and Fig. 1.8c. The pumping system is put in a glass bell jar put on a steel base and one side of the pumping system is open in the bell jar and the other end of the pump is connected to a steel tank with a glass pipe. The pressure in the bell jar is controlled by the rotary vacuum pump and is set to a desired value at the beginning of the experiment. After confirming that the stationary state at a desired pressure is established, the heater is put on and the

pressures in the bell jar and in the tank, as well as the temperature of the heater are monitored. In this process, the pressure in the bell jar is kept constant at the initial pressure by adjusting the valve. The final pressure difference is measured and the pumping speed is estimated.

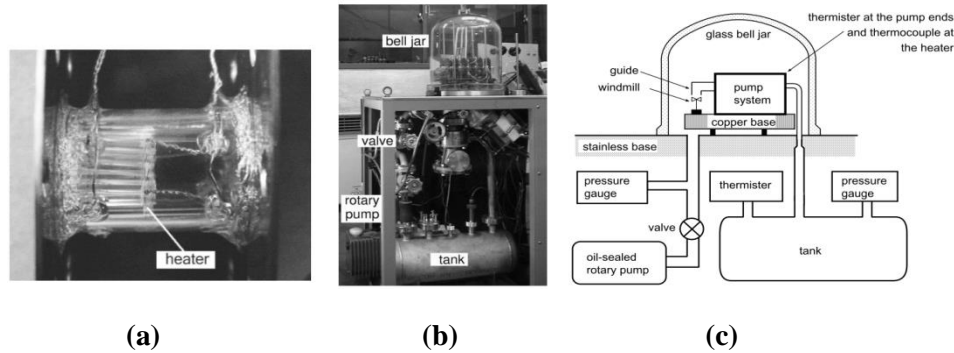


**Figure 1.8 Experimental system for Knudsen pumping:**  
**(a) Real system, zoom on the pump; (b) Real system, global view; (c) explanatory diagram (Sone et al. 2003).**

Sugimoto et al. constructed a pump driven by the edge flow phenomenon using an array of heated plates and an array of unheated plates (Sugimoto et al. 2005), as shown in Fig. 1.9. Owing to sharply curved isothermal lines in a zigzag way near the edges of the plates, a one-way flow is induced from the unheated plates to the heated plates (Fig. 1.10a). Figure 1.10b shows the structure of the pump. Five units are joined in a series. The ducts fitted out in the unit are used for flow cooling water in order to keep the pipe at a uniform and constant temperature. Electric current is supplied with a wire to the heater. The two thermocouples measure the temperature  $T_h$  of a heated plate and the temperature  $T_c$  of an unheated plate. In this system, no temperature gradient on the solid parts is required and heat flux through solid parts, which results in loss of energy, can be considerably reduced. Thus, the energy efficiency of the system is greatly improved.

The performance of this Knudsen pump driven by a thermal edge flow was experimentally examined with the set-up shown in Fig. 1.10 (Sugimoto et al. 2005). A pressure gauge and a thermistor are set at each of both ends (A and B) of the pump system. The entrance B is connected to a mass flow controller  $M_1$ , through which  $N_2$  gas flows into the pump system from a gas reservoir. The mass flow controller is a

combination of a valve and a flowmeter with a programmable system. It controls the flowrate in a passive way. The exit A of the pump system is connected to backing pumps and a bypass is connected to the gas reservoir and the backing pumps are equipped with a mass flow controller  $M_0$ . Through the backing pumps and the mass flow controller  $M_0$ , the pressure  $P_0$  is kept at a desired constant value. For a given pressure  $P_0$  at point A and a given energy supply rate of the pump system, the experiment provided the relations between the volume flowrate and the pressure  $P_1$  at point B. The final pressure difference  $P_1/P_0$  was corresponding to a zero flowrate. In these experiments, the performance of the Knudsen pump was tested for different operating pressures  $P_0$  and different energy supply rates. A final pressure ratio  $P_1/P_0$  in the range of [0.8-0.99] was measured.

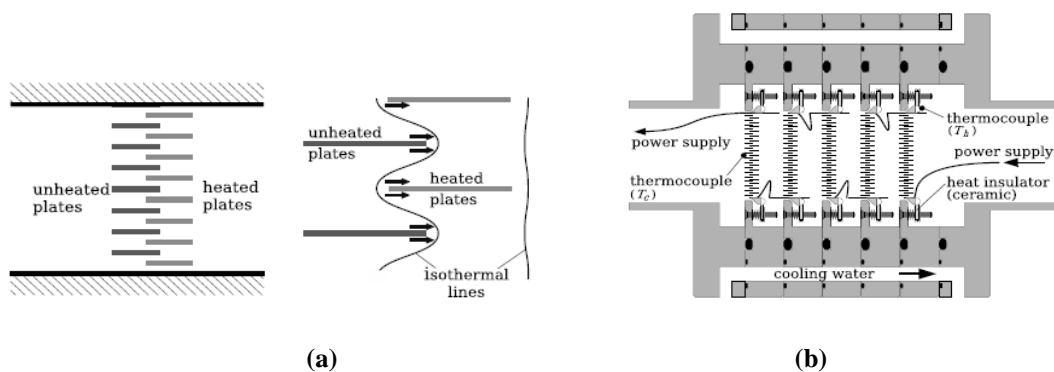


Figure 1.9 Knudsen pump based on the edge flow phenomenon:  
 a) one stage of the pump; b) complete pump system (Sugimoto et al. 2005).

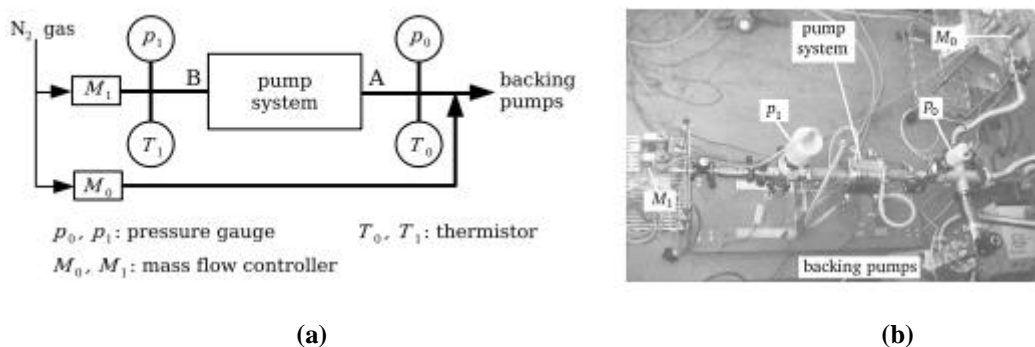


Figure 1.10 Experiment set-up:  
 (a) explanatory diagram; (b) real system (Sugimoto et al. 2005).

In summary, in order to enhance its efficiency, a Knudsen pump is usually designed as a cascaded system with a large number of stages combining heating and cooling systems to provide a periodic temperature distribution. The main practical difficulty comes from the necessity to keep a large contrast of dimensions between narrow channels and mini chambers and accurately control the temperature gradient generated along the walls. The characteristic width of the narrow channels should be comparable or larger than the mean free path of the molecules in order to optimize the transpiration flows generated by the temperature gradient. However, the characteristic dimensions of the mini-chambers have to be kept much larger than the mean free path in order to avoid an opposed transpiration flow generated by the inverse temperature gradient. In the Knudsen pump of 48 stages reported by Gupta (Gupta et al. 2012), a compromise between contrasted hydraulic diameters and easy integration has been found: the narrow channels are 100  $\mu\text{m}$  wide and 250  $\mu\text{m}$  long and the wide channels are about 300  $\mu\text{m}$  wide and 750  $\mu\text{m}$  long. The heater is placed in an intermediate cavity of width 280  $\mu\text{m}$  and length 250  $\mu\text{m}$ .

In order to avoid a complex design involving different hydraulic diameters, an alternative design made of a mono channel pump was proposed and numerically studied by Aoki et al. (Aoki et al. 2009): the channel is composed of a curved segment connected to straight segments with the same depth and width. In this layout, the transpiration effect is stronger in the curved segments than in the straight ones and a global net flow is finally observed. The performances of this pump will be discussed in Chapter 4.

With the goal to avoid a tricky control of the temperature distribution along the channels walls, a new Knudsen pump which consists of two facing isothermal ratchet surfaces at different temperatures will be studied in Chapter 5.

## **References**

- Akhlaghi, H. and Roohi, E. (2014). "Mass flow rate prediction of pressure–temperature-driven gas flows through micro/nanoscale channels." *Continuum Mechanics and Thermodynamics* 26(1): 67-78.
- An, S., Gupta, N. K. and Gianchandani, Y. B. (2014). "A Si-micromachined 162-stage two-part Knudsen pump for on-chip vacuum." *Journal of Microelectromechanical Systems* 23(2): 406-416.

- Aoki, K., Degond, P. and Mieussens, L. (2009). "Numerical simulations of rarefied gases in curved channels: thermal creep, circulating flow, and pumping effect." *Communications in Computational Physics* 6(5): 911-954.
- Aoki, K., Sone, Y. and Waniguchi, Y. (1998). "A rarefied gas flow induced by a temperature field: Numerical analysis of the flow between two coaxial elliptic cylinders with different uniform temperatures." *Computers & Mathematics with Applications* 35(1-2): 15-28.
- Bond, D. M., Wheatley, V. and Goldsworthy, M. (2016). "Numerical investigation into the performance of alternative Knudsen pump designs." *International Journal of Heat and Mass Transfer* 93: 1038-1058.
- Graur, I. and Ho, M. T. (2014). "Rarefied gas flow through a long rectangular channel of variable cross section." *Vacuum* 101(0): 328-332.
- Graur, I. and Sharipov, F. (2008). "Non-isothermal flow of rarefied gas through a long pipe with elliptic cross section." *Microfluidics and Nanofluidics* 6(2): 267-275.
- Gupta, N. K., An, S. and Gianchandani, Y. B. (2012). "A Si-micromachined 48-stage Knudsen pump for on-chip vacuum." *Journal of Micromechanics and Microengineering* 22(10): 105026.
- Gupta, N. K. and Gianchandani, Y. B. (2008). "Thermal transpiration in zeolites: A mechanism for motionless gas pumps." *Applied Physics Letters* 93(19): 193511.
- Gupta, N. K. and Gianchandani, Y. B. (2010). A high-flow Knudsen pump using a polymer membrane: Performance at and below atmospheric pressures. *Micro Electro Mechanical Systems (MEMS), 2010 IEEE 23rd International Conference on, IEEE*.
- Gupta, N. K. and Gianchandani, Y. B. (2011). "Porous ceramics for multistage Knudsen micropumps—modeling approach and experimental evaluation." *Journal of Micromechanics and Microengineering* 21(9): 095029.
- Han, Y.-L. and Muntz, E. P. (2007a). "Experimental investigation of micro-mesoscale Knudsen compressor performance at low pressures." *Journal of Vacuum Science & Technology B: Microelectronics and Nanometer Structures* 25(3): 703-714.
- Han, Y.-L., Phillip Muntz, E., Alexeenko, A., et al. (2007b). "Experimental and Computational Studies of Temperature Gradient-Driven Molecular Transport in Gas Flows through Nano/Microscale Channels." *Nanoscale and Microscale Thermophysical Engineering* 11(1-2): 151-175.
- Huang, J.-C., Xu, K. and Yu, P. (2012). "A Unified Gas-Kinetic Scheme for Continuum and Rarefied Flows II: Multi-Dimensional Cases." *Communications in Computational Physics* 12(03): 662-690.
- Kennard, E. (1938). "Kinetic Theory of Gases." McGraw Hill: 327-332.
- Knudsen, M. (1909). "Eine Revision der Gleichgewichtsbedingung der Gase. Thermische Molekularströmung." *Annalen der Physik* 336(1): 205-229.
- Kunal, P. and Shamus, M. (2010). "Knudsen pump driven by a thermoelectric material." *Journal of Micromechanics and Microengineering* 20(12): 125032.
- Masters, N. D. and Ye, W. (2007). "Octant flux splitting information preservation DSMC method for thermally driven flows." *Journal of Computational Physics* 226(2): 2044-2062.

- Maxwell, J. C. (1879 ). "On stresses in rarefied gases arising from inequalities of temperature." *Phil. Trans. R. Soc.* 170: 231-256.
- McNamara, S. and Gianchandani, Y. B. (2005). "On-Chip Vacuum Generated by a Micromachined Knudsen Pump." *Microelectromechanical Systems, Journal of* 14(4): 741-746.
- Méolans, J. G. and Graur, I. A. (2008). "Continuum analytical modelling of thermal creep." *European Journal of Mechanics - B/Fluids* 27(6): 785-809.
- Pham-Van-Diep, G., Keeley, P., Muntz, E. P., et al. (1995). "A micromechanical Knudsen compressor." *Rarefied gas dynamics 1*: 715-721.
- Porodnov, B. T., Kulev, A. N. and Tuchvetov, F. T. (1978). "Thermal transpiration in a circular capillary with a small temperature difference." *Journal of Fluid Mechanics* 88(04): 609-622.
- Reynolds, O. (1879). "On Certain Dimensional Properties of Matter in the Gaseous State. Part I. Experimental Researches on Thermal Transpiration of Gases through Porous Plates and on the Laws of Transpiration and Impulsion, Including an Experimental Proof That Gas is Not a Continuous Plenum. Part II. On an Extension of the Dynamical Theory of Gas, Which Includes the Stresses, Tangential and Normal, Caused by a Varying Condition of Gas, and Affords an Explanation of the Phenomena of Transpiration and Impulsion." *Philosophical Transactions of the Royal Society of London* 170: 727-845.
- Rojas-Cárdenas, M. (2012). *Temperature Gradient Induced Rarefied Gas Flow*, Ecole Polytechnique Universitaire de Marseille.
- Rojas-Cardenas, M., Graur, I., Perrier, P., et al. (2011). "Thermal transpiration flow: A circular cross-section microtube submitted to a temperature gradient." *Physics of Fluids (1994-present)* 23(3): -.
- Rojas-Cárdenas, M., Graur, I., Perrier, P., et al. (2013). "Time-dependent experimental analysis of a thermal transpiration rarefied gas flow." *Physics of Fluids (1994-present)* 25(7): 072001.
- Sharipov, F. (1997). "Rarefied gas flow through a long tube at arbitrary pressure and temperature drop." *Journal of Vacuum Science and Technology A* 15(4): 2434-2436.
- Sharipov, F. (1999). "Non-isothermal gas flow through rectangular microchannels." *Journal of Micromechanics and Microengineering* 9: 394-401.
- Sharipov, F. and Bertoldo, G. (2005). "Rarefied gas flow through a long tube of variable radius." *Journal of Vacuum Science & Technology A* 23(3): 531-533.
- Sone, Y. (1991). "A simple demonstration of a rarefied gas flow induced over a plane wall with a temperature gradient." *Physics of Fluids A: Fluid Dynamics (1989-1993)* 3(5): 997-998.
- Sone, Y. (2007). *Molecular Gas Dynamics, Theory, Techniques, and Applications*. Boston, USA, Birkhauser Boston.
- Sone, Y., Fukuda, T., Hokazono, T., et al. (2001). Experiment on a one-way flow of a rarefied gas through a straight circular pipe without average temperature and pressure gradients. *Rarefied gas dynamics*. New York. AIP Conference Proceedings 585: 948-955.

- Sone, Y. and Sato, K. (2000). "Demonstration of a one-way flow of a rarefied gas induced through a pipe without average pressure and temperature gradients." *Physics of Fluids* (1994-present) 12(7): 1864-1868.
- Sone, Y. and Sugimoto, H. (2003). Vacuum pump without a moving part and its performance. AIP Conference Proceedings, IOP Institute of Physics Publishing LTD
- Sone, Y., Waniguchi, Y. and Aoki, K. (1996). "One-way flow of a rarefied gas induced in a channel with a periodic temperature distribution." *Physics of Fluids* (1994-present) 8(8): 2227-2235.
- Sone, Y. and Yoshimoto, M. (1997). "Demonstration of a rarefied gas flow induced near the edge of a uniformly heated plate." *Physics of Fluids* (1994-present) 9(11): 3530-3534.
- Sugimoto, H. and Sone, Y. (2005). Vacuum pump without a moving part driven by thermal edge flow. *Rarefied Gas Dynamics: 24th International Symposium on Rarefied Gas Dynamics*, AIP Publishing.
- Vargo, S., Muntz, E. and Tang, W. (1999). The MEMS Knudsen Compressor as a Vacuum Pump for Space Exploration Applications. 2nd International Conference on Integrated Micro/Nanotechnology for Space Applications. Pasadena, California, USA.
- Vargo, S. E. and Muntz, E. P. (2001). "Initial results from the first MEMS fabricated thermal transpiration-driven vacuum pump." AIP Conference Proceedings 585(1): 502-509.
- Yamaguchi, H., Rojas-Cárdenas, M., Perrier, P., et al. (2014). "Thermal transpiration flow through a single rectangular channel." *Journal of Fluid Mechanics* 744: 169-182.
- Young, M., Han, Y. L., Muntz, E. P., et al. (2005). "Characterization and Optimization of a Radiantly Driven Multi-Stage Knudsen Compressor." AIP Conference Proceedings 762(1): 174-179.

## Chapter 2

# Modeling of thermal transpiration flow

---

The development of simulation tools is crucial for investigating thermal transpiration flows and optimizing Knudsen pumps' design. In this chapter, several basic concepts -including the dilute gas assumption and molecules collision models- required for modeling rarefied gas microflows are firstly introduced and the models developed in this work for slip and transition flows are presented. Section 2.2 presents an analytical model for a simple transpiration flow between two plates in the slip flow regime and a numerical method using the CFD code ANSYS Fluent®, in which User Defined Functions (UDF) are implemented to simulate accurate boundary conditions. The developed numerical model can be used in any 2D geometry and provides an efficient tool for the design of Knudsen pumps. The DSMC method is introduced in section 2.3 and an open source code named *dsmcFoamStrath*, as well as a code allowing a novel decomposition of the solution into ballistic and collision parts, are presented. The DSMC models can be used in the whole rarefaction range, but are more efficient in the transition regime and the new decomposition method provides more information than a typical DSMC study for analyzing the transpiration flow.

### 2.1. General points about gas microflows modeling

#### 2.1.1 The simple dilute gas

The study presented in this thesis is restricted to a simple gas defined as a gas with a single chemical species, i.e. a gas in which all molecules are identical. Several characteristic length scales must be taken into account for modeling gas microflows, such as the mean molecular diameter  $d$ , the mean molecular spacing  $\delta$  and the mean free path  $\lambda$ . The mean molecular spacing  $\delta$  is directly related to the number density  $n$  with  $n = \delta^{-3}$ . The molecular mean free path is defined as the average distance traveled by a molecule between two successive collisions in a reference frame that follows the macroscopic movement. It is an important fundamental concept of the kinetic theory of gases which is based on the dilute gas approximation.

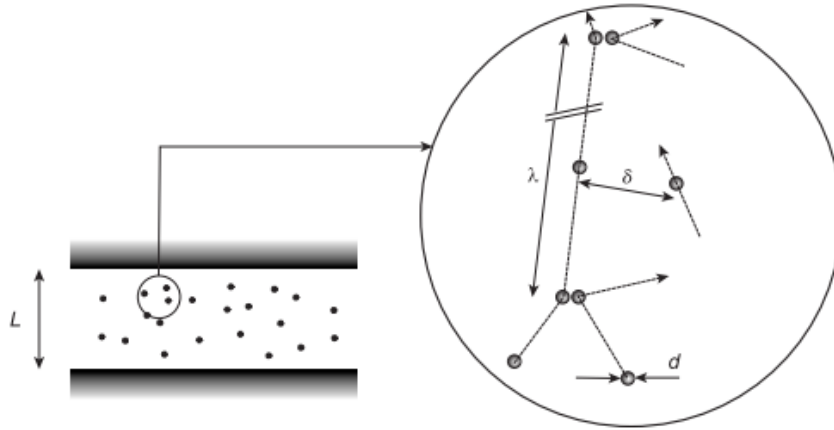


**Figure 2.1:** Main characteristic length scales taken into account at the molecular level (Colin 2013)

A gas is dilute when the molecular diameter  $d$  is much smaller than the mean molecular spacing  $\delta$ , i.e. when

$$\frac{d}{\delta} \ll 1. \quad (2.0)$$

In that case, most of the intermolecular interactions are binary collisions. With this approximation, the mean free path can be expressed as the ratio of the mean thermal velocity  $\bar{c}'$  to the mean collision rate  $\nu$ :

$$\lambda = \frac{\bar{c}'}{\nu} = \frac{1}{\nu} \sqrt{\frac{8kT}{\pi m}}, \quad (2.0)$$

where  $k = 1.381 \times 10^{-23} \text{ J K}^{-1}$  is the Boltzmann constant,  $m$  is the molecular mass and  $T$  the temperature.

### 2.1.2 Molecular collision models

As previously mentioned, the intermolecular collisions in dilute gases are overwhelmingly binary collisions. For a binary elastic collision, there is no transfer between the translation kinetic energy and the vibrational and rotational energies of the molecules. In this case, specifying the pre-collision velocities  $\mathbf{c}_1$  and  $\mathbf{c}_2$  of the two colliding molecules and using the momentum balance and energy conservation equations (four scalar equations) is not sufficient to determine the post-collision velocities  $\mathbf{c}_1^*$  and  $\mathbf{c}_2^*$  (six scalar unknowns). Therefore, the adoption of a molecular

collision model is needed to complete the modeling of molecular behavior. Several molecular collision models have been developed in the past decades.

HS Model

The simplest collision model is the hard sphere (HS) model in which the force between two molecules becomes effective when the distance between them is less than  $d_{12} = \frac{1}{2}(d_1 + d_2)$ , where  $d_1$  and  $d_2$  are the molecular diameters of the two molecules which are assumed to be constant. Figure 2.2 presents the geometric representation of the collision between two hard sphere molecules 1 and 2, where  $\mathbf{c}_r = \mathbf{c}_1 - \mathbf{c}_2$  and  $\mathbf{c}_r^* = \mathbf{c}_1^* - \mathbf{c}_2^*$  are the relative pre- and post-collision velocities.

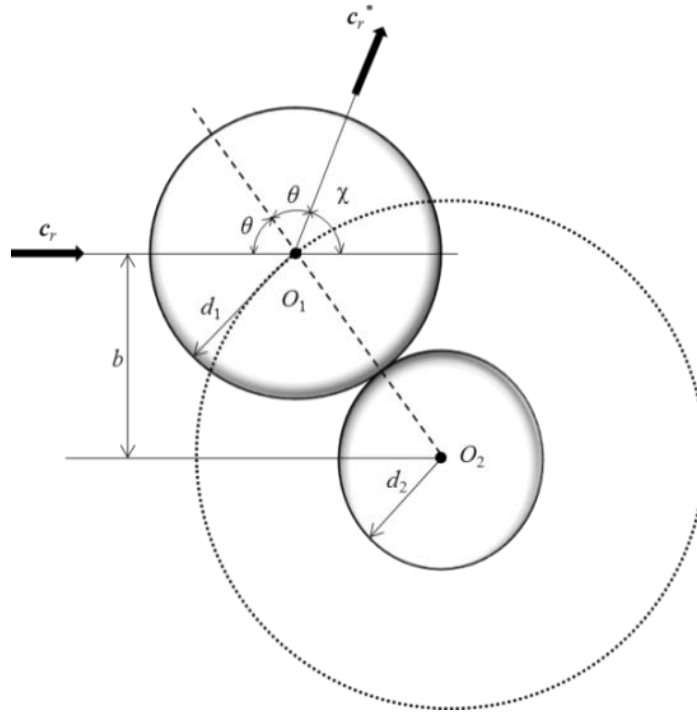


Figure 2.2: Geometric representation of the collision between two hard sphere molecules

The smallest distance  $b$  between the trajectory of molecule 1 and the center of molecule 2 before collision, and the collision cross-section  $\sigma_i$  simply read

$$b = d_{12} \cos(\chi/2), \tag{2.0}$$

$$\sigma_i = \pi d_{12}^2, \tag{2.0}$$

where  $\chi$  is the deflection angle. It is important to note that the collision cross-section  $\sigma_i$  is thus constant for a HS model. In the case of two identical molecules of diameter

$d$ , the above conditions are simplified with  $d_{12} = d$ . In practical applications, it is essential to take a value of  $d$  which ensures that the dynamic viscosity of the gas deduced from molecular data matches its real measured value. Using the Chapman-Enskog theory, the dynamic viscosity of the gas for a HS model is given by

$$\mu_{HS} = \frac{5(mkT/\pi)^{1/2}}{16d^2}, \quad (2.0)$$

If the viscosity  $\mu_{ref}$  is known at a reference temperature  $T_{ref}$ , the value of the molecular mean diameter for a HS collision model is deduced from

$$d_{HS} = \left[ \frac{5(mkT_{ref}/\pi)^{1/2}}{16\mu_{ref}} \right]^{1/2}. \quad (2.0)$$

The mean collision rate  $\nu$  for the HS model can be expressed as

$$\nu = n \overline{\sigma}_t \overline{c}_r = n\pi d^2 \overline{c}_r, \quad (2.0)$$

where  $\overline{c}_r$  is the mean relative velocity between the two molecules. For a single-component gas,  $\overline{c}_r = (2/\sqrt{\pi})\sqrt{2kT/(m/2)}$ .

From Eqs. (2.0) and (2.0), the mean free path for a HS model can read

$$\lambda = \frac{\overline{c}_r}{c_r \pi d^2 n} = \frac{1}{\sqrt{2}\pi d^2 n} \quad (2.0)$$

and it can also be expressed with macroscopic properties as:

$$\lambda = \frac{16}{5\sqrt{2}\pi} \frac{\mu}{\rho\sqrt{RT}}. \quad (2.0)$$

### VHS Model

In a HS model, the dynamic viscosity is proportional to the square root of the temperature (see Eq. (2.0)) which is not correct for a real gas. Bird (Bird 1978) proposed the variable hard sphere (VHS) model in which the molecules possess isotropic scattering probability as in the hard sphere model, but with a collisional cross-section function of the relative velocity between the molecules. The VHS model results in  $\mu \propto T^\omega$  where the coefficient  $\omega$  depends on the gas species.

VSS Model

Koura and Matsumoto (Koura et al. 1991) further introduced the variable soft sphere (VSS) model in which both the cross-section  $\sigma_i$  and the deflection angle  $\chi$  depend on the relative velocity between the molecules, which improves a bit the accuracy of the VHS model. The results from the VHS model are then slightly modified with a corrective coefficient  $\alpha$ , which depends on the gas species.

Each above described model leads to a different estimation of the mean free path of the molecules, which can be written as  $\lambda = k_2 \mu / (\rho \sqrt{RT}) = k_2 \mu \sqrt{RT} / P$ , assuming the gas is dilute and consequently ideal. The expression of coefficients  $k_2$  are resumed in Table 2.1 for different collision models.

**Table 2.1: Coefficient  $k_2$  for calculating the mean free path for different collision models**

Model	$k_2$
HS	$\frac{16}{5\sqrt{2\pi}}$
VHS	$\frac{2(7-2\omega)(5-2\omega)}{15\sqrt{2\pi}}$
VSS	$\frac{4\alpha(7-2\omega)(5-2\omega)}{5(\alpha+1)(\alpha+2)\sqrt{2\pi}}$

For sake of simplicity and to facilitate comparison between different cases, whenever qualitative results are provided in this thesis as a function of the Knudsen number, this Knudsen number is estimated from a mean free path calculated from the VHS model, with a dynamic viscosity  $\mu = \mu_{ref} \left( T/T_{ref} \right)^\omega$ , where the values of  $\omega$  and  $\mu_{ref} \left( T_{ref} \right)$  are taken from the data provided in (Bird 1994). In addition, if the gas is flowing in a channel, the reference length is its hydraulic diameter  $D_h$  and then  $Kn = \lambda/D_h$ .

### 2.1.3 Thermodynamic equilibrium

The continuum approach requires that the sampling volume, in which local macroscopic properties can be deduced from the averaging of molecular properties, is in thermodynamic equilibrium (Bird 1994). In order to respect this thermodynamic equilibrium, the collision rate inside each sampling volume must be high enough. This implies that the mean free path  $\lambda = \bar{c}'/\nu$  must be small compared with the characteristic length  $L_{sv}$  of the sampling volume, itself being small compared with the characteristic length  $L_c$  of the flow domain. As a consequence, the thermodynamic equilibrium requires that

$$\frac{\lambda}{L_c} = Kn \ll 1. \quad (2.0)$$

### 2.1.4 Gas flow regimes and main models

Usually, according to the range of the Knudsen number  $Kn$ , the gas microflows may be classified into four regimes: the continuum regime, the slip flow regime, the transitional regime and the free molecular regime. The appropriate models must be chosen according to the value of the Knudsen number. Figure 2.3 presents the gas flow regimes and their main related models.

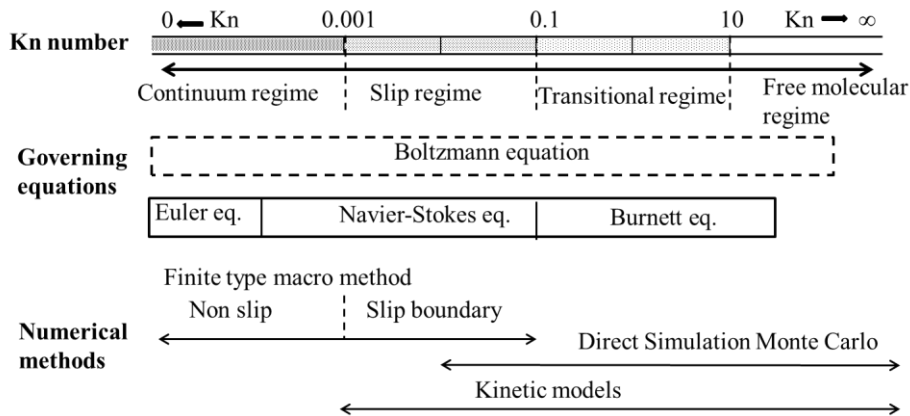


Figure 2.3: Gas flow regimes and main models according to the Knudsen number

In the continuum -or hydrodynamic- regime ( $Kn < 0.001$ ), the effect of rarefaction can be neglected and the compressible Navier-Stokes-Fourier equations with classical no-slip boundary conditions can accurately model flows in this regime.

In the slip regime ( $0.001 < Kn < 0.1$ ), with the decrease of the intermolecular collision rate compared with the rate of collisions between molecules and walls, the local thermodynamic equilibrium near the wall is broken. The Navier-Stokes-Fourier equations can still be used, but should be coupled to velocity slip and temperature jump boundary conditions, which macroscopically take into account the effects of local thermodynamic disequilibrium inside the Knudsen layer (see Fig. 2.4).

In the transitional flow regimes ( $0.1 < Kn < 10$ ), the collisions of the molecules with the walls and the intermolecular collisions have roughly equal importance. The Navier-Stokes-Fourier equations are not valid any longer. However, in the early transition regime ( $Kn < 1$ ) some extended continuum models, such as the Burnett or R13 moments equations, can allow keeping a continuum approach. The modeling of flows at higher Knudsen numbers has to be based on the resolution of the Boltzmann equation, thanks to kinetic models such as the Bhatnagar–Gross–Krook (BGK) model or by Direct Simulation Monte Carlo (DSMC).

In the free molecular flow regimes ( $Kn > 10$ ), molecules freely move without intermolecular collisions and the flow can be described by the Boltzmann equation without the collision term, which can be solved by analytical or numerical methods (Bird 1994, Sone 2007). For the typical thermal transpiration flow discussed in Section 1.1.2, the index  $\zeta$  in Eq. (1.1) is 0.5 in this free molecular flow regime.

## 2.2. Slip flow regime

### 2.2.1 Boundary conditions

Maxwell (Maxwell 1879) developed the theoretical basis for modeling the velocity slip at the wall. He postulated that when molecules collide with a surface, there are two possibilities: (i) the molecules are reflected specularly and only change the direction of their normal velocity to the wall, (ii) the molecules may have a more complex interaction with the surface and are reflected diffusely: the molecules leaving the surface scatter with an equilibrium Maxwellian distribution which is related to surface properties, such as the surface temperature and velocity. Maxwell treated the reaction between molecules and surfaces as a combination of these two reflections. A fraction  $\alpha_v$  of the molecules reflects diffusely while the complementary fraction  $1 - \alpha_v$  of the molecules reflects specularly. The coefficient  $\alpha_v$  is generally called tangential momentum accommodation coefficient (TMAC), although Sharipov



Maxwell initially derived the slip-boundary condition in terms of the shear stress and Eqs. (2.0) and (2.1) are derived from an expression of the shear stress appropriate for the simplified problem analyzed by Maxwell. Therefore Eqs. (2.0) and (2.1) are only valid for plane walls. In the case of a 2-D isothermal flow along a curved wall, the expression of slip velocity at the walls should be written as (Barber et al. 2004, Lockerby et al. 2004, Leontidis et al. 2012)

$$u_{slip} = \frac{2 - \alpha_v}{\alpha_v} \frac{\lambda}{\mu} \tau|_{wall} = \frac{2 - \alpha_v}{\alpha_v} \lambda \left( \frac{\partial u_s}{\partial n} + \frac{\partial u_n}{\partial s} \right) \Big|_{wall} \quad (2.2)$$

where  $\tau|_{wall}$  is the shear stress at the wall, and  $u_s$  and  $u_n$  are the tangential and the normal velocities. It is important to note that the additional derivative  $\partial u_n / \partial s$  must be taken into account in the case of curved walls, although in most published works this term is neglected or has been sometimes erroneously replaced with the derivative  $\partial u_s / \partial s$ . The importance of this term is discussed in Section 2.2.3.2, considering a cylindrical Couette flow.

In a similar way, the temperature jump boundary condition has been initially given by

$$T_{fluid} - T_{wall} = \frac{2 - \alpha_T}{\alpha_T} \frac{2\gamma}{\gamma + 1} \frac{\lambda}{Pr} \frac{\partial T}{\partial n} \Big|_{wall}, \quad (2.3)$$

where  $\alpha_T$  is the thermal accommodation coefficient and  $\gamma$  and  $Pr$  the ratio of the specific heats and the Prandtl number, respectively.

In order to improve the accuracy of the initial boundary conditions proposed in the literature, some authors has tried to add a corrective coefficient, calculated from numerical simulations. In a more general way, the complete velocity slip condition, including the effect of curved wall and thermal transpiration effect, as well as the temperature jump condition, can be written under the following forms:

$$u_{slip} = \sigma_p \lambda \left( \frac{\partial u_s}{\partial n} + \frac{\partial u_n}{\partial s} \right) \Big|_{wall} + \sigma_T \frac{\mu}{\rho T} \frac{\partial T}{\partial s} \Big|_{wall}, \quad (2.3)$$

$$T_{fluid} - T_{wall} = \xi_T \frac{\partial T}{\partial n} \Big|_{wall}, \quad (2.3)$$

where  $\sigma_p$  and  $\sigma_T$  are the viscous slip coefficient and the thermal slip coefficient and  $\xi_T$  is the temperature jump coefficient. These coefficients depend on the tangential

momentum and the thermal accommodation coefficients,  $\alpha_v$  and  $\alpha_T$ , directly linked to the nature of the gas and of the solid surface. They also depend on the collision model chosen for calculating the mean free path  $\lambda$ . A number of experimental (Graur et al. 2009, Rojas-Cárdenas et al. 2015) and numerical studies (Sharipov 2003) have been devoted to the calculation of the slip and jump coefficients and to their link with the accommodation coefficients; a detailed review can be found in (Sharipov 2011). In order to avoid a possible confusion due to the use of these coefficients with the estimation of the mean free path from an inappropriate collision model, Sharipov has suggested to replace the actual mean free path with a so-called equivalent mean free path  $\lambda_e = \mu\sqrt{2RT}/P$ . In that case,  $\sigma_p = 1.018$ ,  $\sigma_T = 1.175$  and  $\xi_T = 1.954$  considering complete (diffuse) accommodation.

### 2.2.2 Analytical method

An analytical solution can be obtained for a transpiration flow in a long channel of length  $L$ . Figure 2.5 shows a schematic representation of the thermal transpiration flow in a microchannel or microtube connected to two reservoirs at different temperatures, namely  $T_c$  and  $T_h$ . The channel temperature varies linearly along its surface as:  $T(z) = (T_h - T_c)z/L + T_c$ . Actually, two configurations should be considered: the closed system (a) and the constant-pressure system (b).

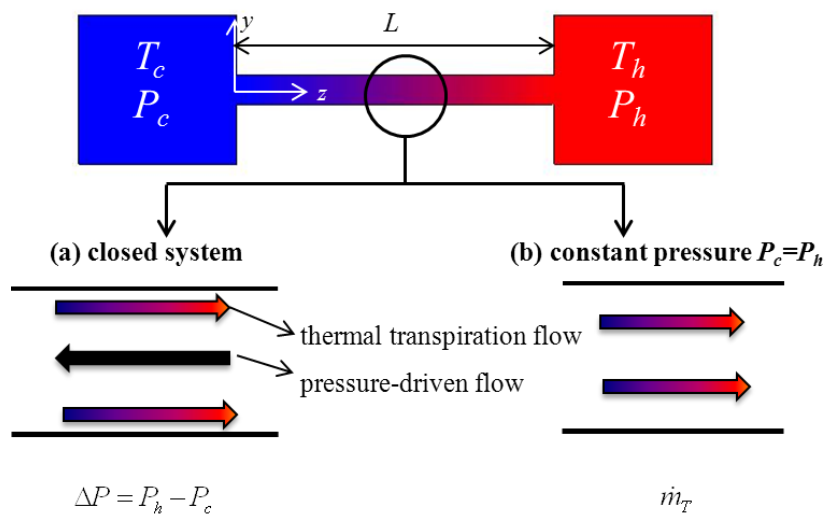


Figure 2.5: Schematic representation of transpiration flow

Let us first consider two closed reservoirs only connected by a relatively large channel whose hydraulic diameter is comparable to the mean free path. The whole system is filled with the same gas at a uniform initial pressure. At the beginning, the gas near the walls starts to creep from the cold reservoir to the hot one due to a temperature gradient along the channel and then the creeping fluid layer starts interacting with the stagnant fluid around it. As more fluid is introduced into the hot reservoir, the pressure increases inside while it decreases in the cold reservoir. Thus, an opposite flow, driven by this pressure difference, starts. Finally, the system reaches a steady state when the thermal transpiration flow and pressure-driven flow are balanced. The final pressure difference  $\Delta P = P_h - P_c$  is generated.

When the dimensions of the two reservoirs can be considered as infinite or if they are connected secondly by a tube with much larger hydraulic diameter than the microchannel one, the pressure in the two reservoirs can be kept constant. In this case, a steady state thermal transpiration flow from the cold side to the hot side is created and a net mass flowrate can be calculated.

A rectangular channel is now considered, whose width  $W$  is much larger than its height  $H$  and whose length  $L$  is much larger than  $H$  so that the end effects can be neglected. With this assumption, the gas velocity has only one component  $u_z$  satisfying the equation (Sharipov 2011):

$$\mu \frac{\partial^2 u_z}{\partial y^2} = \frac{\partial P}{\partial z} . \quad (2.4)$$

When  $\frac{\partial P}{\partial z} = 0$ , imposing the boundary condition  $u_{slip} = \sigma_T \frac{\mu}{\rho T} \frac{\partial T}{\partial s} \Big|_{wall}$  on the walls, the mass flowrate only due to the thermal transpiration effect is

$$\dot{m}_T = \sigma_T \frac{W H \mu}{T} \frac{\partial T}{\partial z} . \quad (2.5)$$

As mentioned before, the flow due to the temperature gradient goes from the cold reservoir to the hot reservoir, which leads to a pressure difference the between two chambers and a reversed Poiseuille flow. Considering the boundary condition

$u_{slip} = \sigma_P \lambda \frac{\partial u}{\partial n} \Big|_{wall}$ , the mass flowrate only due to the pressure gradient reads,

following the integration of Eq. (2.4):

$$\dot{m}_p = -\frac{W H^3 \rho}{12\mu} (1 + 6\sigma_p Kn) \frac{dP}{dz} \quad (2.6)$$

For the closed configuration (Fig 2.5a), a steady state with zero net flowrate can be eventually reached, when the mass flowrate due to the thermal transpiration is equal to the one due to the pressure gradient in every section of the channel. Eqs. (2.5) and (2.6) thus give:

$$\frac{H^2 \rho}{12\mu} (1 + 6\sigma_p Kn) \frac{\partial P}{\partial z} = \sigma_T \frac{\mu}{T} \frac{\partial T}{\partial z} . \quad (2.7)$$

This equation can be numerically solved using the scheme

$$P_{i+1} - P_i = \frac{12\sigma_T \mu_{(T_i)}^2 R}{H_i^2 P_i (1 + 6\sigma_p Kn_i)} (T_{i+1} - T_i), \quad (2.8)$$

where  $H_i$ ,  $P_i$ ,  $T_i$  and  $Kn_i$  are the channel height, pressure, temperature and Knudsen number, respectively, at the  $i^{th}$  node ( $i = 0, \dots, N$ ) of the channel uniformly discretized in the  $z$ -direction. The total pressure difference is then given by  $P_N - P_0$ .

For the open configuration shown in Fig. 2.5b, in which  $P_h = P_c = const.$ , the pressure along the channel is not uniform although the pressures at the ends of the channel are equal and constant. The net mass flowrate can be written as:

$$\dot{m} = -\frac{W H^3 \rho}{12\mu} (1 + 6\sigma_p Kn) \frac{\partial P}{\partial z} + \sigma_T \frac{\mu W H}{T} \frac{\partial T}{\partial z} . \quad (2.9)$$

In a similar way, this equation can be discretized as :

$$\dot{m} = \dot{m}_i = -\frac{W H_i^3 \rho_i}{12\mu_i} (1 + 6\sigma_p Kn_i) \frac{P_{i+1} - P_i}{\Delta z} + \sigma_T \frac{\mu_i W H_i}{T_i} \frac{T_{i+1} - T_i}{\Delta z} . \quad (2.10)$$

The mass flowrate  $\dot{m}$  is determined by satisfying the pressure conditions at the ends of channel, i.e.  $P_0 = P_c = P_N = P_h = const.$ . The pressure  $P_0$  at the inlet is given and a value of the mass flowrate  $\dot{m} (> 0)$  is preset; therefore from Eq. (2.10) the pressure  $P_i$  in every node is obtained. Comparing the obtained pressure at the outlet  $P_N$  with the real value  $P_h$ , if  $P_N \neq P_h$ , the value of  $\dot{m}$  is corrected with a small increment  $\Delta \dot{m}$ . The loop is executed until  $P_N = P_h$ .

The present analytical model is inspired by kinetic models implemented to analyze rarefied gas flows through a long tube (or channel) with variable cross-section

(Sharipov et al. 2005, Graur et al. 2014). Equations (2.8) and (2.10) are also valid for a divergent/convergent channel, where  $H_i \neq const$ . Therefore, this model will be used to investigate a thermal transpiration flow through a tapered channel in Chapter 3.

For a fully developed flow in a long tube with a circular cross section of radius  $a$ , Eqs. (2.8) and (2.9) take the following form:

$$P_{i+1} - P_i = \frac{8\sigma_T \mu_{(T_i)}^2 R}{a^2 P_i (1 + 4\sigma_p Kn_i)} (T_{i+1} - T_i) , \quad (2.11)$$

$$\dot{m} = -\frac{\pi a^4 \rho}{8\mu} (1 + 4\sigma_p Kn) \frac{\partial P}{\partial z} + \sigma_T \frac{\mu \pi a^2}{T} \frac{\partial T}{\partial z} . \quad (2.12)$$

The data provided by the above analytical model will be compared to experimental data in Chapter 6.

### 2.2.3 Numerical method

A 2D numerical method has been developed in this thesis by developing specific User Defined Functions (UDF) to implement the appropriate velocity slip and temperature jump boundary conditions in ANSYS Fluent® CFD code.

#### Solver

The numerical modeling has been carried out using the CFD code ANSYS Fluent®, which implements the finite-volume method. The velocity slip boundary condition is imposed as the velocity of a moving wall, and the temperature jump as a modified temperature of the wall, both of them applied cell by cell at the wall. For that reason User Defined Functions have been developed by means of C++ routines and compiled in the solver. Through the UDF the derivatives of the velocities and the temperature are extracted from the solver and the slip velocity and temperature jump are calculated from Eqs. (2.3) and (2.3). In addition, the temperature of the walls is imposed with the UDF, either as a constant temperature or as a temperature gradient when needed.

Due to the surface curvature, the local wall coordinate system is in general not aligned with the solver's coordinate system. This induces a necessary transformation to express in the local coordinate system  $(s, n)$  the velocity vectors and all derivatives, extracted from the Cartesian coordinate system  $(x, y)$  used by the solver (see Fig. 2.6).

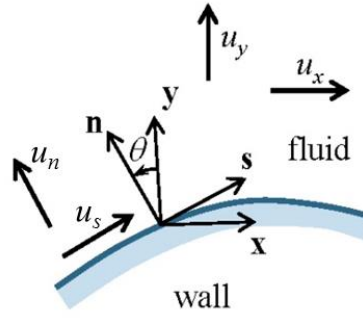


**Figure 2.6:** Cartesian and local coordinate systems at the wall and velocity components.

First of all, the rotation angle  $\theta$  between both coordinate systems is determined at every cell of the wall by

$$\begin{cases} \theta = \arccos \frac{-\mathbf{A} \cdot \mathbf{y}}{\|\mathbf{A}\|} & \text{if } \mathbf{A} \cdot \mathbf{x} \geq 0 \\ \theta = 2\pi - \arccos \frac{-\mathbf{A} \cdot \mathbf{y}}{\|\mathbf{A}\|} & \text{if } \mathbf{A} \cdot \mathbf{x} < 0 \end{cases} \quad (2.13)$$

where  $\mathbf{A} = -A\mathbf{n}$  is the area normal vector provided by Fluent® and  $A$  is the surface area of the cell. The derivative terms required in Eqs. (2.3) and (2.3) can then be obtained with:

$$\begin{aligned} \frac{\partial u_s}{\partial n} &= \nabla u_s \cdot \mathbf{n} = -\left(\frac{\partial u_x}{\partial x} \cos \theta + \frac{\partial u_y}{\partial x} \sin \theta - u_x \sin \theta \frac{\partial \theta}{\partial x} + u_y \cos \theta \frac{\partial \theta}{\partial x}\right) \sin \theta \\ &+ \left(\frac{\partial u_x}{\partial y} \cos \theta + \frac{\partial u_y}{\partial y} \sin \theta - u_x \sin \theta \frac{\partial \theta}{\partial y} + u_y \cos \theta \frac{\partial \theta}{\partial y}\right) \cos \theta \end{aligned} \quad (2.14)$$

$$\begin{aligned} \frac{\partial u_n}{\partial s} &= \nabla u_n \cdot \mathbf{s} = \left(-\frac{\partial u_x}{\partial x} \sin \theta + \frac{\partial u_y}{\partial x} \cos \theta - u_x \cos \theta \frac{\partial \theta}{\partial x} - u_y \sin \theta \frac{\partial \theta}{\partial x}\right) \cos \theta \\ &+ \left(-\frac{\partial u_x}{\partial y} \sin \theta + \frac{\partial u_y}{\partial y} \cos \theta - u_x \cos \theta \frac{\partial \theta}{\partial y} - u_y \sin \theta \frac{\partial \theta}{\partial y}\right) \sin \theta \end{aligned} \quad (2.15)$$

$$\frac{\partial T}{\partial s} = \nabla T \cdot \mathbf{s} = \frac{\partial T}{\partial x} \cos \theta + \frac{\partial T}{\partial y} \sin \theta \quad (2.16)$$

$$\frac{\partial T}{\partial n} = \nabla T \cdot \mathbf{n} = -\frac{\partial T}{\partial x} \sin \theta + \frac{\partial T}{\partial y} \cos \theta \quad (2.17)$$

All velocity and temperature derivatives ( $\partial u_x/\partial x$ ;  $\partial u_x/\partial y$ ;  $\partial u_y/\partial x$ ;  $\partial u_y/\partial y$ ;  $\partial T/\partial x$ ;  $\partial T/\partial y$ ) in Eqs. (2.14)-(2.17) are extracted from the solver and the angle

derivatives  $\partial\theta/\partial x$  and  $\partial\theta/\partial y$  are calculated after determining the local curvature radius

$$r = \frac{\|\mathbf{BC}\|}{2\sqrt{1 - \left(\frac{\mathbf{AC} \cdot \mathbf{AB}}{\|\mathbf{AC}\|\|\mathbf{AB}\|}\right)^2}} \quad (2.18)$$

where A, B and C are the locations of 3 successive nodes at the wall (see Fig. 2.7).

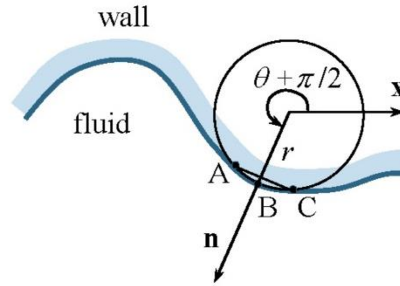


**Figure 2.7:** Osculating circle at the wall for determination of  $\theta$  derivatives.

The angle derivatives are then obtained with:

$$\frac{\partial\theta}{\partial x} = -\frac{\mathbf{n} \cdot \mathbf{AB}}{|\mathbf{n} \cdot \mathbf{AB}| r \cos \theta}, \quad (2.19)$$

$$\frac{\partial\theta}{\partial y} = -\frac{\mathbf{n} \cdot \mathbf{AB}}{|\mathbf{n} \cdot \mathbf{AB}| r \sin \theta}. \quad (2.20)$$

All previous equations are treated with UDF and are applicable whatever the shape of the wall. The deduced slip velocity calculated by Eqs. (2.3) and (2.3) is imposed on the wall as a moving wall velocity of components  $u_{x,wall} = u_{slip} \cos \theta$  and  $u_{y,wall} = u_{slip} \sin \theta$ . The temperature jump is imposed as a modified temperature of the wall.

All calculations in this thesis are performed with the two-dimensional segregated solver assuming laminar flows. A second order upwind spatial discretization scheme is applied. The gas is considered as a dilute and ideal compressible gas, while the temperature-dependent viscosity is calculated from a power law based on a variable hard sphere collision model.

It is worth mentioning that the CFD code ANSYS Fluent® gives the possibility of implementing first-order slip and temperature jump boundary conditions, with the so-called Low Pressure Boundary Slip (LPBS) method. The choice of velocity slip boundary condition is, however, limited to Maxwell's first-order condition, without taking into account the effects of the wall curvature and of the thermal transpiration. In addition, the mean free path can only be adjusted through the Lennard-Jones length. The validity of the LPBS method was tested for the simplest case of pressure driven gas flows in straight microchannels, and comparisons with analytical solutions, which can be found in the literature (Kandlikar et al. 2005), showed a very good global agreement. It has been shown, however, that the obtained results are not always locally very accurate, especially in three-dimensional flows with cross-sections involving acute angles (Pitakarnnop et al. 2008). To overcome these drawbacks, specific UDF have been developed in the present work.

Validation: cylindrical Couette flow

Cylindrical Couette flow in the continuum regime is a classical problem that is addressed in many fluid dynamics textbooks. However, under certain conditions of rarefaction, in particular when the accommodation coefficient is small, the velocity profile between the cylinders can exhibit a curious behavior: for example, when the inner cylinder is rotating and the outer cylinder is stationary, it is possible to obtain an inverted velocity profile where the velocity increases unexpectedly from the rotating inner cylinder to the stationary outer cylinder (Tibbs et al. 1997, Barber et al. 2004, Dinler et al. 2012, Dongari et al. 2013). The same configuration than that studied by Barber (Barber et al. 2004) is here considered. An inner cylinder of radius  $R_1 = 3\lambda$  rotates at a constant angular velocity  $\omega_1$  and an outer cylinder of radius  $R_2 = 5\lambda$  is stationary. The corresponding Knudsen number based on the distance between the two cylinders is then  $Kn = 0.5$ . Both cylinders are maintained at the same temperature and therefore the flow is considered as isothermal. A numerical model with UDF that implement full first order slip boundary conditions and another one that ignores the derivative  $\partial u_n / \partial s$  are used to comparatively investigate this problem.

Figures 2.8 and 2.9 present the non-dimensional velocity  $u_s^* = u_s / (R_1 \omega_1)$  profiles obtained by the UDF compared with analytical (Barber et al. 2004) and DSMC (Tibbs et al. 1997) results for two values of the tangential momentum accommodation

coefficient,  $\alpha_v = 1$  and  $\alpha_v = 0.1$ . It is found that the results calculated by our CFD model with complete UDF taking into account the term  $\partial u_s / \partial n$  agree well with the corresponding analytical data. A small deviation with DSMC data naturally appears because when the Knudsen number reaches relatively high values such as 0.5, the continuum approach becomes less accurate.

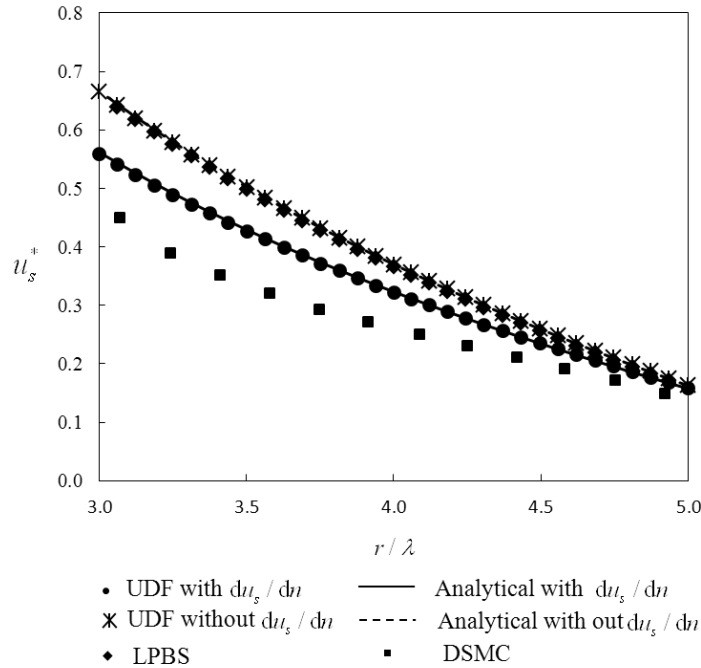


Figure 2.8: Non-dimensional velocity profiles for cylindrical Couette flow ( $\alpha_v = 1$ )

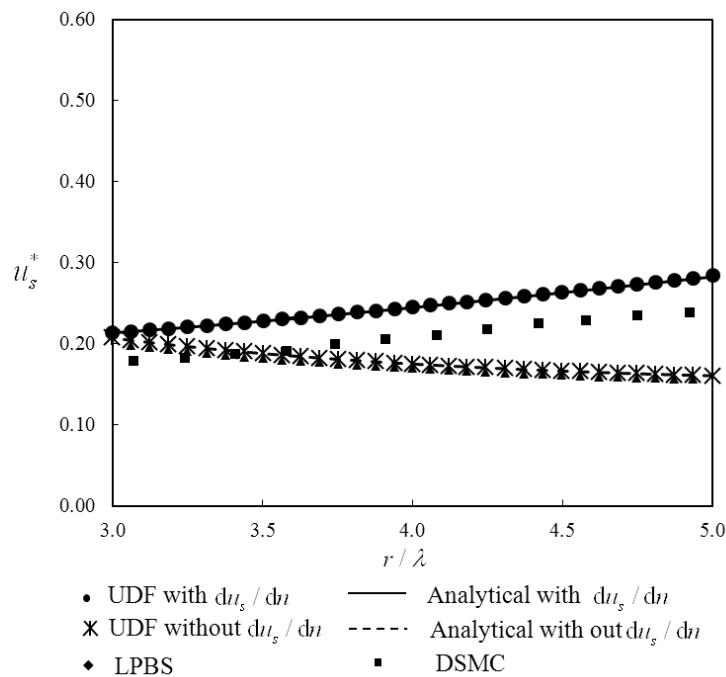
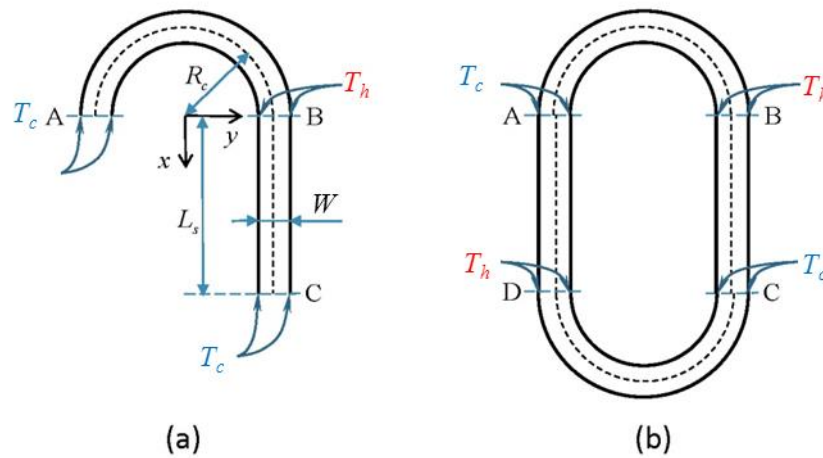


Figure 2.9: Non-dimensional velocity profiles for cylindrical Couette flow ( $\alpha_v = 0.1$ )

For  $\alpha_v = 0.1$ , the so-called inverted velocity profile is observed when the effect of curved wall is taken into account and it is not captured when the term  $\partial u_s / \partial n$  is ignored. This later case, with UDF ignoring the term  $\partial u_s / \partial n$ , provides results close to those directly obtained with the standard LPBS method proposed in Fluent®, where the Lennard-Jones coefficients have been adjusted to provide the same boundary conditions as  $u_{slip} = \sigma_p \lambda (\partial u_s / \partial n)|_{wall}$ , with  $\sigma_p = 1.0$ .

Validation: temperature driven flows in ringed shaped channels

In this section, the layout proposed by Aoki et al. (Aoki et al. 2008, Aoki et al. 2009) is considered. The complete expressions of the boundary conditions, as described by Eqs. (2.3) and (2.3) are used. The basic unit of the simulated device consists of a straight channel with length  $L_s$  connected to a semi-circular channel with a centerline radius  $R_c$  (Fig. 2.10a). The width of the straight and bent channels is  $W$ . A constant temperature gradient is applied along the straight walls and the temperature is increasing from  $T_c$  to  $T_h$ . An opposite constant temperature gradient is applied along the curved walls. By completing the unit drawn in Fig. 2.10a with a symmetrical part, a closed ring can be designed (Fig. 2.10b). It has been proved with theoretical approaches by Aoki and co-workers that a circulating flow is generated inside the ring. Using the Boltzmann-BGK model, they have developed numerical methods based either on the asymptotic technique of the diffusion approximation (Aoki et al. 2008) or on a deterministic finite volume scheme (Aoki et al. 2009).



**Figure 2.10:** a) curved and straight microchannel geometry, b) ring-shaped configuration.

The geometry of the ring is symmetric with respect to the center of the ring, which allows simulating only the unit represented in Fig. 2.10a. Periodic boundary conditions are applied at the inlet and outlet sections A and C, expressed as  $T_A = T_C$  and  $P_A = P_C$ . The steady state 2-D compressible flow of an ideal gas is simulated and the results are compared with the numerical simulations of Aoki et al. (Aoki et al. 2009).

Three different layouts are tested, the parameters of which are presented in Table 2.2. In Aoki's simulations, the system is not a microsystem, but a larger device operating under very low pressures, which ensures that the gas is in rarefied conditions. The pressure in the inlet is  $P_A = P_C = 0.15$  Pa and the hot and cold temperatures are  $T_h = 900$  K and  $T_c = 300$  K, respectively. The gas is argon with a molecular weight  $M = 39.95 \times 10^{-3}$  kg mol<sup>-1</sup>. The Knudsen numbers  $Kn = \lambda/W$  are the same for each considered case, as the width  $W$  is kept constant. The Knudsen number based on the average density within the device is  $Kn = 0.1$ , and when it is calculated for the entrance conditions, its value is  $Kn_A = 0.04$ . In addition, the length of the curved part is the same as the one of the straight part, and the ratio  $L_s/W$  is increased from case 1 to case 3, which results in a reduced curvature of the curved part.

**Table 2.2: Simulation parameters of thermal transpiration flow in a curved channel and mass flowrates calculated by the present UDF method and the numerical simulations of Aoki et al. (Aoki et al. 2009).**

Case	1	2	3
$W$ (m)	1	1	1
$L_s$ (m)	3.14	6.28	15.7
$R_c$ (m)	1	2	5
	<b>Mass flowrate (<math>10^{-8}</math> kg s<sup>-1</sup> m<sup>-1</sup>)</b>		
(Aoki et al. 2009)	79.645	8.833	0.511
UDF	77.943	8.897	0.520
<b>Deviation (%)</b>	<b>1.79</b>	<b>0.720</b>	<b>1.761</b>

The channel is meshed with 200×200 cells for case 1, 200×100 cells for case 2 and 400×100 cells for case 3. In all cases the grid is progressive in the spanwise direction with an increased density near the walls. Grid independence has been checked for

each case by comparison with results obtained with finer and coarser meshes. The deviation between the mass flowrates per unit of depth calculated by the UDF method and by the simulations of Aoki et al. is very low, of the order of 1 %, although the rarefaction is already significant (see Table 2.2).

The importance of the term  $\partial u_n / \partial s$  in Eq. (2.3) is estimated here for the conditions of case 1 from Table 2.2. For the thermal transpiration flow, the second term on the right hand side of Eq. (2.3), due to the temperature gradient, is preponderant compared with the first term. The absence of  $\partial u_n / \partial s$ , which is smaller than  $\partial u_s / \partial n$  for this case, has not led to significant changes on the mass flowrate and the pressure distribution. However, for accurate calculations, this term should be considered. For example, an isothermal pressure driven flow in the same geometrical configuration than in case 1 is simulated with  $P_A = 0.06$  Pa ,  $P_C = 0.061$  Pa ,  $T_A = T_B = T_C = 300$  K and a Knudsen number  $Kn = 0.1$ . Slip velocities along the inner wall of the curved channel are shown in Fig. 2.11, where  $s^* = s / (2L_s)$  is the dimensionless curvilinear abscissa along the centerline from A to B. It is found that the slip velocity is overestimated of 8 % to 15 % when  $\partial u_n / \partial s$  is neglected in Eq. (2.3).

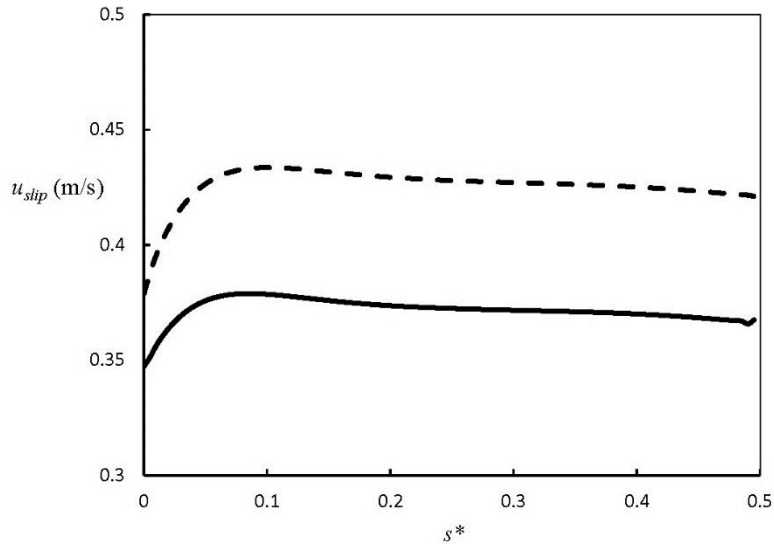


**Figure 2.11:** Slip velocity along the inner wall of the curved channel for isothermal flow in geometrical case 1, with  $P_A = 0.06$  Pa ,  $P_C = 0.061$  Pa ,  $T = 300$  K and  $Kn_C = 0.1$ . The dashed line does not take the term  $\partial u_n / \partial s$  from Eq. (2.3) into account but the solid line does.

### 2.3. Transitional regime - DSMC simulation

#### 2.3.1 DSMC simulation

The direct simulation Monte-Carlo (DSMC) method developed by Bird is widely used in the transition flow regime and has achieved great success. The DSMC method models the gas flow using a set of test molecules (simulators), each of them representing a large number of real molecules. Simulators move and collide in a probabilistic simulation in accordance with the rarefied gas dynamics theory. A fundamental assumption of the DSMC method is that the real process of molecular free movement and intermolecular collisions can be approximated by decoupling it into two consecutive steps over time intervals smaller than the mean collision time. The Flow chart of the DSMC method is shown in Fig. 2.12.

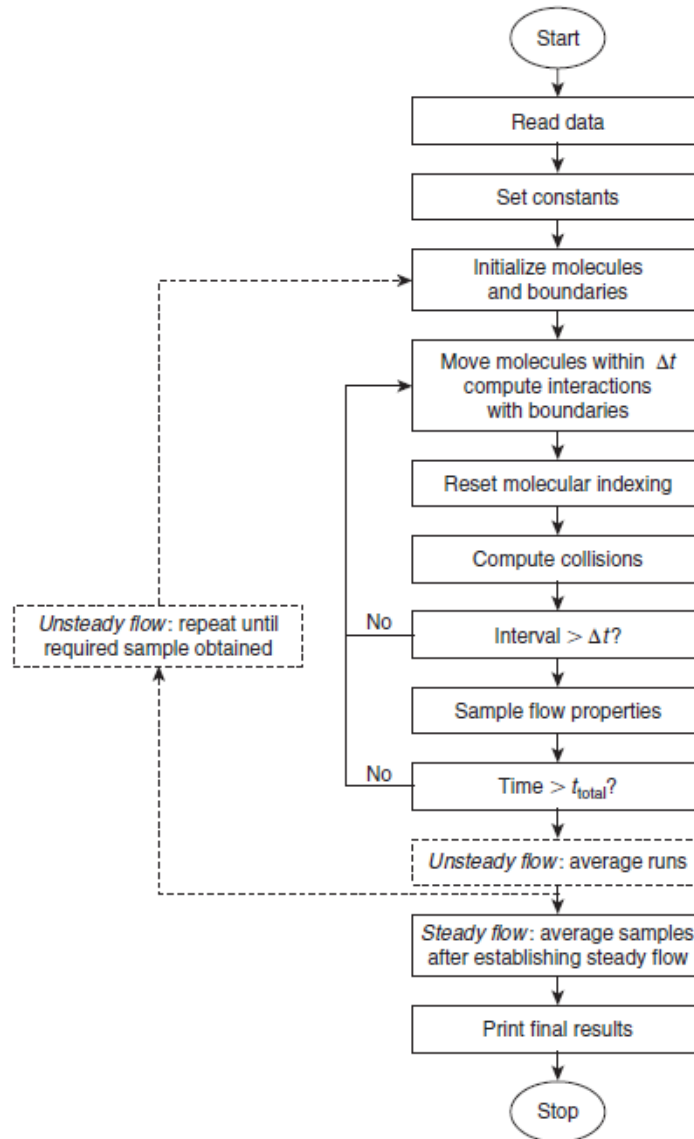


Figure 2.12: DSMC flow chart (Oran et al. 1998)

All details about the DSMC method could be found in books written by Bird (Bird 1978, Bird 1994) or other authors (Oran et al. 1998, Shen 2006). Here, we just simply discuss several key points.

Recently, Stefanov proposed other collision algorithms based on the Kac's stochastic gas model (Stefanov 2012) for simulation of the binary collision process in a homogenous rarefied gas. These collision algorithms avoid repeated collisions and can be used for simulation of the collisions in grid cells with a small average number of particles.

### 2.3.2 *dsmcFoamStrath*

The DSMC code named *dsmcFoamStrath* has been developed within the framework of the open source CFD toolbox OpenFOAM (White et al. 2013). OpenFOAM is a flexible set of efficient, object-oriented C++ modules for solving complex fluid flows. The *dsmcFoamStrath* code is based on Bird's original formulation and has been validated by several benchmark tests for high speed rarefied gas flows (Scanlon et al. 2010, White et al. 2013). The open source nature of the code, its unlimited parallel solution capability, and its potential application to arbitrary geometries are highlighted.

### 2.3.3 DSMC with decomposition of the solution into ballistic and collision parts

A DSMC method combining a novel solution decomposition into ballistic and collisions parts was recently introduced and used to investigate a rarefied gas flow in a rectangular enclosure induced by non-isothermal walls (Vargas et al. 2014) and the Knudsen paradox in long capillaries (Tatsios et al. 2015).

In general, a kinetic solution at one point in a flow domain can be decomposed in two parts, namely the ballistic and collision parts. The former one is due to particles arriving at this point from walls with no intermediate intermolecular collision and the latter one is due to particles arriving after at least one intermolecular collision. This idea of decomposition was implemented in a typical DSMC algorithm by introducing a suitable indexation process of the molecules simulators (Vargas et al. 2014). An indicator  $I_j$  (for  $j=1, \dots, N_T$ ) marks each sampled molecule –or simulator– used in the simulation, the total number of which is noted  $N_T$ . The indicator  $I_j$  has the value

0 or 1 indicating if a simulator contributes to the ballistic or to the collision part of the distribution, respectively, and the value may be changed at any time during the simulation. At the beginning of each time step, the indicator is set to 0. The indicator is not changed in case of free motion of the simulator and it is changed to 1 if the simulator is involved in any binary collision (once or several times). In the sampling stage of the macroscopic properties, all particles with indicators  $I_j = 0$  are considered as belonging to the ballistic part of the particle distribution and all particles with indicators  $I_j = 1$  to the collision part. The macroscopic quantities such as the number density  $n$  and the velocity components, e.g.  $u_x$ , corresponding to the ballistic (index  $b$ ) and collision (index  $c$ ) parts, are computed from the summations:

$$n^{(b)} = \frac{1}{N_T} \sum_{k=1}^S \sum_{i=1}^{N(t_k)} (1 - I_i(t_k)), \quad n^{(c)} = \frac{1}{N_T} \sum_{k=1}^S \sum_{i=1}^{N(t_k)} I_i(t_k) \quad (2.21)$$

$$u_x^{(b)} = \frac{1}{N_T} \sum_{k=1}^S \sum_{i=1}^{N(t_k)} (1 - I_i(t_k)) c_{x,i}(t_k), \quad u_x^{(c)} = \frac{1}{N_T} \sum_{k=1}^S \sum_{i=1}^{N(t_k)} I_i(t_k) c_{x,i}(t_k) \quad (2.22)$$

where  $S$  denotes the number of samples,  $t_k$  indicates the different times over which the sampling is performed, and  $N(t_k)$  is the number of particles in the cell at time  $t_k$ .

As a result, the total number of all particles accumulated in a cell is divided into two groups and the macroscopic quantities are sampled into the two corresponding parts:

$$n(x, y) = n^{(b)}(x, y) + n^{(c)}(x, y), \quad (2.23)$$

$$u_x(x, y) = u_x^{(b)}(x, y) + u_x^{(c)}(x, y), \quad (2.24)$$

$$u_y(x, y) = u_y^{(b)}(x, y) + u_y^{(c)}(x, y). \quad (2.25)$$

This novel analysis method can provide more information than typical DSMC simulations. In the case of an isothermal pressure-driven flow through long capillaries, it was quantitatively confirmed that the difference observed between the ballistic and collision flowrates contributions analyzed as a function of the rarefaction parameter can provide a clear explications of the Knudsen minimum of the overall flowrate (Vargas et al. 2014). The streamlines and velocity contours of the ballistic and collision parts in the case of a thermally-driven flow in an enclosure were shown in (Vargas et al. 2014). It was demonstrated that at small Knudsen numbers the

collision part dominates and the classical thermal transpiration theory works, while at large Knudsen numbers the ballistic part prevails and then the gas flows along the wall from hot to cold regions.

In collaboration with one of the authors of the papers cited in this section, Professor Stefanov from the Bulgarian Academy of Sciences, a home code specially developed for studying a ratchet pump has been developed and is presented in Chapter 5. This code based on a standard DSMC procedure includes the novel decompositions analysis method.

#### 2.3.4 Validation: thermally-driven flow in a closed rectangular channel

The considered geometry for this validation is a microchannel with a rectangular cross-section, closed at both ends. The height  $H$  of the channel is assumed to be much larger than its width  $W$ , allowing to consider only two dimensions: a length  $L$  in the  $z$ -direction and a width  $W$  in the  $y$ -direction. The two ends (denoted by subscripts  $c$  at the left and  $h$  at the right) of the channel are maintained at two different temperatures:  $T_c = 273$  K and  $T_h = 573$  K. The temperature of the side walls varies linearly along the length of the channel and the working gas (argon) is initially in thermal equilibrium with the walls (i.e.  $T_0(y, z) = T_c + (T_h - T_c)z/L$ ) and at a uniform atmospheric pressure (i.e.  $P_0(y, z) = Cte = 10^5$  Pa). The length over width ratio of the channel is fixed to 5 and three values of the width are considered:  $W = [1 \mu\text{m}; 100 \text{ nm}; 20 \text{ nm}]$ , which corresponds to mean Knudsen numbers  $Kn = [0.06; 0.64; 3.20]$ , respectively. Both previously described codes (*dsmcFoamStrath* code and the code including the decomposition method) are used to study this problem. Pressure distributions along the centerline of the channel are shown for the three cases in Fig. 2.13 and compared with the results obtained by Masters and Ye (Masters et al. 2007). A very good agreement is observed.

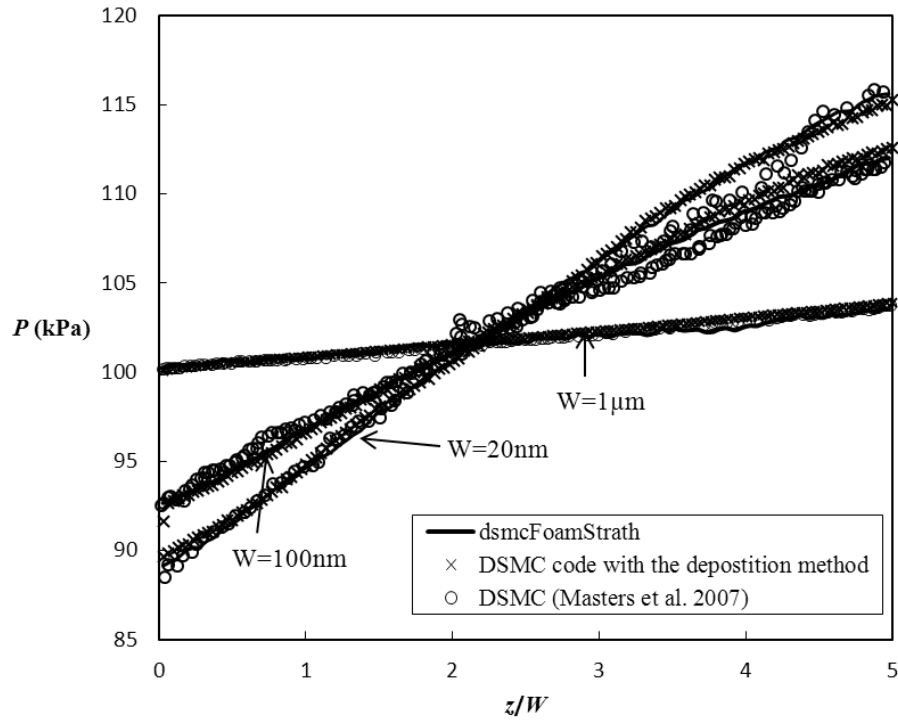
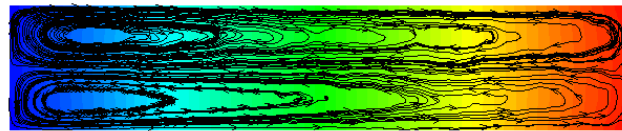
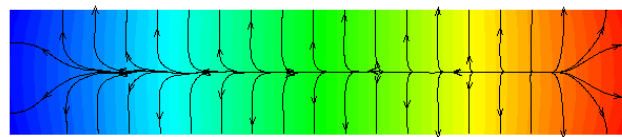


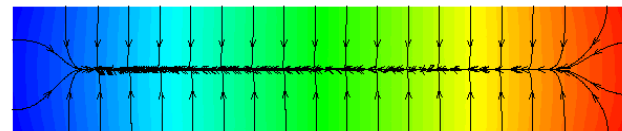
Figure 2.13: Pressure distribution along the centerline of the channel compared with DSMC results from (Masters et al. 2007)



(a)



(b)



T: 280 305 330 355 380 405 430 455 480 505 530 555

(c)

Figure 2.14: Streamlines of the overall flow (a), of the collision part of the flow (b) and of the ballistic part of the flow (c), for case 1. The colors show the temperature fields.

The “ballistic” streamlines and the “collision” streamlines have opposed directions and the flow patterns of these two parts are totally different from the overall pattern shown in Fig 2.14a. This case could be regarded as a special case of the study presented in (Vargas et al. 2014) with an aspect ratio of 5; more in-depth discussion can be found in this paper.

## **2.4. Summary**

In this chapter, general points about modeling of rarefied gas flows and the main numerical models according to the Knudsen number range were introduced. For slip flow, an analytical model of a simple thermal transpiration flow between two plane plates or through a long tube has been presented. A 2-D numerical model has been developed, based on the commercial CFD code ANSYS Fluent® with specific UDF derived to implement accurate slip boundary conditions. This model has been validated with two benchmark problems: the cylindrical Couette flow and the thermal transpiration flow in a ringed shaped channel. It will be used to design Knudsen pumps in the following chapters. In the transition flow regime, the DSMC method, which is widely and successfully used in various configurations in this regime, has been introduced. Based on the typical DMSC model proposed by Bird, two codes are explored in this thesis. The first one is the open source code *dsmcFoamStrath* which can be used for arbitrary geometries. The other one is a home code developed in collaboration with Professor Stefanov, more specifically for studying the ratchet pump presented further in Chapter 5. This code includes a novel decomposition analysis method which can provide more detailed information to understand the physics of the flows.

## **References**

- Aoki, K., Degond, P. and Mieussens, L. (2009). "Numerical simulations of rarefied gases in curved channels: thermal creep, circulating flow, and pumping effect." *Communications in Computational Physics* 6(5): 911-954.
- Aoki, K., Degond, P., Mieussens, L., et al. (2008). "A Diffusion Model for Rarefied Flows in Curved Channels." *Multiscale Modeling & Simulation* 6(4): 1281-1316.
- Barber, R. W., Sun, Y., Gu, X. J., et al. (2004). "Isothermal slip flow over curved surfaces." *Vacuum* 76(1): 73-81.

- Bird, G. (1978). "Monte Carlo simulation of gas flows." *Annual Review of Fluid Mechanics* 10: 11-31.
- Bird, G. A. (1994). *Molecular gas dynamics and the direct simulation of gas flows*. Oxford, Clarendon Press
- Colin, S. (2013). *Single-phase gas flow in microchannels. Heat transfer and fluid flow in minichannels and microchannels*, Elsevier: 11-102.
- Dinler, A., Barber, R. W., Emerson, D. R., et al. (2012). "Role of surface shape on boundary slip and velocity defect." *Physical Review E* 86(1): 016314.
- Dongari, N., Barber, R., Emerson, D., et al. (2013). "The effect of Knudsen layers on rarefied cylindrical Couette gas flows." *Microfluidics and Nanofluidics* 14(1-2): 31-43.
- Graur, I. and Ho, M. T. (2014). "Rarefied gas flow through a long rectangular channel of variable cross section." *Vacuum* 101(0): 328-332.
- Graur, I., Perrier, P., Ghazlani, W., et al. (2009). "Measurements of tangential momentum accommodation coefficient for various gases in plane microchannel." *Physics of Fluids (1994-present)* 21(10): 102004.
- Kandlikar, S., Garimella, S., Li, D., et al. (2005). *Heat transfer and fluid flow in minichannels and microchannels*, Elsevier.
- Koura, K. and Matsumoto, H. (1991). "Variable soft sphere molecular model for inverse - power - law or Lennard - Jones potential." *Physics of Fluids A* 3(10): 2459-2465.
- Leontidis, V., Brandner, J. J., Baldas, L., et al. (2012). "Numerical analysis of thermal creep flow in curved channels for designing a prototype of Knudsen micropump." *Journal of Physics: Conference Series-1st European Conference on Gas Micro Flows (GasMems 2012)* 362(1): 012004.
- Lockerby, D. A., Reese, J. M., Emerson, D. R., et al. (2004). "Velocity boundary condition at solid walls in rarefied gas calculations." *Physical Review E* 70(1): 017303.
- Masters, N. D. and Ye, W. (2007). "Octant flux splitting information preservation DSMC method for thermally driven flows." *Journal of Computational Physics* 226(2): 2044-2062.
- Maxwell, J. C. (1879). "On stresses in rarefied gases arising from inequalities of temperature." *Phil. Trans. R. Soc.* 170: 231-256.
- Oran, E. S., Oh, C. K. and Cybyk, B. Z. (1998). "DIRECT SIMULATION MONTE CARLO: Recent Advances and Applications." *Annual Review of Fluid Mechanics* 30(1): 403-441.
- Pitakarnnop, J., Geoffroy, S., Colin, S., et al. (2008). "Slip flow in triangular and trapezoidal microchannels." *International Journal of Heat and Technology* 26: 167-174.
- Rojas-Cárdenas, M., Graur, I., Perrier, P., et al. (2015). "A new method to measure the thermal slip coefficient." *International Journal of Heat and Mass Transfer* 88: 766-774.

- Scanlon, T. J., Roohi, E., White, C., et al. (2010). "An open source, parallel DSMC code for rarefied gas flows in arbitrary geometries." *Computers & Fluids* 39(10): 2078-2089.
- Sharipov, F. (2003). "Application of the Cercignani–Lampis scattering kernel to calculations of rarefied gas flows. II. Slip and jump coefficients." *European Journal of Mechanics - B/Fluids* 22(2): 133-143.
- Sharipov, F. (2011). "Data on the Velocity Slip and Temperature Jump on a Gas-Solid Interface." *Journal of Physical and Chemical Reference Data* 40(2): 023101.
- Sharipov, F. and Bertoldo, G. (2005). "Rarefied gas flow through a long tube of variable radius." *Journal of Vacuum Science & Technology A* 23(3): 531-533.
- Shen, C. (2006). *Rarefied gas dynamics: fundamentals, simulations and micro flows*, Springer.
- Sone, Y. (2007). *Molecular Gas Dynamics, Theory, Techniques, and Applications*. Boston, USA, Birkhauser Boston.
- Stefanov, S. (2012). "DSMC collision algorithms based on Kac stochastic model." *AIP Conference Proceedings* 1501(1): 609-614.
- Tatsios, G., Stefanov, S. K. and Valougeorgis, D. (2015). "Predicting the Knudsen paradox in long capillaries by decomposing the flow into ballistic and collision parts." *Physical Review E* 91(6): 061001.
- Tibbs, K. W., Baras, F. and Garcia, A. L. (1997). "Anomalous flow profile due to the curvature effect on slip length." *Physical Review E* 56(2): 2282-2283.
- Vargas, M., Tatsios, G., Valougeorgis, D., et al. (2014). "Rarefied gas flow in a rectangular enclosure induced by non-isothermal walls." *Physics of Fluids (1994-present)* 26(5): 057101.
- White, C., Borg, M. K., Scanlon, T. J., et al. (2013). "A DSMC investigation of gas flows in micro-channels with bends." *Computers & Fluids* 71(0): 261-271.

## Chapter 3

# Thermal transpiration flows in tapered microchannels

---

In this chapter, thermal transpiration flows in tapered microchannels are studied. Focusing on the slip flow regime, the analytical model as well as the numerical method presented in Chapter 2, based on the Navier-Stokes equations and appropriate slip boundary conditions, are used. An isothermal pressure-driven flow through a tapered channel is first studied and the numerical results are compared with existing experimental data. Then, the thermal transpiration flow in convergent and divergent channels is investigated and the observed diode effect is analyzed. With a principle based on this diode effect, a novel Knudsen pump with tapered channels is proposed and numerically tested.

### 3.1. Introduction

Fluid flowing through a channel with variable cross-section is a practical problem encountered in some microsystems such as valve-less diffuser micropumps (Olsson et al. 2000). The diffuser is a channel with gradually expanding cross-section. Once connected to two reservoirs, its design leads to lower local losses in the diffuser direction than in the nozzle direction, at least when its diverging angle is small enough (Balint et al. 2003). This means that the fluid flow has a non-symmetric behavior according to the pressure gradient direction, which can be considered as a fluidic diode effect (Stemme et al. 1993). Rarefied gas flows through gaps with non-constant cross-section also occur in some applications; it is for example the case for leakage flows in reed type valves of small reciprocating compressors (Silva et al. 2015). The features of such gaseous flows has not been studied in-depth and there are only few researches published in the literature about rarefied gas flows through tapered channels (Aubert et al. 1998, Stevanovic 2007, Veltzke et al. 2012, Graur et al. 2014, Graur et al. 2015, Szalmás et al. 2015) or in a conical pipe (Sharipov et al. 2005, Titarev et al. 2014). Similarly to the case of liquid flows, the non-symmetrical behavior of the flow in convergent/divergent channels was described for both unsteady flows (Aubert et al. 1998) and steady pressure driven flows (Veltzke et al. 2012).

Aubert et al. (Aubert et al. 1998) studied an unsteady flow through a tapered rectangular microchannel using a theoretical model derived from the Navier-Stokes equations and Maxwell slip boundary conditions (Colin et al. 1998). The behavior of microdiffusers subjected to sinusoidal pressure fluctuations including the influence of slip boundary condition was studied and the diode effect of a microdiffuser/nozzle was analyzed. Figure 3.1 shows the two layouts (a) and (b) considered in the study (Colin 2013). In layout (a), the tested element is a microdiffuser, with an increasing section from inlet to outlet. In layout (b), the same element is used as a nozzle with a decreasing section from inlet to outlet. The gains  $A_p^*$ , defined as the ratio of the outlet pressure amplitude  $A_{p_o}$  over the inlet one  $A_{p_i}$ , were different for the two layouts. In order to characterize the dissymmetry of the pressure fluctuations transmission, an efficiency  $E$  of the diode, defined as the ratio  $A_p^{*(a)} / A_p^{*(b)}$  of the pressure gains in the two layouts, was introduced. The results showed that a microdiode had a reversed diode effect compared to a millimetric or sub-millimetric diode: the value of  $E$  was less than unity below a critical frequency for a microdiode but, for a millimetric diode, it was higher than unity below a critical frequency (Aubert et al. 1998).

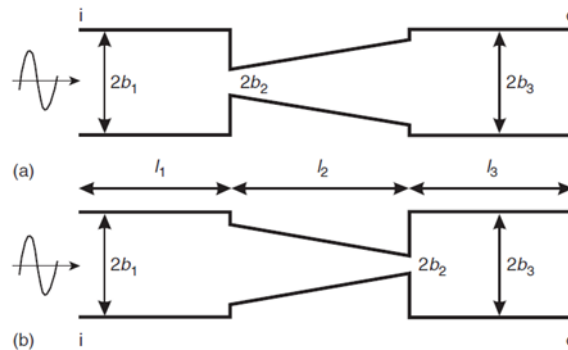


Figure 3.1: Two layouts of a microdiode placed in a microchannel (Colin 2013).

Veltzke et al. (Veltzke et al. 2012) performed an experimental study of isothermal pressure-driven gas flows through tapered microchannels etched in a silicon wafer. The channel width was varying along the channel from  $2.2 \mu\text{m}$  to  $132.0 \mu\text{m}$  over a length of  $15.0 \text{ mm}$  and the  $9.0 \mu\text{m}$  height was constant. The mass flowrate was measured and was found higher in the nozzle direction (when gas flows from the large cross-section to the narrow one). Recently, a pressure-driven flow through a Olsson et

al. 2000) long tapered channel has been studied with an analytical slip flow model and a numerical method based on the solution of the linearized S-model, as well as with experimental measurements (Graur et al. 2015). The height of the channel ranged from  $0.96\ \mu\text{m}$  to  $252.80\ \mu\text{m}$  over a length of  $11.05\ \text{mm}$ , while the channel width was constant, with a value of  $1007.50\ \mu\text{m}$ . All numerical and analytical results were in good agreement with the experimental ones for the diffuser case but experimental results were systematically overestimated by the models in the nozzle case. All the results showed that the mass flowrate was significantly higher when the tapered channel was perfused like a nozzle and the diode effect increased with the Knudsen number in the range  $[0.05; 0.25]$ . An analytical solution based on the linearized BGK kinetic equation was proposed in the whole range of rarefaction (Szalmás et al. 2015), and compared to experimental results for small Knudsen numbers. It was shown that the diode effect reached a maximum at intermediate values of the Knudsen number, i.e. near an average Knudsen number of 0.5.

To summarize, the analysis of flows in variable cross-section channels is very complex due to the conjugation of different effects which can be antagonist:

- end effects which can be preponderant when the channel length is small,
- nonlinear effects along the channel, generally dependent on the rarefaction level,
- effects linked to the geometry of the channel, in particular its angle whose variation can lead to an inversion of the diode effect.

In addition, as far as we know, there is no published data about the diode effect in tapered microchannel for non-isothermal rarefied gas flows. The main objective of the present work is then to address the three following questions:

- Can the diode effect observed for pressure-driven flows through tapered channels in the slip flow regime be correctly analyzed by the Navier-Stokes equations with adequate slip boundary conditions?
- Do thermal transpiration flows in tapered channels exhibit a diode effect?
- Is it possible to design a Knudsen pump with tapered channels?

### **3.2. Isothermal flow**

An isothermal pressure-driven flow in a tapered channel is simulated by the numerical method presented in section 2.2.3. The same channel as the one presented

in (Graur et al. 2015) is analyzed. Because of its relatively large aspect ratio along most of the channel (the width is  $W = 1000.75 \mu\text{m}$  and the height varies from  $H_1 = 0.96 \mu\text{m}$  to  $H_2 = 252.80 \mu\text{m}$ ), the tapered channel is considered in a first approximation as a 2D channel (see Fig. 3.2). The channel length  $L$  is 11.05 mm. When the pressure is higher at  $x = 0$ , the channel is referred to as a diffuser, whereas when the pressure is higher at  $x = L$ , it is called a nozzle.

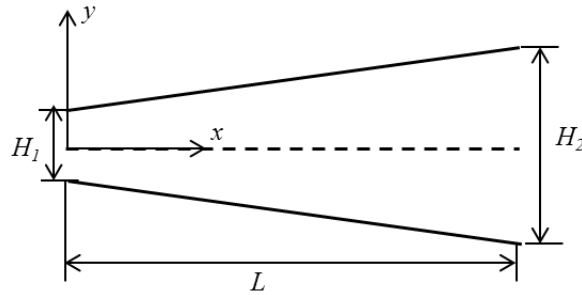


Figure 3.2: Schematic of a tapered channel

The slip boundary condition (2.15) is imposed on the walls of the tapered channel with a viscous slip coefficient  $\sigma_p = 1.018$  and the equivalent mean free path  $\lambda_e$  and the thermal transpiration term is zero due to the constant temperature  $T = 294 \text{ K}$  of the walls, which corresponds to the mean temperature in the experiments. All results are presented in function of a Knudsen number based on the hydraulic diameter and on a mean free path  $\lambda_{VHS}$  calculated from the VHS model, and argon is considered in the present simulations. The pressures ( $P_1, P_2$ ) at the ends of the channel, and the corresponding local Knudsen numbers ( $Kn_1, Kn_2$ ) values are listed in Table 3.1. The calculated mass flowrate  $\dot{m}$  and the deviations (indicated in brackets) with the results reported in (Graur et al. 2015, Szalmás et al. 2015) are also presented in Table 3.1.

It is found that the present numerical results are in good agreement with the experimental and numerical results from (Graur et al. 2015, Szalmás et al. 2015). The results are closer to the numerical results reported by (Graur et al. 2015) and higher than the experimental data. The deviations become larger when the Knudsen number increases in the diffuser layout. For the nozzle layout, the low pressure in the narrow section leads to large local Knudsen numbers; therefore only one of the experimental

cases is simulated, as shown in Table 3.1. In this tested condition, the local Knudsen number at the outlet is 0.885 and the continuum model is not accurate enough, which leads to a relative large deviation of 16.0 % from the experimental results and 4.8 % from kinetic numerical results. However, the present results provide an acceptable precision and also show that the mass flowrate is higher in the nozzle direction than in the diffuser direction.

**Table 3.1:** Mass flowrate  $\dot{m}$  ( $10^{-9}$  kg s $^{-1}$ ) of pressure-driven flows in a tapered channel

$P_1$ (kPa)	$P_2$ (kPa)	$Kn_1$	$Kn_2$	$\dot{m}$ Present	$\dot{m}$ (Graur et al, 2015)			$\dot{m}$ (Szalmás et al. 2015)
					Exp.	Anal.	Num.	Num.
<u>Diffuser</u>								
46.063	4.693	0.121	0.005	5.810	5.459 (6.4%)	5.561 (4.5%)	5.880 (1.2%)	5.459 (6.4%)
57.181	5.464	0.097	0.004	8.049	7.762 (3.7%)	7.727 (4.0%)	8.078 (0.4%)	7,762 (3.7%)
68.652	6.292	0.081	0.003	10.698	10.537 (1.5%)	10.292 (4.0%)	10.666 (0.3%)	10,537 (1.5%)
<u>Nozzle</u>								
68.618	6.295	0.0003	0.885	12.878	11.092 (16%)	12.097 (6.5%)	12.292 (4.8%)	12.121 (6.2%)

In summary, the developed numerical method can be used to correctly analyze pressure-driven flows in tapered channels. However, under the same pressure difference imposed between the ends of tapered channels, the local Knudsen number strongly varies due to the channel shape, and the present model is limited to relatively small local Knudsen numbers, corresponding to the slip flow regime.

### 3.3. Thermal transpiration flow

Configurations for studying thermal transpiration flows in tapered channels are now built as shown in Fig. 3.3, in which two reservoirs at different temperatures  $T_c$  and  $T_h$  (with  $T_h > T_c$ ), are connected by a 2-D microchannel with a constant or linearly variable cross-section. Here, we assume that the channel height  $H_0$  is much smaller than the channel width  $W$  to treat the flow as two-dimensional. When the cylindrical -or constant cross-section- channel (Fig. 3.3a) is replaced with a diffuser,

the height of the channel increases in the direction of the temperature gradient and the thermal transpiration flow is observed in the diffuser direction (see Fig. 3.3b). In the same way, we will say that the thermal transpiration flow takes place in a nozzle (see Fig. 3.3c) if the channel height decreases in the direction of the temperature gradient. For comparison between cylindrical, diffuser and nozzle configurations, the channel height at the middle of the diffuser or nozzle,  $H_0 = 10\mu\text{m}$ , is kept constant and is the same as in the cylindrical channel. The length  $L = 100\mu\text{m}$  is also kept constant in all considered cases. The maximal and minimal channel heights are noted  $H_{\text{max}}$  and  $H_{\text{min}}$ , respectively. A different ratio  $H_{\text{max}}/H_{\text{min}}$  is then obtained by simply changing the angle  $\varphi$ . In the following simulations, four groups of values for  $(H_{\text{max}}; H_{\text{min}})$  are considered:  $(10\mu\text{m}; 10\mu\text{m})$ ,  $(12\mu\text{m}; 8\mu\text{m})$ ,  $(16\mu\text{m}; 4\mu\text{m})$  and  $(18\mu\text{m}; 2\mu\text{m})$ . The ratio  $H_{\text{max}}/H_{\text{min}}$  varies from 2 to 9, which corresponds to an angle  $\varphi$  ranging from  $2^\circ$  to  $9.1^\circ$ . The temperature in the channels varies linearly along the walls:  $T(x, y) = (T_h - T_c)x/L + T_c$  with  $T_h = 573\text{K}$ ,  $T_c = 273\text{K}$ .

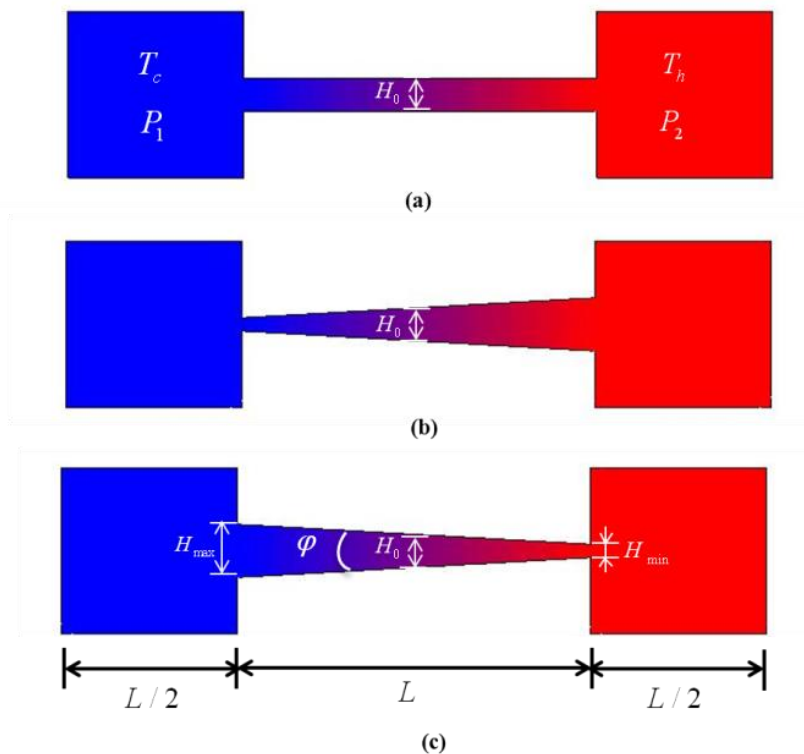


Figure 3.3: Configurations of thermal transpiration in a 2-D cylindrical channel (a) as well as in diffuser (b) and a nozzle (c)

As discussed in Chapter 2, the configurations shown in Fig. 3.3 could be operated in two ways:

(i) The pressures of two reservoirs are kept constant at the same value  $P_1 = P_2$ . A constant transpiration flow is analyzed from the cold reservoir toward the hot one and the obtained mass flowrate  $\dot{m}$  is shown in Section 3.3.1.

(ii) The whole system is closed. The gas is at the same uniform initial pressure in both reservoirs and a pressure difference is finally generated by the thermal transpiration flow. We will discuss this case in Section 3.3.2.

The analysis is made using the analytical and numerical methods respectively presented in Sections 2.2.2 and 2.2.3. The values of the viscous slip coefficient  $\sigma_p$ , the thermal slip coefficient  $\sigma_T$  and the temperature jump coefficient  $\xi_T$  used in the present simulations are, respectively, 1.018, 1.175 and 1.954, following the recommendations from Sharipov (Sharipov 2003) when Eq. (2.15) is associated to the equivalent mean free path  $\lambda_e$ .

### 3.3.1. Mass flowrate at constant pressure (open reservoir configuration)

Figure 3.4 shows the mass flowrate (per unit of width) obtained by the numerical and analytical methods for different values of the ratio  $H_{\max} / H_{\min}$ .

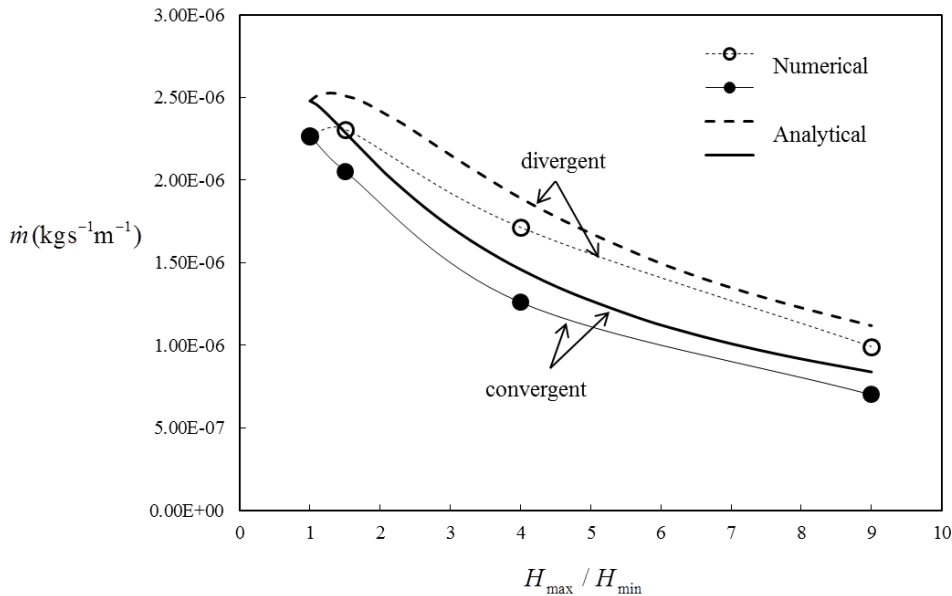


Figure 3.4: Mass flowrate generated by tapered channels with different  $H_{\max} / H_{\min}$

It is found that the mass flowrates generated by the divergent channels are larger than those generated by the convergent channels. Compared to the transpiration flow in a cylindrical channel, for which  $H_{\max} / H_{\min} = 1$ , the mass flowrate is reduced in both convergent and divergent channels, except for divergent channels with a ratio

$H_{\max} / H_{\min}$  in the range (1; 1.5) where the mass flowrate is slightly larger (<1.8% ) than the one in a straight channel.

The analytical results, based on a long channel hypothesis, overestimate the mass flowrate, which underlines the non-negligible role of the end effects. For  $H_{\max} / H_{\min} = 1.5$ , the deviations between analytical and numerical data for divergent and convergent channels are 8.7 % and 11.5 %, respectively. A longer channel with  $L / H_0 = 100$  instead of 10 is simulated to check this point. The results show that the deviations for divergent and convergent channels are reduced to less than 0.1 % and 0.3 %, respectively. Therefore, it is clear that the discrepancy between the two methods appearing in Fig. 3.4 is mainly due to the end effects which are significant for the shorter channel defined by  $L / H_0 = 10$ .

The analysis of the mass flowrate generated by thermal transpiration flow in the converging and diverging channels under constant pressure conditions shows significant differences, which is the characteristic of a diode effect. In order to characterize the different behaviors, an efficiency is defined as the ratio of the mass flowrates in the divergent and in the convergent channels:

$$E_m = \frac{\dot{m}^{div}}{\dot{m}^{conv}} \quad (3.1)$$

Figure 3.5 shows this efficiency versus the ratio  $H_{\max} / H_{\min}$ .

The values are higher than unity, which shows a larger mass flowrate in the diffuser than in the nozzle. The diffuser direction can thus be defined as the "positive" direction of the fluidic diode for thermally driven flows, which is the same behavior than for pressure driven flows. When the ratio  $H_{\max} / H_{\min}$  (or the angle  $\varphi$ ) increases, the efficiency increases and the deviations between analytical results and numerical results become larger.

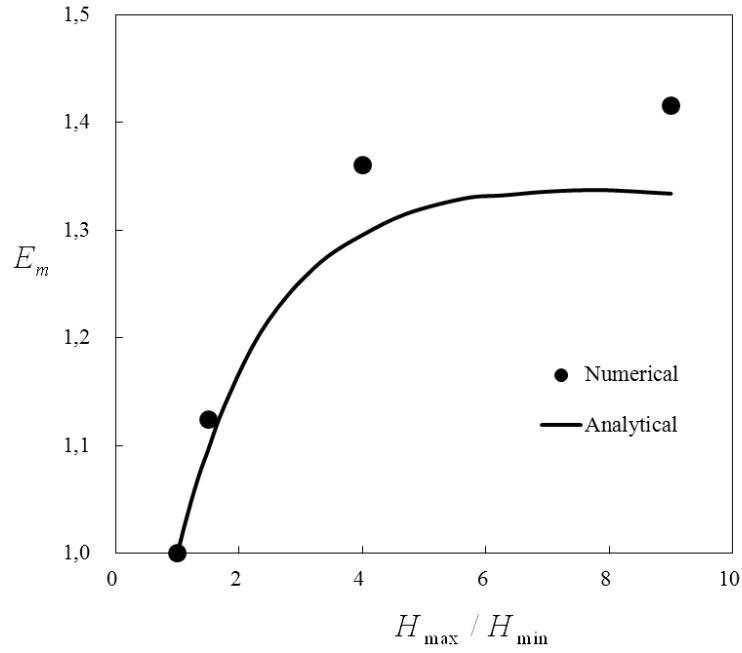


**Figure 3.5:** Efficiency based on the mass flowrate in tapered channels with different values of  $H_{\max} / H_{\min}$

### 3.3.2. Pressure difference at zero mass flowrate (closed reservoir configuration at equilibrium)

Figure 3.6 shows the pressure difference  $\Delta P$  generated between the two reservoirs versus the ratio  $H_{\max} / H_{\min}$ .

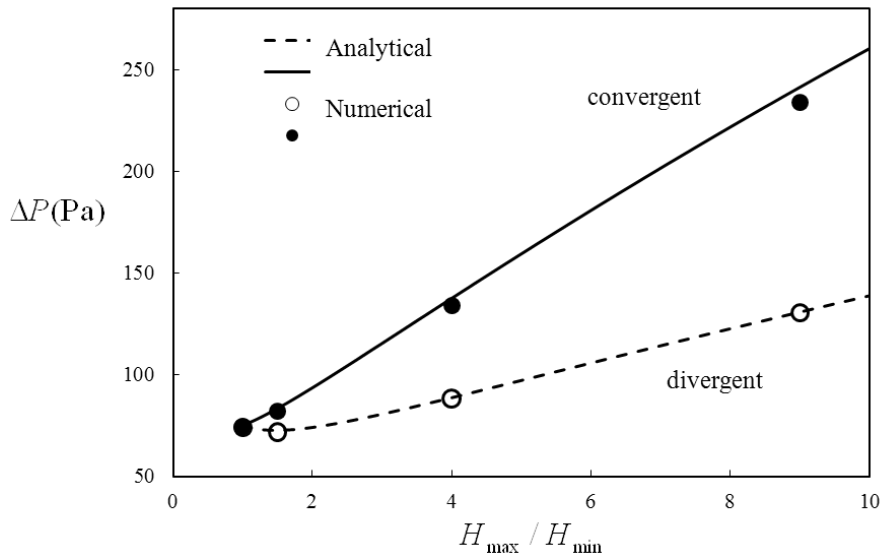


**Figure 3.6:** Efficiency of the transpiration effect in tapered microchannels: final pressure difference generated versus  $H_{\max} / H_{\min}$

For the nozzle –or convergent channel– with  $H_{\max} / H_{\min} = 1.5$ ,  $\Delta P$  is slightly lower (3 %) than that generated by the straight channel ( $H_{\max} / H_{\min} = 1$ ). In all others cases, the final pressure differences generated by the tapered channels are larger than in the cylindrical channel and the effect in the nozzle –or convergent channel– is more significant than in the diffuser. The difference between convergent and divergent channels becomes larger as the ratio  $H_{\max} / H_{\min}$  increases, and the analytical results agree well with numerical results.

In order to characterize the diode effect, another efficiency

$$E_P = \frac{\Delta P^{con}}{\Delta P^{div}} \quad (3.1)$$

is introduced, where  $\Delta P^{con}$  and  $\Delta P^{div}$  are the pressure differences generated by the convergent channel and divergent one, respectively. The variation of the efficiency with the ratio  $H_{\max} / H_{\min}$  is plotted in Fig. 3.7. It is found that the diode effect increases when the ratio  $H_{\max} / H_{\min}$  (or the angle  $\varphi$ ) increases.

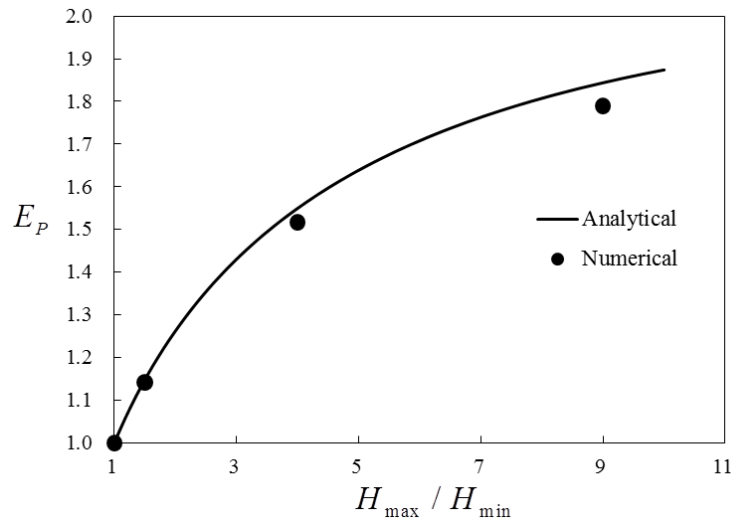


**Figure 3.7:** Efficiency on the pressure difference generated by tapered channels for different values of  $H_{\max} / H_{\min}$

Moreover, it is found that, for this flow configuration, the generated pressure difference is larger in the convergent channel than in the divergent one. The diode effect is thus in the opposite direction compared to the case in which both ends of the channel are kept at the same pressure, as shown in the previous section.

To explain this behavior, three different flow configurations are examined (Fig. 3.8). In the configuration shown on Fig. 3.8a, both ends of the channel are open and kept at the same pressure, and the flow is thermally driven. In that case, the diffuser is the positive direction of the diode (maximum flowrate for the same temperature gradient). In the second configuration (Fig. 3.8b), the flow is isothermal and pressure-driven: the positive direction is in this case the nozzle one. In the last configuration (Fig. 3.8c), end reservoirs are closed and a temperature gradient is imposed on the channel walls. A competition will then occur between the thermally driven flow generated by the temperature gradient at the walls and the pressure driven flow due to the pressure difference generated by the thermal transpiration flow. According to the analysis of the two preceding cases, larger flow rates in both directions will appear for the diffuser configuration.

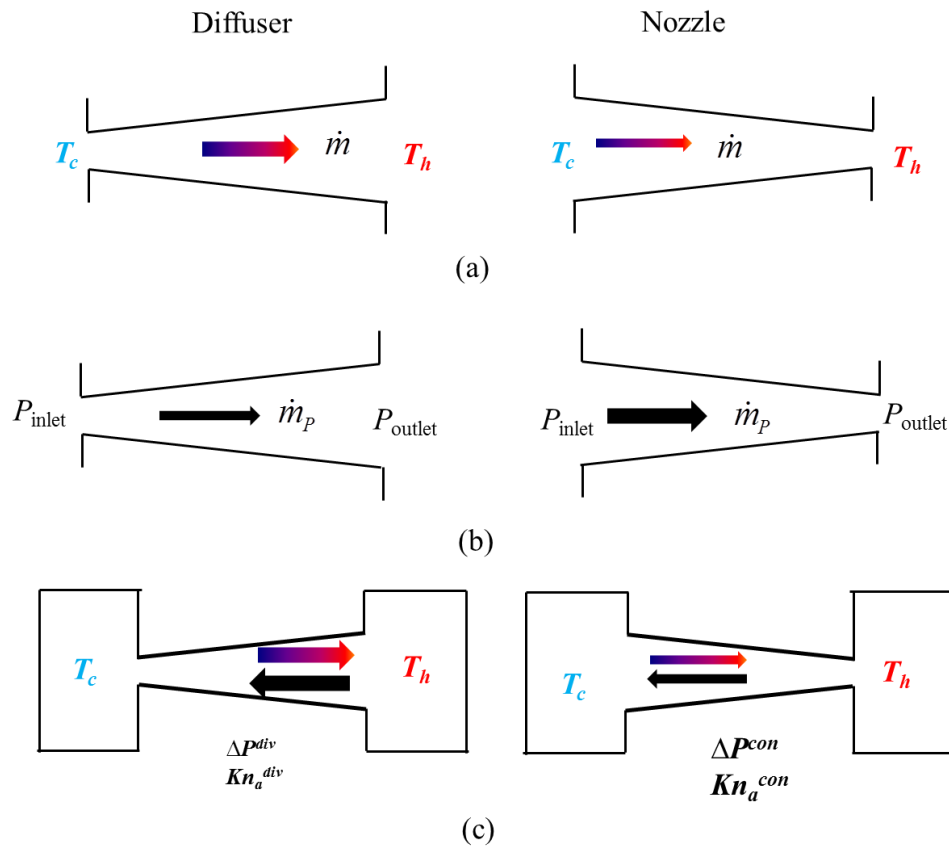


**Figure 3.8:** Illustration of the diode effect for 3 different rarefied gas flow configurations: a) Thermally driven flow in open ends channels ; b) pressure driven flow ; c) Thermally driven flow with closed reservoirs

However, at this stage, it is not possible to draw any conclusion relating to the diode efficiency  $E_p$  in terms of pressure difference, which is linked to the difference

between the pressure driven and thermally driven flowrates. On the other hand, it is also useful to analyze the influence on the flow of the average Knudsen number, which is defined as

$$Kn_a = \frac{1}{L} \int Kn_i dx \quad (3.1)$$

where  $Kn_i$  is the local Knudsen number. Figure 3.9 shows the variation of  $Kn_i$  along the channel for the case  $H_{\max} / H_{\min} = 9$ . It is found that  $Kn_i$  strongly varies in the convergent channel while it varies in a relative small range for the divergent channel. The pressure variation is relatively small in this case and  $Kn_i$  is mainly determined by the local temperature and the local channel height. The average Knudsen number is larger in the convergent case ( $Kn_a^{con} = 0.014$ ) than in the divergent one ( $Kn_a^{div} = 0.010$ ) because in the nozzle the temperature is higher where the height is small. As mentioned in Chapter 1, the existing experimental results show that the pressure difference generated by a constant cross-section channel increases with the rarefaction level in the slip flow regime. Therefore, the larger pressure difference generated by the convergent channel is probably due to the larger  $Kn_a$ .

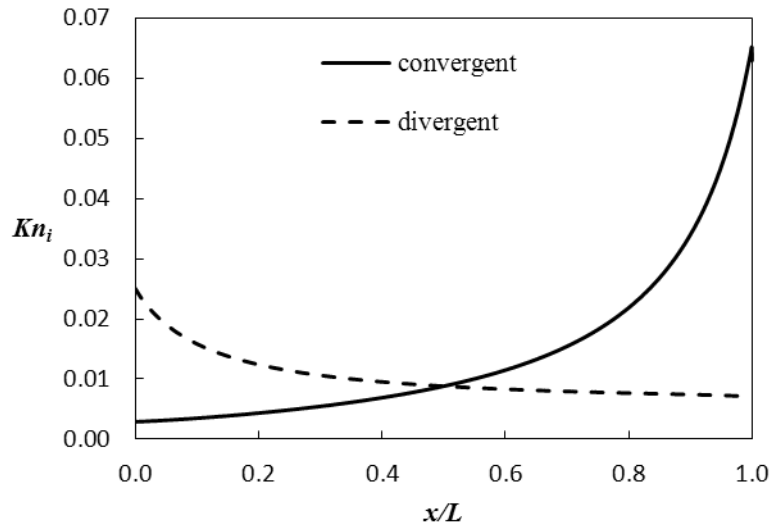


Figure 3.9: Local Knudsen number along the channel

The influence of the Knudsen number is now studied by varying the initial pressure  $P_0$  for the tapered channel for which  $H_{\max} / H_{\min} = 9$ . Table 3.2 lists the values of the initial pressure  $P_0$  and of the Knudsen number  $Kn_0$  calculated at the

mean temperature and for the characteristic length  $H_0$ , as well as the local Knudsen numbers  $Kn_1$  and  $Kn_2$  at the inlet and outlet of the convergent/divergent channels.

**Table 3.2: Pressure differences (in Pa) generated by a tapered channel with  $H_{\max} / H_{\min} = 9$  for different values of the Knudsen number.**

$P_0$ (Atm)	$Kn_0$	Divergent channel			Convergent channel			$E_p$
		$Kn_1$	$Kn_2$	$\Delta P^{div}$	$Kn_1$	$Kn_2$	$\Delta P^{con}$	
1.0	0.010	0.024	0.007	130.56	0.003	0.063	233.32	1.787
0.9	0.011	0.027	0.008	143.34	0.003	0.070	253.45	1.768
0.8	0.012	0.030	0.009	159.52	0.003	0.079	277.73	1.741
0.6	0.014	0.034	0.010	178.55	0.004	0.090	306.80	1.718
0.7	0.016	0.040	0.012	204.08	0.004	0.105	342.10	1.676
0.5	0.019	0.048	0.014	237.21	0.005	0.126	376.00	1.585

The pressure differences  $\Delta P^{div}$  and  $\Delta P^{con}$  obtained by the numerical method and the efficiency  $E_p$  are also presented in Table 3.2. It is found that  $\Delta P^{div}$  and  $\Delta P^{con}$  as well as  $\Delta P^{con} - \Delta P^{div}$  increase when the operating pressure decreases but the efficiency  $E_p$  slowly decreases. This efficiency can be linked to the ratio  $Kn_a^{con} / Kn_a^{div}$  which is higher for  $P_0 = 1\text{Atm}$  ( $Kn_a^{con} / Kn_a^{div} = 1.40$ ) than for  $P_0 = 0.5\text{Atm}$  ( $Kn_a^{con} / Kn_a^{div} = 1.33$ ). As discussed above, the generated pressure difference increases with the average Knudsen number  $Kn_a$ . Thus, when the ratio  $Kn_a^{con} / Kn_a^{div}$  increases, the efficiency  $E_p$  which is the ratio  $\Delta P^{con} / \Delta P^{div}$  also increases.

The complexity of the diode effect is due to the coupling of a temperature-driven flow and a pressure-driven flow in opposite directions. Further investigations are thus needed to better understand the physical mechanism controlling the global behavior of such devices.

### 3.3.3. Tapered-channel Knudsen pump

Based on the diode effect of a transpiration flow in tapered channels, a new Knudsen pump is proposed, as shown in Fig. 3.10a. A stage of this pump consists of a convergent channel and a divergent channel connecting reservoirs at temperatures  $T_c$

or  $T_h$ . It is reminded that the definition of convergent or divergent channels is dependent upon the direction of the temperature gradient. According to the previous results, the generated pressure difference is larger in convergent than in divergent channels, and a net gas flow is expected in the direction indicated by the arrow in Fig. 3.10a. By comparing with the classical Knudsen pump (see Fig. 3.10b), the tapered-pump can be regarded as a classical pump in which narrow channels are replaced with the convergent channels while wide channels are replaced with the divergent channels. The reservoirs in the tapered-channel pump are at constant and uniform temperature with no thermal transpiration effect inside. They are designed for connecting divergent and convergent channels and provide a certain available area for heating and cooling systems; therefore there is no strict requirement for the dimension of the reservoirs, which allows much more flexibility in terms of design constraints. In contrast, in classical Knudsen pumps, the characteristic scale of the wide channels should be much larger than that of the narrow channels to avoid a reverse thermal transpiration effect.

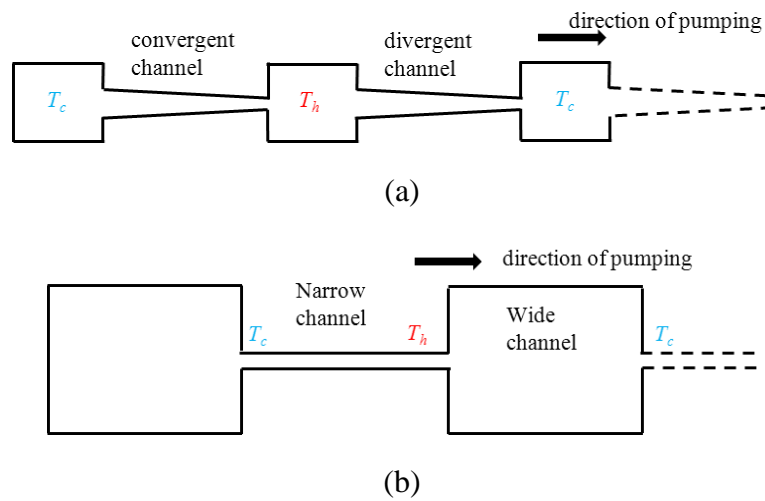


**Figure 3.10: Configuration of a Knudsen pump with tapered channels (a) compared to the configuration of classic Knudsen pump (b)**

According to the previous study, among the simulated configurations, the one with  $H_{\max} / H_{\min} = 9$  generates the largest pressure difference  $\Delta P$  and the best efficiency; this configuration is therefore chosen for a first analysis of tapered-channel pump.

One stage of pump is simulated with one close end and the other end open to the atmosphere (see Fig. 3.10a).

The pressure along the direction of pumping is shown in Fig. 3.11. It is found that the total pressure difference generated by one pump stage is  $\Delta P = 102$  Pa and those generated by the convergent and divergent channels are 232 Pa and 107 Pa, respectively. It means that the net pumping effect corresponds to a fraction of 44 % of the effect generated by the convergent channel, which is significant. The pressure gain, defined as  $G_p = \Delta P / P_0$ , is 0.10 % for a single-stage tapered-channel pump operating at atmospheric pressure. Under the same operating conditions, the pressure gain generated by the classic Knudsen pump shown in Fig. 3.10b is 0.07 %. That means that the pumping efficiency of the tapered-channel configuration is improved by 36.8 % compared to the classic one. Due to a small mean Knudsen number  $Kn_0 = 0.01$ , the value of  $G_p$  is relatively modest. The pressure gain  $G_p$  increases with the Knudsen number and it reaches 0.3 % at  $Kn_0 = 0.02$  and 1.8 % at  $Kn_0 = 0.1$ , but in this case, the validity of the model is doubtful, as the Knudsen number can be locally as large as 0.7.

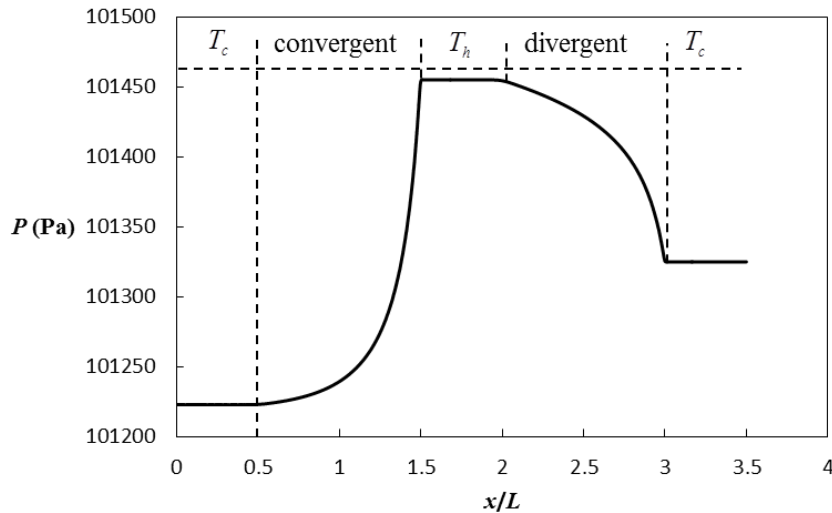


Figure 3.11: Pressure distribution along the tapered-channel pump

The pumping effect can be enhanced by using a divergent channel with a less efficient pumping effect, e.g. a divergent channel with  $H_{\max} / H_{\min} = 1.5$  or by simply

using a straight channel with  $H \geq H_0$ . The higher the contrast of pumping effects between convergent and divergent channels, the higher the pump efficiency. Following this initial analysis, the design of tapered-channel Knudsen pumps should be further optimized, taking into account manufacturing constraints. A design of numerical experiments could provide a database useful for fabricating a first optimized prototype.

### **3.4. Summary**

The analysis of thermal transpiration flows in tapered channels has shown that a diode effect exists in divergent/convergent channels submitted to a temperature gradient. Under the same conditions, the convergent channel generates a larger pressure difference than the divergent channel. The present numerical study also demonstrates the possibility of designing a tapered-channel Knudsen pump taking advantage of this diode effect. This tapered-channel Knudsen pump presents several key-advantages in terms of design and control constraints, compared with classic Knudsen pump designs.

### **References**

- Aubert, C., Colin, S. and Caen, R. (1998). Unsteady gaseous flows in tapered microchannels. First International Conference on Modeling and Simulation of Microsystems, Semiconductors, Sensors and Actuators (MSM'98). 1: 486-491.
- Balint, G., Baldas, L., Rohacs, J., et al. (2003). "Numerical study of convergent/divergent microdiodes." *Houille Blanche*(4): 43-48.
- Colin, S. (2013). Single-phase gas flow in microchannels. Heat transfer and fluid flow in minichannels and microchannels, Elsevier: 11-102.
- Colin, S., Aubert, C. and Caen, R. (1998). "Unsteady gaseous flows in rectangular microchannels: frequency response of one or two pneumatic lines connected in series." *European Journal of Mechanics - B/Fluids*. 17(1): 79-104.
- Graur, I. and Ho, M. T. (2014). "Rarefied gas flow through a long rectangular channel of variable cross section." *Vacuum* 101(0): 328-332.
- Graur, I., Veltzke, T., Méolans, J. G., et al. (2015). "The gas flow diode effect: theoretical and experimental analysis of moderately rarefied gas flows through a microchannel with varying cross section." *Microfluidics and Nanofluidics* 18(3): 391-402.
- Olsson, A., Stemme, G. and Stemme, E. (2000). "Numerical and experimental studies of flat-walled diffuser elements for valve-less micropumps." *Sensors and Actuators A: Physical* 84(1-2): 165-175.

- Sharipov, F. (2003). "Application of the Cercignani–Lampis scattering kernel to calculations of rarefied gas flows. II. Slip and jump coefficients." *European Journal of Mechanics - B/Fluids* 22(2): 133-143.
- Sharipov, F. and Bertoldo, G. (2005). "Rarefied gas flow through a long tube of variable radius." *Journal of Vacuum Science & Technology A* 23(3): 531-533.
- Silva, L. R. and Deschamps, C. J. (2015). "Modeling of gas leakage through compressor valves." *International Journal of Refrigeration* 53: 195-205.
- Stemme, E. and Stemme, G. (1993). "A valveless diffuser/nozzle-based fluid pump." *Sensors and Actuators A: Physical* 39(2): 159-167.
- Stevanovic, N. D. (2007). "A new analytical solution of microchannel gas flow." *Journal of Micromechanics and Microengineering* 17(8): 1695.
- Szalmás, L., Veltzke, T. and Thöming, J. (2015). "Analysis of the diodic effect of flows of rarefied gases in tapered rectangular channels." *Vacuum* 120, Part A: 147-154.
- Titarev, V. A., Shakhov, E. M. and Utyuzhnikov, S. V. (2014). "Rarefied gas flow through a diverging conical pipe into vacuum." *Vacuum* 101: 10-17.
- Veltzke, T., Baune, M. and Thöming, J. (2012). "The contribution of diffusion to gas microflow: An experimental study." *Physics of Fluids* 24(8): 082004.



# Chapter 4

## Curved-channel Knudsen Pump

In this chapter, a Knudsen pump consisting of a series of curved segments and straight segments is studied, using the numerical method described in Chapter 2. Thanks to the low computational cost of this numerical method, the pumping effect of a multi-stage curved-channel pump is investigated and a parametric analysis of a one-stage pump is performed in a wide range of geometrical parameters and operating conditions. A first prototype of a multistage curved-channel Knudsen pump at millimetric scale, which was designed and fabricated at the Karlsruhe Institute of Technology, is presented and its performances are estimated through a series of numerical simulations.

### 4.1. Introduction

The basic design of a Knudsen pump consists of a thin channel, in which the gas is rarefied, connecting a cold region and a hot region. In order to increase the efficiency of the pump, it is possible to use a cascade system consisting of several units connected in series by intermediate thick channels or reservoirs (Fig. 4.1a).

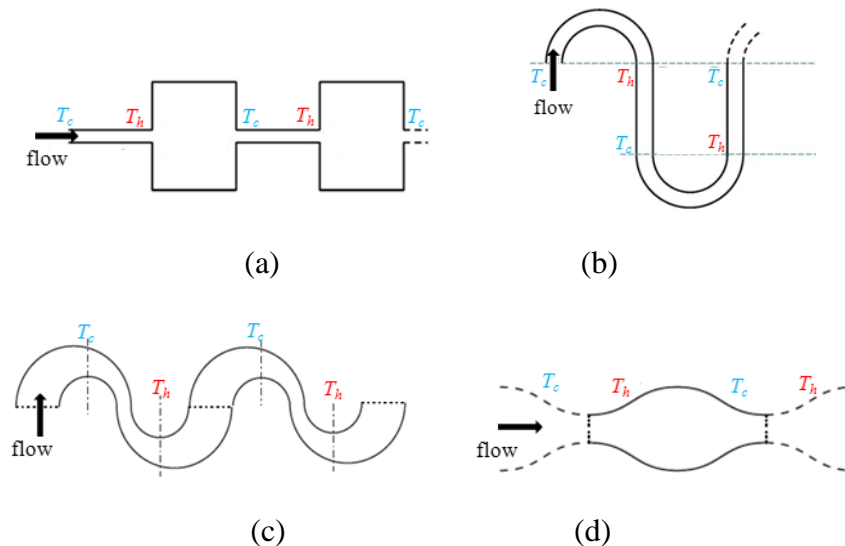


**Figure 4.1:** Configurations of classic Knudsen pump (a), curved-channel Knudsen pump (Aoki et al. 2009) (b), double-curved Knudsen pump (Bond et al. 2014) (c) and sinusoidal Knudsen pump (Bond et al. 2016) (d).

Thermal transpiration takes place in the narrow channels from the cold sections at a low temperature  $T_c$  towards the hot sections at a high temperature  $T_h$ , while the phenomenon does not occur in the reservoirs where the flow is not rarefied due to their larger dimensions. Therefore, in order to operate a Knudsen pump at atmospheric pressure, the dimensions of the narrow channel must be in sub-micro or nano-scales while the dimensions of the reservoirs must be large enough, i.e. in a millimetric scale, to avoid reversed thermal transpiration flows. Consequently, it is difficult to fabricate such a pump.

Recently, an alternative configuration has been proposed and numerically studied (Aoki et al. 2008, Aoki et al. 2009), in which the sequence of narrow-wide segments was replaced with a sequence of curved-straight segments. The curved (semicircular) segments have the same width as the straight segments (Fig. 4.1b). In this layout, a uniform temperature gradient is applied along the walls of the straight channels (the temperature decreases linearly from  $T_h$  to  $T_c$ ), while an opposite temperature gradient is applied along the walls of the curved part. As a consequence, two opposed thermal transpiration flows are generated in two successive straight and curved channels. Due to the different geometry, however, the transpiration effect is stronger in the curved segments and a global net flow is finally observed. A resulting steady flow is observed if the pump is open at both ends with the same pressure. If one end is closed, an unsteady flow takes place until a pressure difference is obtained between the closed and the open ends. In addition, it has been shown that a multi-stage Knudsen compressor consisting of curved and straight channels can actually operate in the slip flow and transition regimes (Aoki et al. 2008, Aoki et al. 2009). More precisely, there is an optimum Knudsen number, depending both on the curvature of the bent channels and on the number of stages, for achieving the highest compression efficiency. Under specific conditions, it is possible to reach a maximum compression ratio either in the slip flow or in the early transition regimes. However, in these works, the pump dimensions were in a metric scale, the operation was at low pressure and all the geometrical parameters were chosen for facilitating the computations rather than considering the technical constraints related to the design and fabrication of a prototype. The configuration proposed by Aoki et al. has later been modified by Bond et. al by increasing the imbalance between straight and curved segments in order to improve the pumping effects (Bond et al. 2014). The straight sections of the pump

shown in Fig. 4.1b have been removed and the curved sections altered to introduce width variation along the flow path, as shown in Fig. 4.1c. By an appropriate comparative study, it was shown that the maximal mass flowrate generated by the double-curved geometry was two and a half times higher than the flowrate of the curved-channel configuration. And, very recently, the mass flowrate has been further improved for a sinusoidal pump (Bond et al. 2016) as shown in Fig. 4.2d. However, in practice, it is hard to fabricate such a channel and provide a precise temperature control.

The goal of the present work is to using the previously developed simulation tool in which the appropriate slip boundary conditions, taking into account the thermal transpiration flow due to the tangential temperature gradient and the effect of the wall curvature, are implemented in a commercial CFD code. As shown in Chapter 2, this method has a very good agreement with kinetic simulations (Aoki et al. 2008, Aoki et al. 2009) for the thermal transpiration flow in ringed shaped channels. Moreover, it has a largely reduced computational cost compared with kinetic simulations or DSMC. Though this method is limited to the slip flow regime, its high computational efficiency and adaptation for any geometry are very important for the stage of design and optimization of the pump structure. In Section 4.2, a series of numerical simulations are taken out for clarifying the performance of a multi-stage pump and making a parametric analysis of a single stage in order to draw a guideline for designing a prototype. Section 4.3 presents a first prototype of a multi-stage Knudsen pump with curved segments at millimetric scale that has been designed and fabricated at the Karlsruhe Institute of Technology in 2012. The performances of the pump are evaluated thanks to numerical simulations.

## 4.2. Numerical design

### 4.2.1. Simulation of multi-stage pumps

In this section, a multi-stage micropump having the configuration shown in Fig. 4.2 is simulated. The basic unit of the pump consists of a semicircle with radius  $R_c = 100\mu\text{m}$  and a straight channel of length  $L_s = 314\mu\text{m}$ . Both segments have the same width  $D_s = 100\mu\text{m}$ . The hot and cold temperatures are  $T_h = 900\text{K}$  and  $T_c = 300\text{K}$ , respectively, and the pressure at the open end D of the device is  $P_0 = 1500\text{Pa}$ . The pump has a closed section A at the temperature  $T_c$ . The Knudsen

number calculated at the low temperature section is  $Kn_c = 0.036$ . The mesh of each unit contains  $200 \times 100$  cells. The simulations are made for different numbers of stages  $N_s = \{1; 2; 4; 8; 25\}$ .

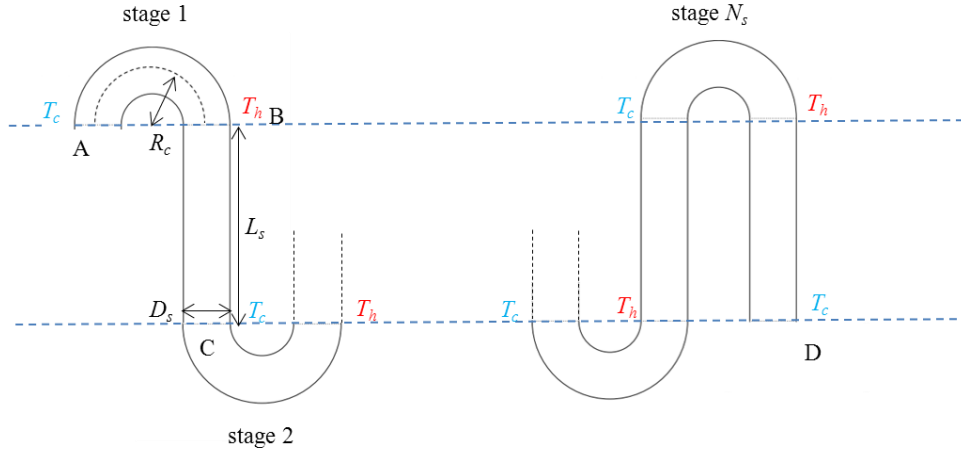
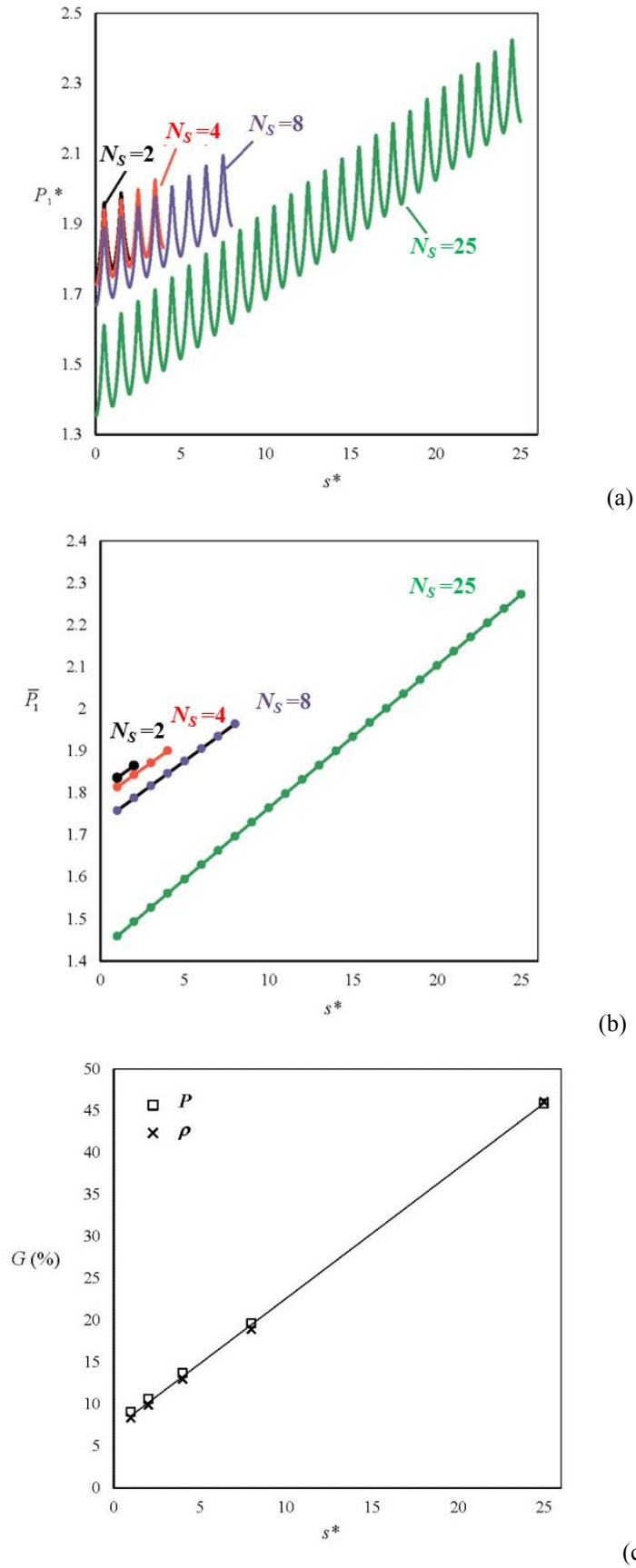


Figure 4.2: Configuration of multi-stage curved-channel pump

The average density along the centerline of the whole serpentine channel is noted  $\bar{\rho}$ . The dimensionless pressure  $P_1^* = P/(\bar{\rho}RT_c)$  along this centerline for the different cascade systems is shown in Fig. 4.3a as a function of the dimensionless curvilinear abscissa  $s^* = s/(2L_s)$ . As expected, the pressure profiles oscillate with a mean pressure variation depending on the number of stages. The dimensionless average pressure  $\bar{P}_1$  defined as the mean value of  $P_1^*$  in each stage is a linear function of  $s^*$  which depends on the number of stages (Fig. 4.3b). The pressure gain  $G_p$ , defined as the ratio of the pressure difference between the two ends of the cascade system to the outlet pressure  $P_0$ , and the density gain  $G_\rho$ , defined as the ratio of the density difference between the two ends of the cascade system to the density at the open end, are plotted in Fig. 4.3c. Both pressure and density gains are linearly dependent on the number of stages. Additional simulations with a larger number of stages and under different conditions, however, are required in order to confirm this observation. For the present simulated device, the pressure and density gains are 46 % for the 25-stage device. Extrapolating the line of Fig. 4.3c, it is found that a gain of 100 % could be achieved with about 60 stages.



**Figure 4.3:** Dimensionless pressure  $P_1^*$  (a), dimensionless average pressure  $\bar{P}_1$  (b) and pressure and density gains  $G$  (c) along the centerline of the serpentine channel.

Aoki et al. (Aoki et al. 2009) have simulated a different multi-stage Knudsen pump ( $D_s = 1\text{m}$ ,  $L_s = 6.28\text{m}$ ,  $R_c = 2\text{m}$ ,  $T_h = 900\text{K}$ ,  $T_c = 300\text{K}$ ,  $N_s = 2$  to 16). The Knudsen number calculated at the low temperature section is  $Kn_c = 0.20$  and the average Knudsen number defined by the author as  $Kn_0 = \mu_{ref} \sqrt{2RT_c} / D_s \rho_0 RT_{ref}$ , with  $T_{ref} = 273.15\text{K}$ , is 0.5. In their system, a gain of 100 % is achieved with about 32-36 stages. The results of Fig. 4.3 present the same trend and the qualitative observations are almost identical. The difference in the required number of stages for achieving 100 % of gain is most likely due to the different Knudsen number which is higher in the case simulated by Aoki et al. The operation of the Knudsen pump in this early transition regime is expected to be a bit more efficient.

#### 4.2.2. Parametric analysis of a single-stage micropump

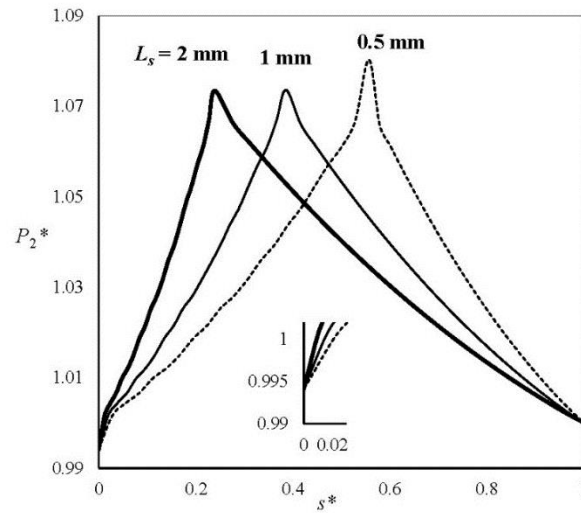
##### Influence of the geometrical parameters

The micropump unit can be described by three geometrical parameters: the length  $L_s$  of the straight part, the width  $D_s$  of the microchannel and the radius  $R_c$  of the curved part centerline. Alternatively, two dimensionless geometrical parameters can be defined: the ratios  $D_s/R_c$  and  $L_c/L_t$  where  $L_c$  the length of the centerline of the curved part and  $L_t = L_s + L_c$  is the total length of the centerline. Table 4.1 provides the values of the geometrical parameters for the 6 simulated configurations. These parameters were chosen in order to respect micro fabrication constraints.

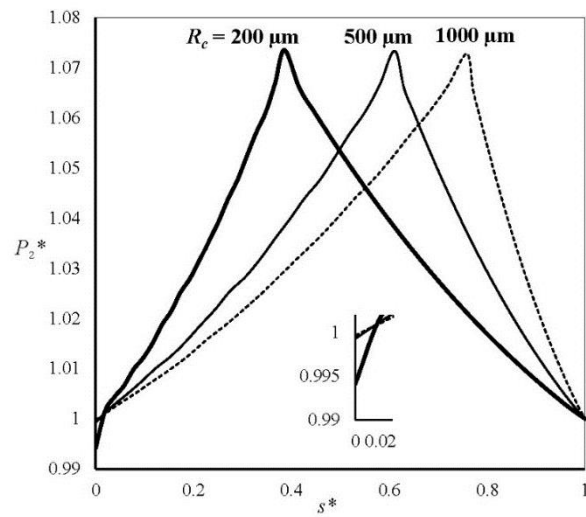
**Table 4.1: Simulation parameters and pressure gain for a single-stage curved-channel Knudsen micropump.**

Case	1	2	3	4	5	6
$L_s$ ( $\mu\text{m}$ )	1000	1000	1000	1000	500	2000
$D_s$ ( $\mu\text{m}$ )	50	200	50	50	50	50
$R_c$ ( $\mu\text{m}$ )	500	500	1000	200	200	200
$D_s/R_c$	0.1	0.4	0.05	0.25	0.25	0.25
$L_c/L_t$	0.611	0.611	0.759	0.386	0.557	0.239
$G_P$ (%)	0.09	1.60	0.04	0.60	0.60	0.60

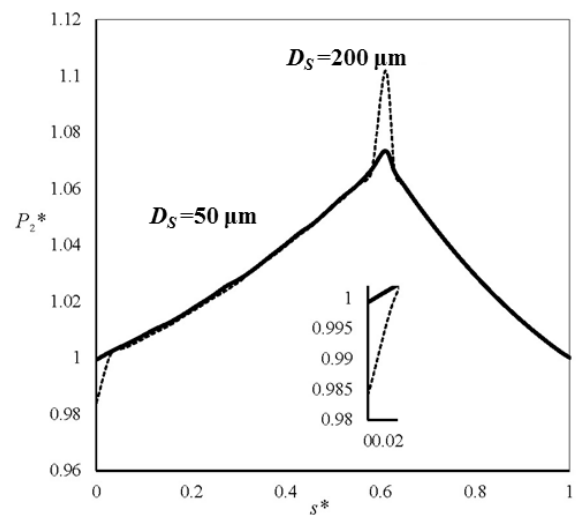
In the first set of comparisons, the operating conditions are kept constant and only the influence of the geometrical parameters is tested. This single unit has a closed end A with a wall kept at temperature  $T_c = 300$  K and an open end C kept at the same temperature  $T_c$  and at pressure  $P_c$  such that  $Kn_c = 0.095$ . The walls of section B are at the temperature  $T_h = 450$  K. The pressure gains  $G_p = (P_c - P_A) / P_c$  for all cases are listed in the last line of Table 4.1. The distributions of the dimensionless pressure  $P_2^* = P / P_c$  along the microchannel are presented in Fig. 4.4, underlying the influence of the straight channel length  $L_s$  (a), of the radius  $R_c$  of the curved part centerline (b) and of the microchannel width  $D_s$  (c). The pressure distributions near the closed end A are magnified in the inset figures to highlight the pressure differences between both ends obtained for the different values of the tested parameters. A higher pressure difference between the two ends corresponds to a higher efficiency of the micropump. Fig. 4.4a which compares cases 4, 5 and 6 demonstrates that the length  $L_s$  of the straight part has no influence on the pressure difference as the gains obtained for the three cases are 0.60 %. The influence of the curved channel radius is illustrated in Fig. 4.4b comparing cases 1, 3 and 4, and the influence of the microchannel width is illustrated in Fig. 4.4c comparing cases 1 and 2. Figs. 4.4b and 4.4c show that decreasing the radius of the curved part and/or increasing the width of the channel lead to an increase of the pressure difference. The gains calculated for a radius of 200  $\mu\text{m}$ , 500  $\mu\text{m}$  and 1000  $\mu\text{m}$  are 0.60 %, 0.09 % and 0.04 %, respectively. A larger gain is achieved for a smaller  $R_c$ . In Fig. 4.4c,  $P_c = 1160$  Pa when  $D_s = 50$   $\mu\text{m}$  and  $P_c = 290$  Pa when  $D_s = 200$   $\mu\text{m}$  in order to achieve the same Knudsen number. The gain dramatically increases from 0.09 % to 1.6 % when the channel width is increased by a factor of 4.



(a)



(b)



(c)

**Figure 4.4:** Influence of the microchannel dimensions on the dimensionless pressure  $P_2^*$  distributions along the centerline for a single-stage pump in cases 4, 5 and 6 (a), cases 1, 3 and 4 (b) and cases 1 and 2 (c).

Influence of the operating conditions

The influence of the operating conditions (pressure and temperature) is now examined for case 4. The Knudsen number  $Kn_C$  at the open end, the temperature difference  $\Delta T$  and the obtained pressure gain  $G_p$  are given in Table 4.2.

**Table 4.2:** Pressure gain  $G_p$  for the different operating conditions of case 4

Case	4-a	4-b	4-c	4-d	4-e
$Kn_C$	0.047	0.095	0.095	0.095	0.19
$\Delta T$ (K)	150	150	250	600	150
$G_p$ (%)	0.15	0.60	1.04	2.79	2.34

By modifying the pressure level at the open end of the channel, the corresponding Knudsen number can be changed. Three different  $Kn_C$  are tested (0.05, 0.01 and 0.2) and the distributions of the dimensionless pressure  $P_2^* = P/P_C$  along the microchannel centerline are shown in Fig. 4.5a. The effect of the temperature difference on the pressure distribution is presented in Fig. 4.5b. Temperature differences of 150 K, 250 K and 600 K are imposed by changing the high temperature on the walls of section B. The maximum value of the pressure is experienced in section B between the curved and the straight parts of the microchannel, where the temperature has its highest value  $T_h$ . This section corresponds to  $s^* = 0.386$  in case 4. In the straight parts of the microchannel, the pressure is decreasing along the centerline in a slightly nonlinear manner with a higher gradient close to the hot section. In the curved part of the microchannel, a similar behavior is observed, with in addition an inflexion point in the curve  $P_2^*(s^*)$  for  $s^* \approx 0.03$ . A pressure lower than the outlet pressure imposed at  $s^* = 1$  is only observed very close to the closed end, for  $s^* < 0.01$  (see inset figures). Both the Knudsen number and the temperature difference have a strong effect on the efficiency of the pump, as expected. Larger  $Kn$  and/or  $\Delta T$  result in a higher pressure difference between the two ends of the microchannel, as illustrated by the inset figures. This effect can be described quantitatively by the pressure gain  $G_p$  values given in Table 4.2. It is found that an increase of the Knudsen number, which depends on the operating pressure for the same channel width, has a significant impact on the pressure gain: multiplying  $Kn_C$  by a factor roughly amounts to multiplying  $G_p$  by the square of this factor, in a

Knudsen range  $Kn_C \in [0.05; 0.19]$  relating to the slip flow regime. Note that the Knudsen numbers based on the average temperature are a bit different from  $Kn_C$ : they are 0.127, 0.150 and 0.249, for cases 4-b, 4-c and 4-d, respectively. As expected, the temperature gradient has also a strong impact on the pressure gain.

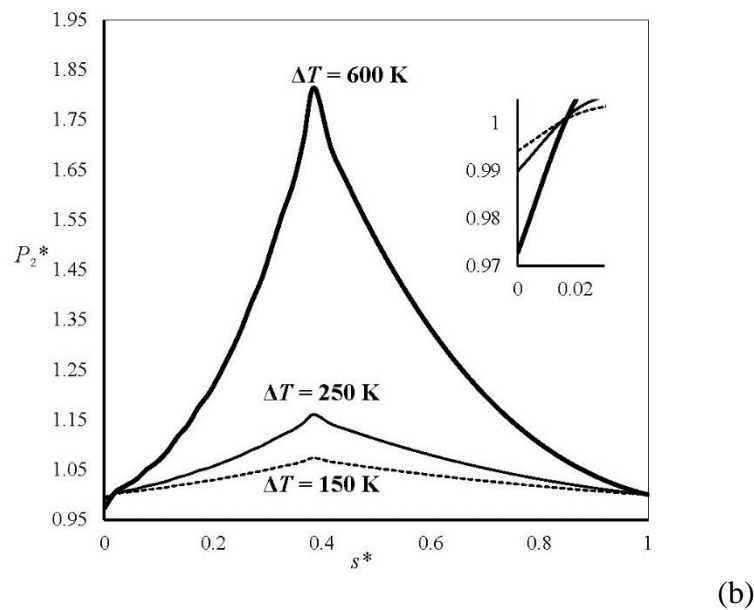
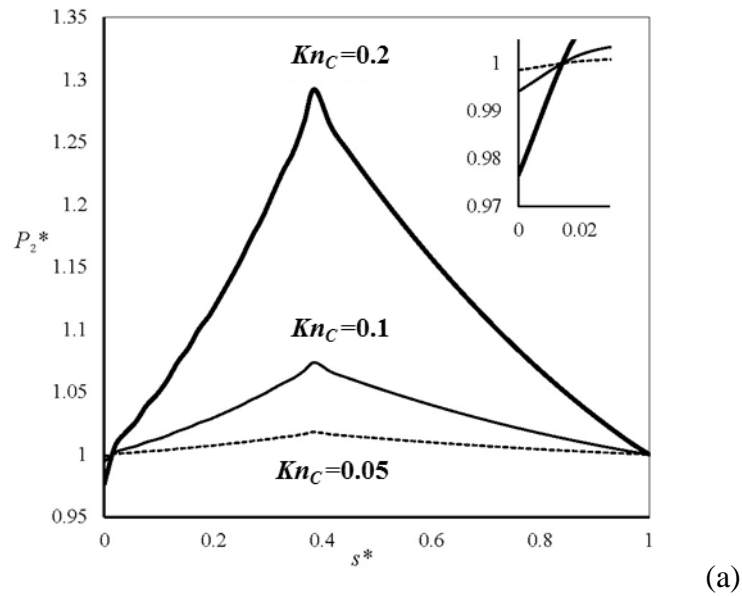


**Figure 4.5: Influence of the Knudsen number  $Kn_C$  and of the temperature difference  $\Delta T = T_h - T_c$  on the dimensionless pressure  $P_2^*$  along the microchannel centerline of a single-stage micropump.**  
 a) Cases 4-a, 4-b and 4-e; b) Cases 4-b, 4-c and 4-d.

For a given value of  $P_c$ , the pressure gain  $G_p$  versus the temperature difference can precisely be fitted by a second order polynomial; for example, for  $Kn_c = 0.095$ , the equation is  $G_p = 1.42 \times 10^{-6} (\Delta T)^2 + 3.80 \times 10^{-3} \Delta T$ .

From the above analysis, it is found that significant gains, of the order of 1 or 2 %, can be achieved for a single stage configuration with reasonable values of the geometrical and operating parameters. In order to improve the efficiency of the micropump, the dimensionless ratio  $D_s / R_c$  should be as large as authorized by the technological constraints. In addition, the temperature difference  $T_h - T_c$  should be as high as possible. A larger Knudsen number which depends on the channel width and on the operating pressure can lead to a better performance of the pump. On the other hand, modifying the length of the straight channel, or modifying the ratio  $L_c / L_s$ , has a negligible effect on the gain.

However, the distribution of temperature imposed on the wall in the previous analysis is idealized. In practice, a heated or cooled point source can hardly be achieved. The influence of the size of the heated or cooled zone is studied by setting 3 different heated or cooled lengths  $L_z$  in the boundary conditions:  $L_z = 0$  (point source),  $L_z = 0.1 L_s$  and  $L_z = 0.2 L_s$ . The temperatures  $T_h$  or  $T_c$  are kept constant in the heated or cooled zones and linear distributions are imposed along the straight or curved walls in the other zones. Figure 4.6 shows the temperature imposed on the inner wall and the distribution on the outer wall is similar. The case 4-d (see Table 4.2) is used as a test case. The pressure gains of 0.43 and 0.36 obtained for  $L_z = 0.1 L_s$  and  $L_z = 0.2 L_s$ , respectively, are much lower than the gain of 2.72 calculated for an ideal temperature distribution. The influence on the distribution of the dimensionless pressure  $P_2^*$  along the microchannel centerline is shown in Fig. 4.7. The peak observed in section B for  $L_z = 0$  is replaced with a constant pressure zone whose length corresponds to the one of the heated zone. A constant pressure which is lower than the outlet pressure is observed in the cooled zone close to the closed end (see inset figure).

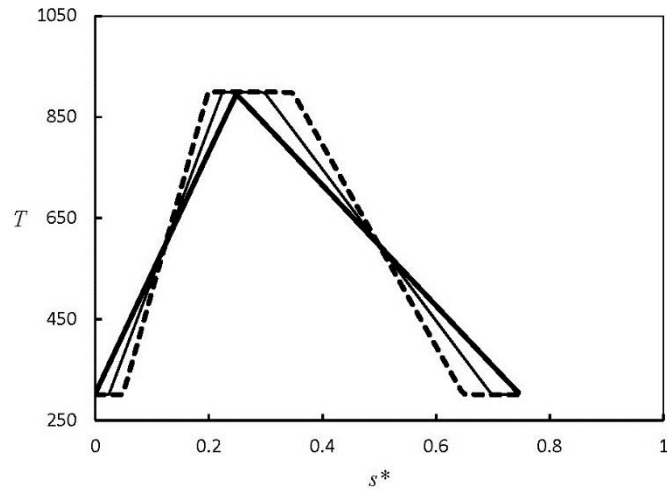


**Figure 4.6:** Imposed temperature distribution along the inner wall of the curved and straight parts of the channel for different sizes of the heated or cooled zones:  $L_z = 0$  (thick solid line),  $L_z = 0.1 L_s$  (thin solid line) and  $L_z = 0.2 L_s$  (dashed line).

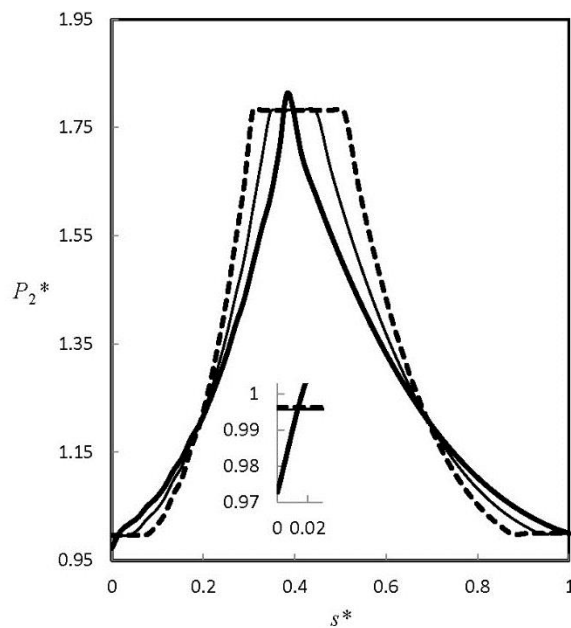


**Figure 4.7:** Influence of the size of the heated or cooled zones on the dimensionless pressure  $P_2^*$  along the microchannel centerline of a single-stage micropump:  $L_z = 0$  (thick solid line),  $L_z = 0.1 L_s$  (thin solid line) and  $L_z = 0.2 L_s$  (dashed line).

The influence of the size of the heated and cooled zones on the mass flowrate and flow pattern is now discussed for one unit of the multi-stage micropump studied in section 4.2.1 ( $D_s = 100 \mu\text{m}$ ,  $L_s = 314 \mu\text{m}$ ,  $R_c = 100 \mu\text{m}$ ,  $T_h = 900 \text{ K}$ ,  $T_c = 300 \text{ K}$ ) when

both ends are open and at the same pressure. The pressure at both ends is  $P_0 = 1500$  Pa and the Knudsen number calculated for these conditions is  $Kn_c = 0.036$ .

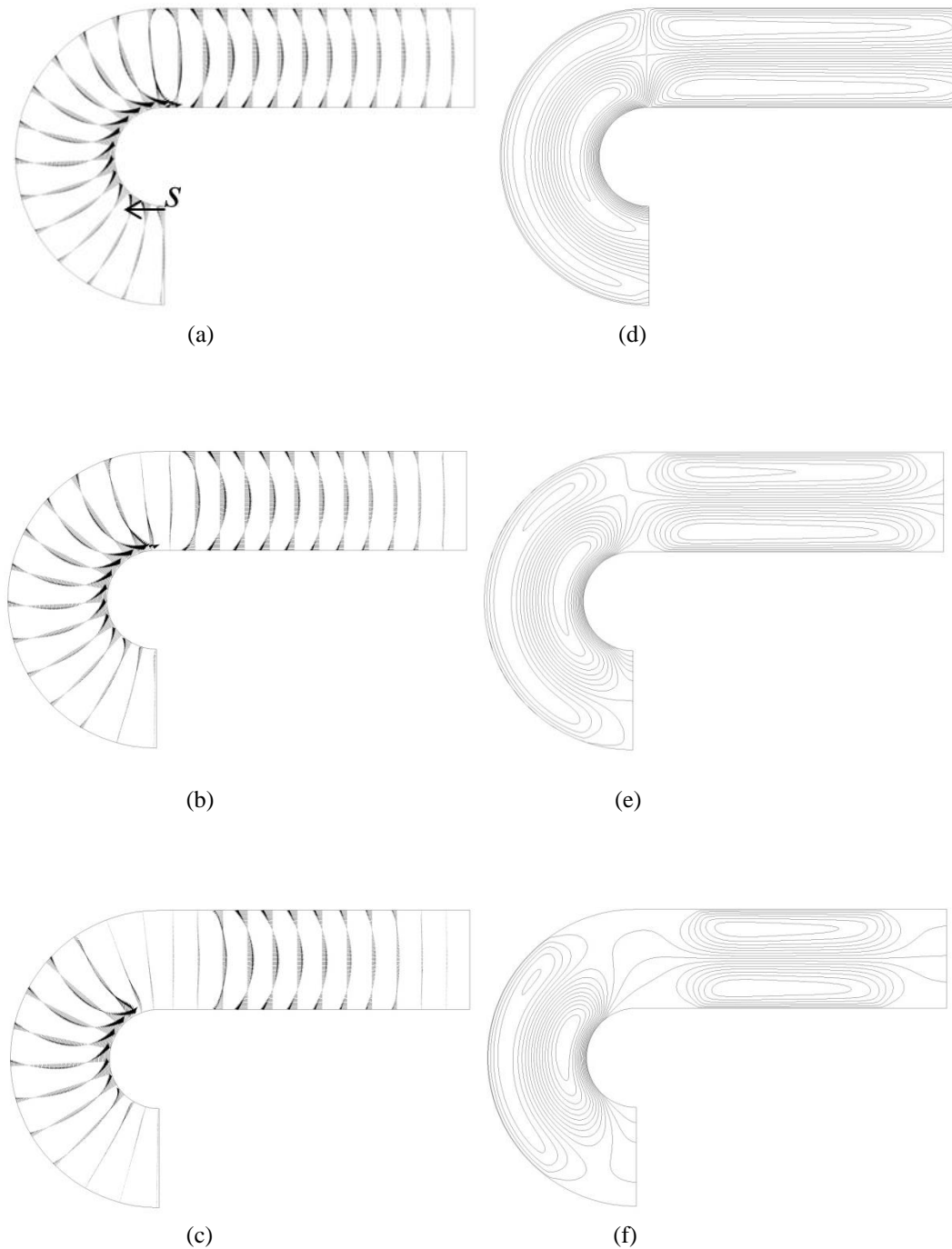


**Figure 4.8: Velocity fields (a) to (c) and streamlines (d) to (f) for three sizes of the heated and cooled zones:**

$L_z = 0$  (a) and (d),  $L_z = 0.1 L_s$  (b) and (e),  $L_z = 0.2 L_s$  (c) and (f).

For  $L_z = 0$ ,  $L_z = 0.1 L_s$  and  $L_z = 0.2 L_s$ , the mass flowrates are  $7.79 \times 10^{-7}$  kg/s,  $7.78 \times 10^{-7}$  kg/s and  $7.57 \times 10^{-7}$  kg/s respectively. These results show that increasing the size of the heated and cooled zones leads to a slight decrease of the generated mass flowrate. This effect is limited when the size of these zones remains small (the mass flowrate reduction is of the order of 0.1 % for  $L_z = 0.1 L_s$  compared to  $L_z = 0$ ) but becomes significant for larger heated and cooled zones (the reduction is of 2.8 % for  $L_z = 0.2 L_s$  compared to  $L_z = 0$ ).

The velocity vectors in a series of cross sections of the channel (Figs. 4.8a-c) and the streamlines (Figs. 4.8d-f) are shown. It is observed that the velocity is much lower in the heated and cooled zones when these zones are enlarged while the thermal transpiration flows near the straight walls (in the negative direction) and curved walls (in the positive direction) are both largely enhanced due to larger local temperature gradients. As the thermal transpiration flow generated along the curved walls is always stronger than the one generated along the straight part of the channel, a mass flowrate is finally obtained in the positive  $s$  direction. However, the difference between the flows generated in the positive and negative directions decreases when the heated and cooled zones are enlarged, which explains the diminution of the global mass flowrate.

It is interesting to see in Figs. 4.8d to 4.8f that the thermal transpiration flow generated at the inner curved wall of the curved channel is deviated towards the center of the straight channel by the recirculation zones generated along the straight walls. The size and shape of these recirculation zones as well as those generated in the curved part of the channel are strongly modified by the enlargement of the heated and cooled zones. For further study of flow details, the path lines of the fluid particles released from section A are shown in Fig. 4.9. It is observed that the fluid particles which creep toward section B along the inner and outer walls of the curved part are redistributed. Most of the fluid particles return along the center of the curved channel due to the resistance of the counter transpiration flow generated at the straight walls and the positive pressure gradient along the curved centerline. A small fraction of the flow (see path line 1), however, exits at section C, close to the center of the section. This redistribution of the path lines could be of some interest for mixing purposes. On the other hand, a significant fraction of the gas molecules is not advected through the pump and can only exit the recirculation zones by a diffusion process.

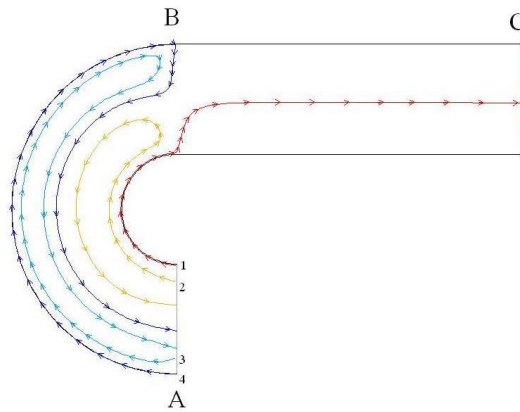


**Figure 4.9:** Path lines of the fluid particles released from section A (for  $L_z = 0$  ).

### 4.3. A prototype of serpentine Knudsen pump

#### 4.3.1. Description of the pump system

A first prototype of multi-stage Knudsen pump with curved segments at millimetric scale has been designed and fabricated, taking into account manufacturing limitations, at the Karlsruhe Institute of Technology (Germany) in 2012. Figure 4.10a shows the sketch of the pump system and Fig. 4.10b is a photo of the final completed prototype. The system consists of four main blocks: the upper and bottom covers made in aluminum, the block in which the micro-channel has been etched and its upper wall block that are both made in PEEK (Polyetherether Ketone). Those blocks are assembled with the help of 14 stainless steel screws and a ring is put between the two blocks in PEEK to ensure the sealing. Two microfluidic connectors for the inlet and outlet of the gas are included in the micro-channel upper wall block. Figure 4.10c shows the configuration of the micro-channel which consists of a sequence of straight and semi-circular parts. The micro-channel has a rectangular cross-section of  $100 \mu\text{m} \times 50 \mu\text{m}$ . The length of the straight part is 2 mm and the distance between the centerlines of two successive straight channels is 1.5 mm. The channel includes 50 semi-circular segments and is thus considered as a 50-stage Knudsen pump. The main reason for choosing PEEK was its low thermal conductivity (around  $0.25 \text{ W/m K}$  at room conditions), which should allow to control a temperature gradient along the channel walls. The heating layer was placed between the upper cover and the micro-channel upper wall block while the cooling layer was placed between the micro-

channel block and the bottom cover which includes fittings for the inlet and outlet of the cooling fluid. The cooling is operated using a low temperature fluid which flows in a series of grooves and the heating is achieved by a resistance wire. The cooling or heating layer contacts with a copper plates on which a series of pins were arranged in accordance with the cooling/heating points of the micro-channel. Those pins are in contact with PEEK blocks and heat transfer between the cooling/heating blocks and the microchannel is made through them.

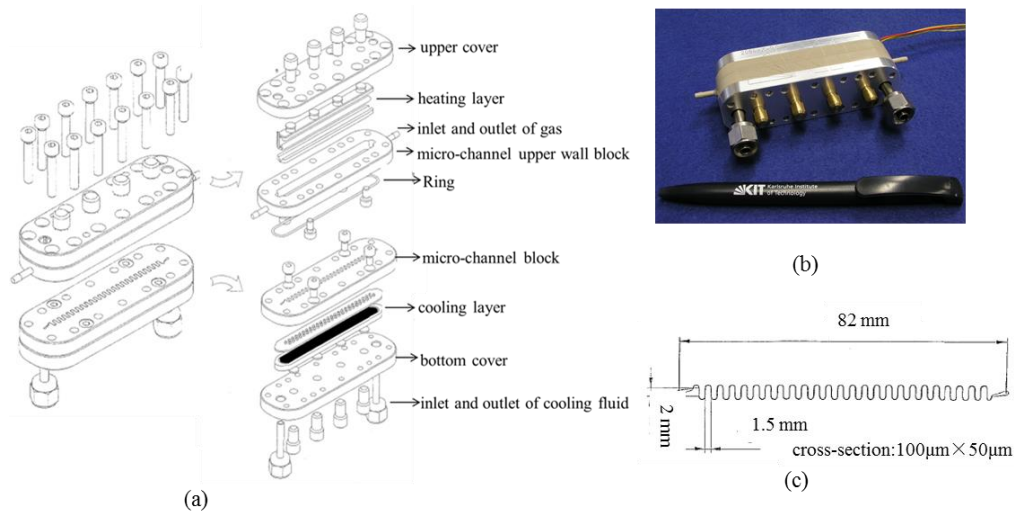


**Figure 4.10:** Serpentine Knudsen system fabricated by KIT. (a) sketch of the pump system; (b) photo of the final device; (c) configuration of the micro-channel

### 4.3.2. Numerical estimation of performance

The design and fabrication of the prototype started in 2010 and finally finished in 2012. The micro-channel configuration has not been optimized by the numerical study but it has been designed taking into account manufacturing limitations. Now, the performance of the pump is numerically examined by a series of 2-D simulations. The geometry of a single stage is shown in Fig. 4.11.

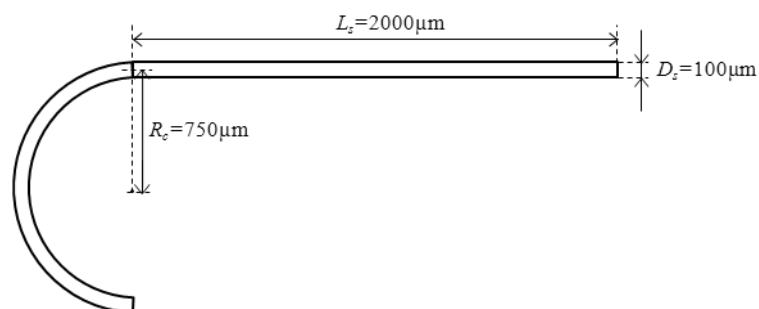


**Figure 4.11:** Geometry of single stage of prototype

A feasible and favorable operating condition in the laboratory is considered. The pins of the cooling plate may be cooled by liquid nitrogen to 77 K and the hot pins could be heated to 370 K. The tips of pins which are in contact with the walls of the microchannel have a very small area of  $20\ \mu\text{m} \times 20\ \mu\text{m}$  compared to the dimensions of microchannel:  $L_z = 0.01L_s$ . The influence of the size of the heated or cooled zone can thus be considered negligible. Linear temperature distributions are assumed along the straight and curved channels. Argon is considered as working gas and the operating pressure  $P_0$  is 150 Pa, resulting in a Knudsen number calculated at the low temperature section  $Kn_c = 0.062$ . These temperature and pressure conditions are first used to study the effect of multi-stages and then the influence of operating pressure and working gas species are investigated by a two-stages configuration.

#### Effect of multi-stages

The simulations are run for different numbers of stages  $N_s = \{1; 2; 4; 8; 20; 50\}$ . Figure 4.12 shows the pressure gain versus the number of stages. The pressure gain linearly increases with the number of stages, which is similar to Fig. 4.3c for the design studied in Section 4.2.1, but the gain of the present pump is much lower. The pressure gain of a single stage is only 0.24 %, which corresponds to a pressure difference of 0.36 Pa generated at the operating pressure of 150 Pa. The total pressure difference generated by 50 stages is about 14.4 Pa and the total pressure gain is 9.6 %.

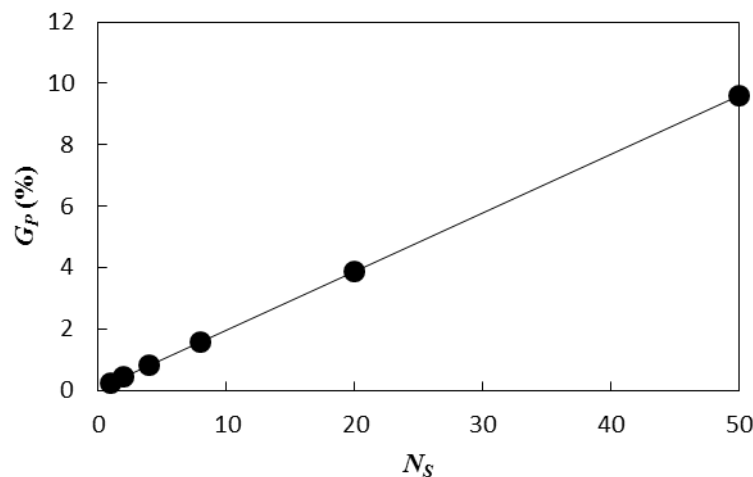


**Figure 4.12:** Pressure gain versus number of stages ( $T_c = 77\ \text{K}, T_h = 370\ \text{K}, P_0 = 150\ \text{Pa}$ )

)

Reviewing the results obtained in the analysis of the geometrical parameters (see Table 4.1), a larger pressure gain is achieved when the dimensionless ratio  $D_s/R_c$  is increased. The dimensionless ratio  $D_s/R_c$  of this prototype is 0.13, which results in a relatively low pressure gain. The dimensions of the channels in the present prototype are limited by the overall design and the fabrication constraints, especially on the heating/cooling system. Although the tips of the pins used for local heating and cooling have a small area, the diameter of the pins base is about 1.7 mm, limiting the possibility to reduce the distance between successive hot or cold points.

As shown as Fig. 4.12, the relationship between the pressure gains and the stages number is linear and the pressure gain of a 50-stage pump is about 21.6 times larger than the one of a 2-stage pump. Therefore in the following study, only a 2-stage pump is simulated and the pressure gain of the whole pump is obtained by multiplying the results by a factor of 21.6.

#### Influence of the operating pressure

Due to the 100  $\mu\text{m}$  characteristic length of the channel, the pump must be operated at low pressure to reach rarefied conditions. The influence of the operating pressure is studied in the range of 150 to 1000 Pa, which corresponds to a cold point Knudsen number  $Kn_c$  between 0.062 to 0.009. Figure 4.13 shows that the generated pressure difference increases with  $Kn_c$  from 0.1 to 0.6 Pa, corresponding to a pressure gain ranging from 0.012 % to 0.445 %. By multiplying these values by a factor of 21.6 as mentioned before, the total pressure gain  $G_p$  of the present pump could range from 0.26 % to 9.62 %, which corresponds to a generated pressure difference  $\Delta P$  ranging from 2.61 to 14.4 Pa for an operating pressure  $P_0$  between 1000 and 150 Pa. It can thus be noted that with the accuracy of the pressure gauge in the laboratory (0.2% of reading) it will be very difficult to accurately measure the generated pressure difference for an operating pressure higher than 1000 Pa. On the other hand, due to the limitations of the continuum approach, the curve in Fig. 4.13 is not completed for large Knudsen numbers. The generated pressure difference should continually increase with  $Kn_c$  and reach a maximum somewhere in the transition regime. But a high  $Kn_c$  requires a very low pressure (e.g.  $P_0 = 18.6$  Pa is needed for reaching  $Kn_c = 0.46$ ), which requests more stringent experimental conditions.

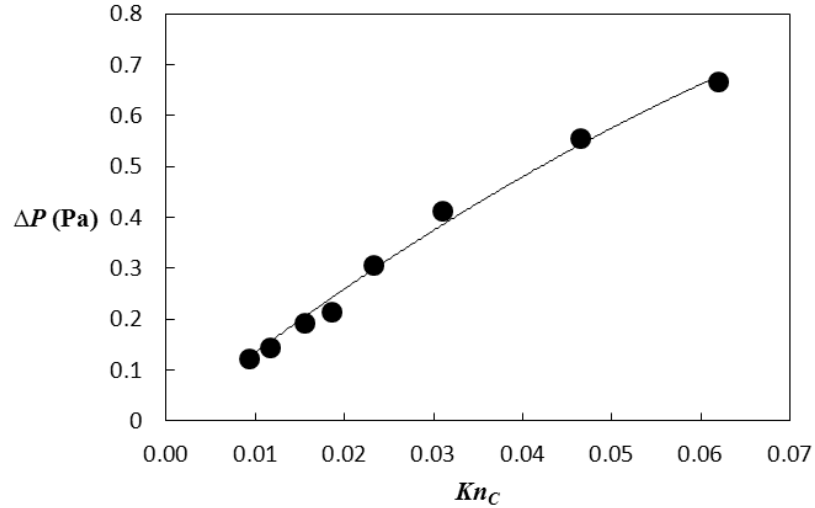


**Figure 4.13:** Pressure difference versus  $Kn_C$  for the 2-stage pump  
( $T_c = 77$  K,  $T_h = 370$  K,  $P_0 = 150$  Pa ~ 1000 Pa ).

Influence of the gas species

A series of simulations are run with helium, which leads to larger Knudsen numbers than with argon for the same operating pressures. Figure 4.14 shows the generated pressure difference versus operating pressure and Fig. 4.15 shows the pressure gain versus Knudsen number. It is found that at the same operating pressure the generated pressure differences for helium are about 7.6 times larger than for argon. However, the evolutions of the pressure gain with  $Kn_C$  have the same trend for both gases and can be fitted with an exponential function  $G_p = 77.46 Kn_C^{1.876}$ .

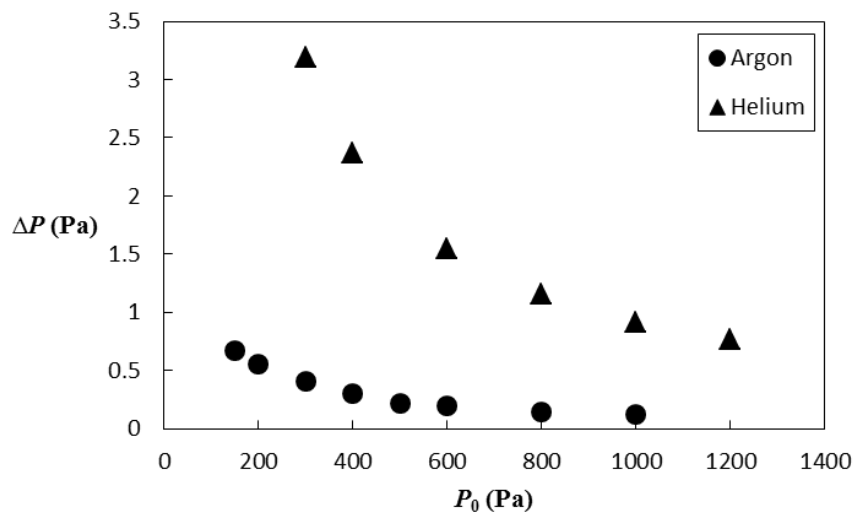


**Figure 4.14:** Pressure difference versus operating pressure for a 2-stage pump  
( $T_c = 77$  K,  $T_h = 370$  K).

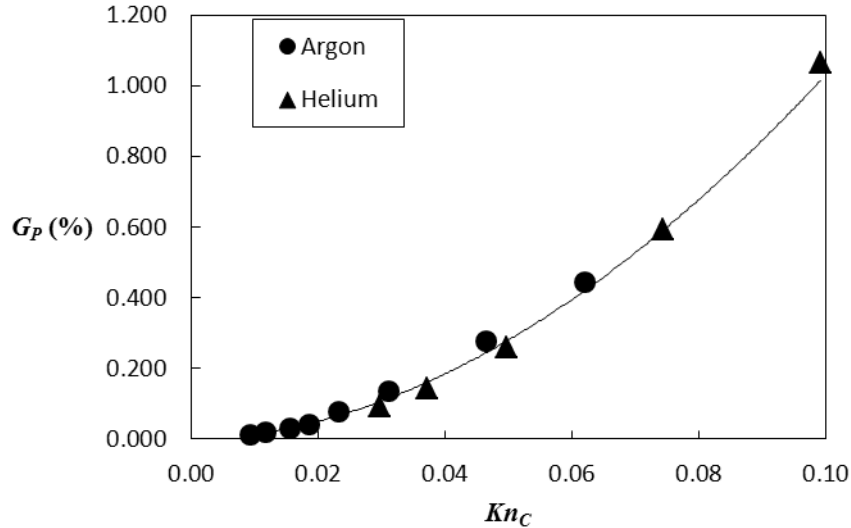


**Figure 4.15:** Pressure gain versus  $Kn_C$  for argon et helium for the 2-stage pump ( $T_c = 77$  K,  $T_h = 370$  K,  $P_0 = 150$  Pa ~ 1200 Pa ).

It is important to note that all these simulations have been performed using the 2D numerical model presented in Chapter 2. The results can thus just provide rough estimations of the pump performances, as the small depth ( $50 \mu\text{m}$ ) of the microchannel should lead to a significant decrease of the pumping efficiency. Besides, the actual temperature distribution within the two blocks of PEEK should be much more complex than the assumed linear distribution along the straight and curved parts of the microchannel.

As mentioned before, testing this pump requires stringent experimental conditions, but the experimental set-up that has been built (Jeerasak et al. 2010) in our group has a non-negligible leakage for low pressure. An improved experimental set-up that will be presented in Chapter 6 has been built and in a future work, the pump will be experimentally tested using this new experimental set-up. Besides, as shown in Fig. 4.10, the pump uses special connectors at the inlet and outlet. For connecting the pump to the experimental set-up, we failed to make a totally leakage-free connection and the internal part of the pump itself is not totally airtight. Some additional improvements are required before any possible reliable test of this serpentine pump prototype.

#### 4.4. Summary

It has been proved in Chapter 2 that the developed numerical model, based on a continuum approach with a specific treatment of the appropriate boundary conditions implemented as user defined functions in a commercial CFD code, was efficient to analyze thermal transpiration in curved-channel pumps. Compared to kinetic simulations or DSMC, this model has a largely reduced computational cost, facilitating the design and optimization of the pump, from a geometrical and operating conditions point of view. The present numerical simulations have shown that multi-stage Knudsen pumps based on curved channels can be efficient in the slip flow regime. Moreover, a parametric analysis of a single-stage Knudsen pump has permitted to draw guidelines for improving the device efficiency: the pump should have a semicircular part with large curvature and should operate under high temperature difference and under rather strong rarefied conditions. A first prototype of a multistage Knudsen pump with curved segments at millimetric scale has been designed and fabricated at the Karlsruhe Institute of Technology and its performances have been estimated using a simplified 2D configuration. Due to the manufacturing technological constraints, the curved-channel has a thin shape, i.e. the ratio of the channel width to the radius of the curved parts is small. The numerical results showed that the pressure gain generated by a 50-stage pump increases with the cold point Knudsen number to reach nearly 10 % for  $Kn_c = 0.062$ . The prototype will be experimentally examined in a future work with a new experimental set-up, but an optimization of its structure and fittings will be preliminary necessary.

#### References

- Aoki, K., Degond, P. and Mieussens, L. (2009). "Numerical simulations of rarefied gases in curved channels: thermal creep, circulating flow, and pumping effect." *Communications in Computational Physics* 6(5): 911-954.
- Aoki, K., Degond, P., Mieussens, L., et al. (2008). "A Diffusion Model for Rarefied Flows in Curved Channels." *Multiscale Modeling & Simulation* 6(4): 1281-1316.
- Bond, D. M., Wheatley, V. and Goldsworthy, M. (2014). "Numerical investigation of curved channel Knudsen pump performance." *International Journal of Heat and Mass Transfer* 76: 1-15.
- Bond, D. M., Wheatley, V. and Goldsworthy, M. (2016). "Numerical investigation into the performance of alternative Knudsen pump designs." *International Journal of Heat and Mass Transfer* 93: 1038-1058.

Jeerasak, P., Stelios, V., Dimitris, V., et al. (2010). "A novel experimental setup for gas microflows." 8(1): 16.

# Chapter 5

## Ratchet Knudsen pumps

---

This chapter presents a numerical analysis of a novel Knudsen pump configuration. The pumping element consists of two facing isothermal ratchet surfaces at different temperatures, which is consequently much easier to thermally control than a classic Knudsen pump with a temperature gradient along the walls. The asymmetric saw-tooth-like surfaces in optimal geometrical conditions can create temperature inequalities in the near wall region and finally engender a macroscopic flow. The origin of ratchet Knudsen pumps and the preliminary investigations found in the literature are introduced first. Then, several configurations are investigated using the Navier-Stokes equations with appropriate slip and temperature jump boundary conditions. The influence of the geometrical parameters, operating pressure and temperature conditions, is analyzed. In section 5.3, the performance of this type of pumps in a large range of Knudsen numbers is studied by DSMC simulations. A parametric study reveals the effects of several crucial parameters including the Knudsen number, the temperature difference, the accommodation coefficients as well as the main geometrical parameters. An analysis of the simulation results based on the decomposition of the solution into ballistic and collision parts is proposed and used to identify the main physical phenomena driving the flow.

### 5.1. Introduction

A new possible Knudsen pump configuration consisting of two facing isothermal surfaces with different temperatures, one of which at least being unsymmetrically nanostructured, has recently been proposed by Donkov et al. (Donkov et al. 2011) and by Würger (Würger 2011). Donkov et al. considered a two-dimensional prototype channel composed of a cold flat wall facing a hot structured wall (Fig. 5.1a). The cold flat wall parallel to the  $x$ -direction had a diffusive surface and the hot ratchet-structured wall exhibited a periodic pattern generated by three segments: two diffusive boundary segments in the  $x$ - and  $y$ -directions linked by one tilted specular segment. Donkov et al. demonstrated that a net flowrate  $\dot{m}$  is thermally generated in

the opposite  $x$ -direction when the gas is rarefied, with a maximum momentum flux in the free-molecular flow regime and a maximum mass flux in the transition flow regime. From an analytical analysis in the free molecular regime, it was demonstrated that there is no momentum in the  $x$ -direction when the entire structured wall has a diffusive surface and that, in this regime, the asymmetry of the wall topography is not a sufficient condition to generate a flow along the channel. This analysis was confirmed and completed by a numerical simulation based on two Monte Carlo schemes: a time-splitting Monte Carlo method with a hard sphere collision model and a standard DSMC method with a variable hard sphere collision model. It was shown that a maximum flowrate is achieved for a Knudsen number of the order of  $10^{-1}$  and that the maximum value of the velocity is observed around the tips of the ratchet surface.

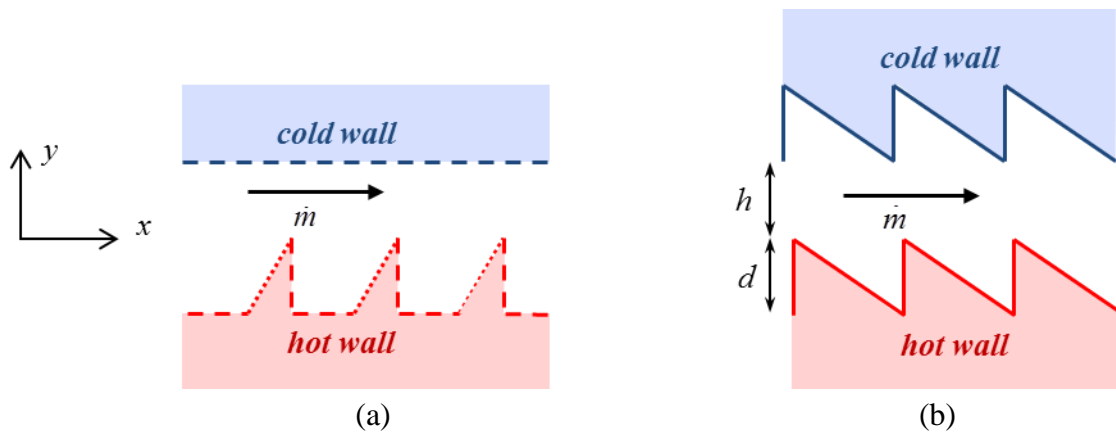


**Figure 5.1:** Two ratchet designs analyzed by (a) Donkov et al. (Donkov et al. 2011) and (b) Würger (Würger 2011). In (a), diffusive walls are represented by dashed lines and specular walls by dotted lines.

In the paper of Würger, the initial idea is inspired from the so-called Leidenfrost ratchet effect, by which a surface carved as a ratchet and heated over the Leidenfrost temperature can propel an evaporating droplet in a preferential direction (Linke et al. 2006, Ok et al. 2011). In his paper, Würger pointed out that the thermal transpiration flow due to a strong temperature gradient in the cleft between the droplet and the Leidenfrost ratchet surface is the physical mechanism which generates the droplet movement towards the preferential direction (Würger 2011). He proposed an analytical model of the vapor flow in the cleft between the droplet (or a piece of dry ice) and the heated ratchet surface which is able to qualitatively predict the velocity of

the droplet observed in experiments (Linke et al. 2006, Ok et al. 2011). In contrast to that analysis, Hardt et al. (Hardt et al. 2013) recently concluded from a numerical analysis using a Monte Carlo scheme that the thermal transpiration flow has an insignificant contribution to the thrust of Leidenfrost solids on ratchet surfaces, and that this thrust is dominated by a pressure-driven flow resulting from the sublimation of the solid. In the absence of any sublimation effect, however, Würger (Würger 2011) proposed a Knudsen pump design based on the same physical mechanism as the one described in (Donkov et al. 2011). It consists of two facing ratchet surfaces with the same topography maintained at a respectively hot and cold uniform temperatures (Fig. 5.1b). From a simplified analytical model only valid for small ratchet depths (i.e. for  $d < h$ ), it was demonstrated that velocities of several meters per second could be generated and that the phenomenon should also be observed for a high distance between both plates, up to hundred times higher than the mean-free path of the molecules. In Würger's analysis, there was no assumption on the accommodation of the gas at the walls, contrary to the hypothesis of Donkov et al. In addition, the thermal transpiration along the vertical wall segments was neglected in Würger's model, which could partly explain the significant differences with the conclusions of Hardt et al. In the above mentioned papers (Donkov et al. 2011, Würger 2011, Hardt et al. 2013), the ratchets have acute angles and the strong temperature gradients close to these angles play a significant role in the pumping efficiency.

From these analyses, several questions are raised about the possibilities of constructing a Knudsen pump with ratchet surfaces:

- 1) Is there a pumping effect when all surfaces are diffusive and not only when the accommodation coefficient has different values according to the segments of the ratchet? What is the influence of accommodation coefficients on different segments?
- 2) Is there a significant generated flowrate, even when the angles of the ratchet have a finite curvature, as expected in a real-case?
- 3) What is the influence of the main geometric parameters (ratchet angle, misalignment of the ratchet patterns on the facing walls, gap between the walls) and operating parameters (Knudsen number and temperature difference)?

These problems are investigated both by a continuum approach performed on ANSYS Fluent® CFD software and by DSMC simulations. Finally, guidelines are drawn for designing a prototype.

## 5.2. Study in the slip flow regime

### 5.2.1. Problem statement

Three basic designs are considered, as illustrated in Fig. 5.2. The first configuration has a cold flat wall facing a ratchet hot wall, the second and third ones have two hot and cold ratchet walls with aligned (Config. 2) or misaligned (Config. 3) identical saw-tooth patterns. The gap  $h$  between the ratchet and flat walls or between two ratchet walls is defined from the planes of the ratchet tips. The ratchet surfaces have a periodic pattern with a length  $L$  in the  $x$ -direction and height  $d$  in the  $y$ -direction, resulting in an angle  $\beta$ . In the case of misaligned patterns (Config. 3), there is a shift of  $L/2$  in the  $x$ -direction between the two facing walls. In addition, whatever the configuration (1, 2 or 3), a finite curvature, with a radius  $r$ , is assumed at the intersection of the ratchet segments in order to take into account realistic microfabrication constraints.

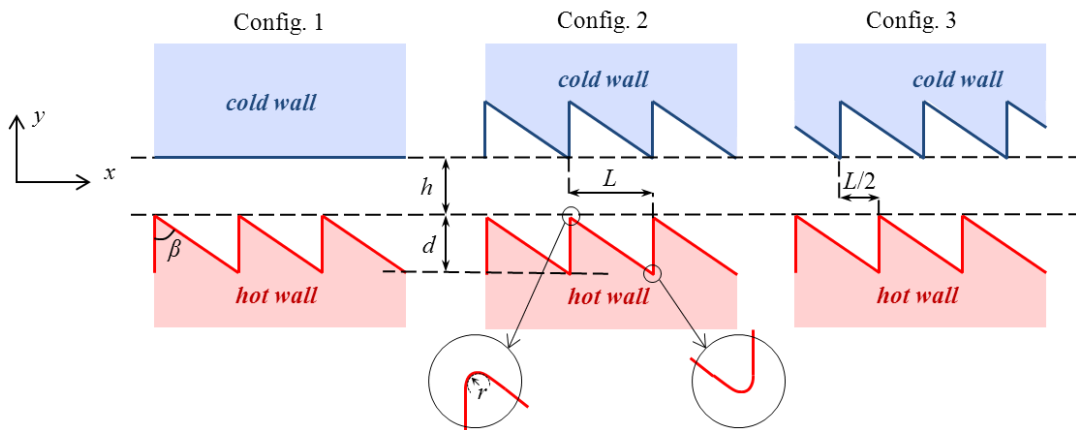


Figure 5.2: Three analyzed configurations and geometric parameters

Each surface is assumed isothermal, which can be achieved with a material of very high thermal conductivity. The hot temperature of the lower wall is noted  $T_h$  and the cold temperature of the upper wall is noted  $T_c$ . As a consequence, the main temperature gradient is perpendicular to the surfaces, in contrast with classical

transpiration flows generated by an imposed tangential temperature gradient along the walls; but, as demonstrated below and due to the structuration of the surface, it results in temperature gradients tangentially to the ratchet surfaces and leads to a rectified thermal transpiration flow in the  $x$ -direction.

The numerical model presented in Section 2.2.3 is used and the slip and temperature jump boundary conditions Eqs. (2.15) and (2.16) are implemented by User Defined Functions, in which the values of the viscous slip coefficient  $\sigma_p$ , the thermal slip coefficient  $\sigma_T$  and the temperature jump coefficient  $\xi_T$  used in the present simulations are, respectively, 1.018, 1.175 and 1.954, following the recommendations from Sharipov (Sharipov 2003) and the equivalent mean free path  $\lambda_e = \mu\sqrt{2RT}/P$  is used.

The Knudsen number

$$Kn = k_2 \frac{\mu_0 \sqrt{RT_0}}{h P} \quad (5.1)$$

is defined as the ratio of the mean free path  $\lambda$  based on the Variable Hard Sphere (VHS) model over the height  $h$ . In Eq. (5.1),  $k_2$  is a coefficient depending on the molecular collision model; in the present study, the VHS model leads to  $k_2 = 0.967$  for argon. The dynamic viscosity  $\mu_0$  is defined at the mean temperature  $T_0 = (T_c + T_h)/2$ .

### 5.2.2. Influence of the mesh on the calculations accuracy

In this problem, the accuracy of the calculations of slip velocity and temperature jump is strongly influenced by the type and resolution of the mesh near the walls, due to the huge normal temperature gradient which is much larger than the tangential one. In particular, a systematic error on the tangential temperature gradient occurs, due to the fact that this gradient can only be calculated by ANSYS Fluent® at the center of the cell adjacent to the wall. As the Green-Gauss cell-based gradient approach is used for this calculation, completely orthogonal and thin meshes with large aspect ratio should be adopted near the walls to reduce the discrete error made on the tangential temperature gradients at the walls. This is evidenced in Table 5.1 which shows the mass flowrates calculated with different meshes, with and without taking into account the temperature jump at the wall. As the temperature of the walls is uniform, the mass

flowrate should be zero when the temperature jump condition is not considered. This is of course not the case in our calculations, as the tangential temperature gradient is calculated at the center of the first cell. However, the error is largely reduced in the case of Mesh 1 which combines low thickness, good orthogonality and large aspect ratio for the first cell row. In all cases, the mass flowrate calculated without implementing a temperature jump condition is much lower than the one obtained with complete boundary conditions including temperature jump, which illustrates that the discrete error on  $\partial T / \partial s$  has a limited influence on the simulations. It is also worth to mention, comparing the mass flowrates obtained with no temperature jump for Meshes 1 and 4, that the orthogonality of boundary cells has a strong influence on the accuracy of the calculations.

**Table 5.1: Influence of thickness and orthogonality of the mesh at the walls on mass flowrate**

for  $d = h = 1 \mu\text{m}$ ,  $L = 4 \mu\text{m}$ ,  $T_h = 375 \text{ K}$ ,  $T_c = 225 \text{ K}$  and  $P = 1.013 \times 10^5 \text{ Pa}$

	Mesh 1	Mesh 2	Mesh 3	Mesh 4
Number of cells	8988	8847	22542	8445
Height of 1 <sup>st</sup> cells ( $\mu\text{m}$ )	0.001	0.002	0.001	0.001
Aspect ratio of 1 <sup>st</sup> cells	50	50	30	50
Orthogonality of wall layer	Good	Good	Good	Not good
$\dot{m}$ ( $\text{kg s}^{-1} \text{ m}^{-1}$ )	$2.52 \times 10^{-7}$	$2.54 \times 10^{-7}$	$2.60 \times 10^{-7}$	$3.05 \times 10^{-7}$
$\dot{m}_{\text{without } T_{\text{jump}}}$ ( $\text{kg s}^{-1} \text{ m}^{-1}$ )	$3.81 \times 10^{-9}$	$5.08 \times 10^{-9}$	$6.14 \times 10^{-9}$	$4.09 \times 10^{-8}$

According to this analysis, Mesh 1, whose local geometry near the wall around the tips of the ratchet is shown in Fig. 5.3, has been used in all the following simulations.

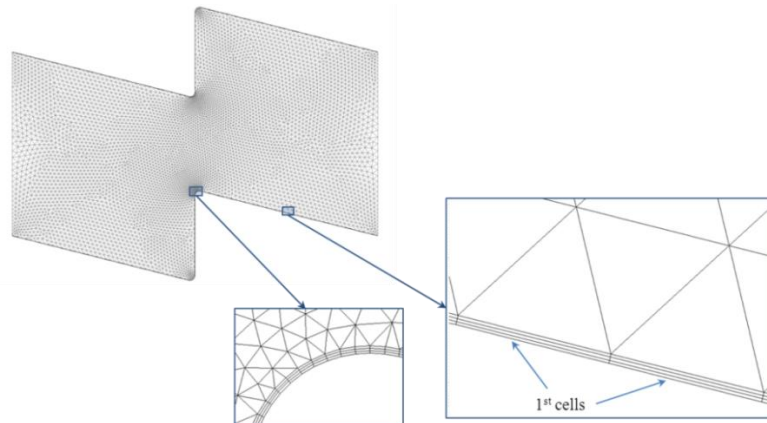


**Figure 5.3: Mesh 1 and details at the wall**

### 5.2.3. Comparison of the three configurations

An example of isotherms (a) and streamlines (b) calculated for the same boundary and pressure conditions in the three configurations are shown in Fig. 5.4 and the corresponding calculated mass flowrates are presented in Table 5.2.

The misalignment of the ratchet patterns in Config. 3 results in a large zone (shown with a dashed line in Fig. 5.4a) in which the upper and lower walls are closer and the normal temperature gradients larger. As a consequence, the thermal transpiration pumping effect is increased in this zone, leading to an increase of the generated mass flowrate of the order of 19 %.

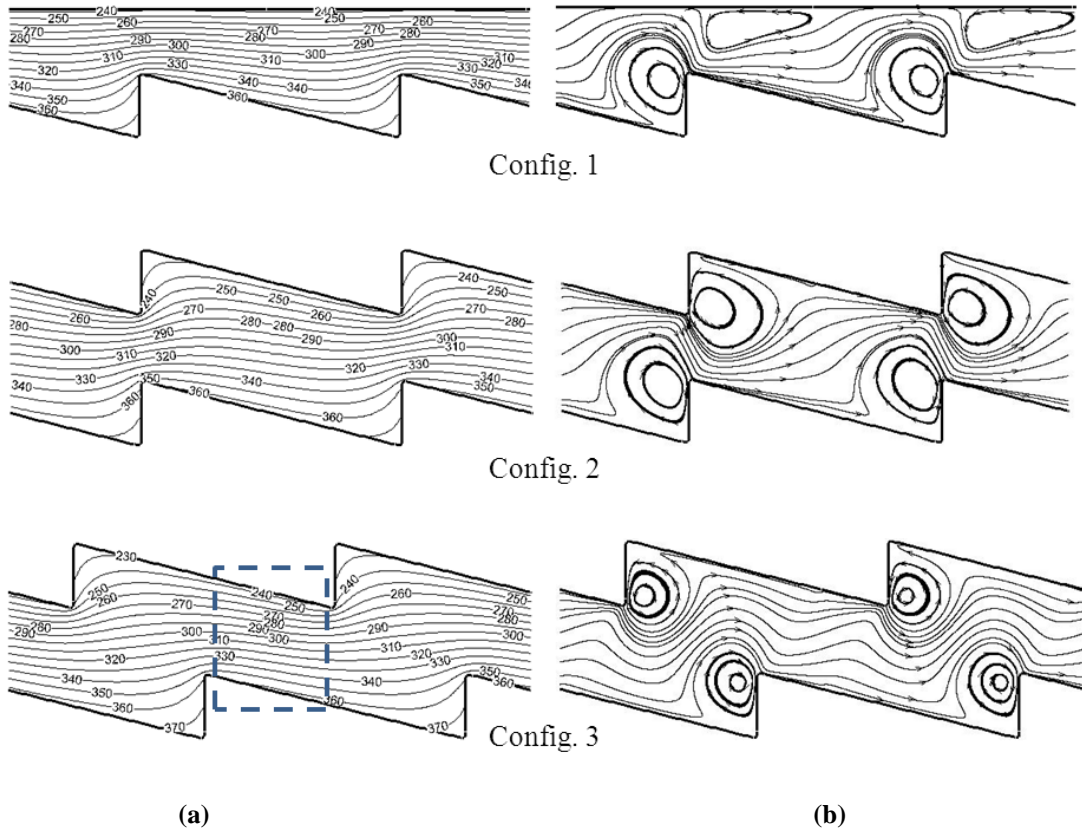


**Figure 5.4:** Isotherms (a) and streamlines (b) for the three configurations, with  $d = h = 1 \mu\text{m}$ ,  $L = 4 \mu\text{m}$ ,  $T_h = 375 \text{ K}$ ,  $T_c = 225 \text{ K}$  and  $P = 1.013 \times 10^5 \text{ Pa}$

**Table 5.2:** Mass flowrate per unit of width calculated for three configurations, with  $d = h = 1 \mu\text{m}$ ,  $L = 4 \mu\text{m}$ ,  $T_h = 375 \text{ K}$ ,  $T_c = 225 \text{ K}$  and  $P = 1.013 \times 10^5 \text{ Pa}$

	Config. 1	Config. 2	Config. 3
$\dot{m}$ ( $\text{kg s}^{-1} \text{ m}^{-1}$ )	$1.58 \times 10^{-7}$	$2.52 \times 10^{-7}$	$2.99 \times 10^{-7}$

In the three configurations, two counter-rotating vortices are generated near the upper and lower walls, as already evidenced by Hardt et al. (Hardt et al. 2013) in a geometry similar to the one of Config. 1. The size of these vortices and the induced reduction of the main flow section and distortion of streamlines are lower in Config. 3 than in the two other ones, which limits their resistive effect on the main flow and thus contributes to the observed increase of mass flowrate.

To better analyze the origin of the generated flow, the local velocity vectors for Config. 2 near the tip of the lower wall ratchet are shown in Fig. 5.5. The flow pattern is very similar to the one shown by Hardt et al. (Hardt et al. 2013): a thermal transpiration flow develops along the inclined wall due to the tangential temperature gradient, as also described by Würger (Würger 2011). However, a thermally induced flow is also generated along the vertical wall where the tangential temperature gradient is even larger than on the inclined one. This leads to the generation of the vortex which strongly limits the mass flowrate and can explain the discrepancy observed on the mean flow velocity between the present results and those of Würger, deduced from his simplified analytical model which neglects the effect of gas flow along the vertical wall. In the case of Config. 2 with  $d = h = 1 \mu\text{m}$ ,  $L = 4 \mu\text{m}$ ,  $T_h = 375 \text{ K}$ ,  $T_c = 225 \text{ K}$  and  $P = 1.013 \times 10^5 \text{ Pa}$  (which leads to a Knudsen number  $Kn$ , based on the mean temperature and ratchet depth, equal to 0.054), the present simulation gives a mean velocity of the order of  $0.1 \text{ m s}^{-1}$  and the model of Würger predicts a velocity three times higher.

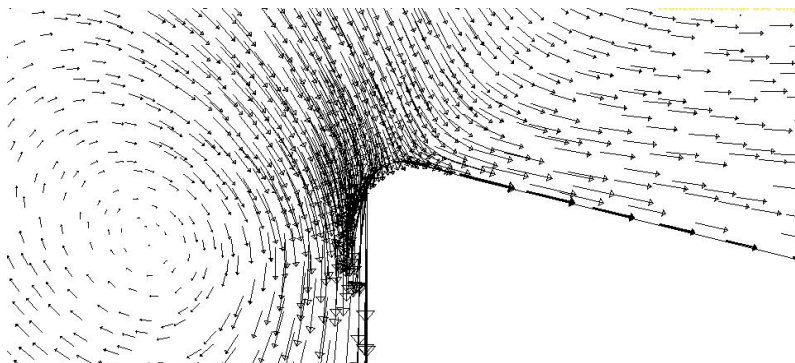


Figure 5.5: Velocity vectors near a tip of the lower ratchet surface for Config. 2

### 5.2.4. Parameter analysis

Config. 3 which showed the best pumping performance in the previous analysis is used to examine the influence of the operating conditions (Knudsen number, temperature difference  $\Delta T = T_h - T_c$ ) and geometrical parameters (ratchet angle  $\alpha$  and distance  $h$  between the two surfaces) on the pumping efficiency of the device.

The following geometrical dimensions and operating conditions applied on Config. 3 constitute the reference conditions of this parametric analysis. The ratchet is defined by a depth  $d = 1 \mu\text{m}$  and a length  $L = 4 \mu\text{m}$ , and the channel gap  $h = 1 \mu\text{m}$  is equal to the ratchet depth. The temperature of the hot and cold ratchet walls are  $T_h = 375 \text{ K}$  and  $T_c = 225 \text{ K}$ , respectively. The pressure  $P = 1.013 \times 10^5 \text{ Pa}$  is at atmospheric conditions, which leads to a Knudsen number  $Kn$ , based on the mean temperature and ratchet depth, equal to 0.054. These reference conditions are indicated in bold font in Tables 5.3-5.5.

#### Influence of the Knudsen number

The influence of the Knudsen number is studied by considering different values of pressure ranging from 101.3 kPa to 400 kPa. All other parameters are those of the reference conditions. The resulting investigated Knudsen number is in the range 0.019 to 0.054. The calculated mass flowrate  $\dot{m}$  per unit of width of the channel and the mean velocity  $\bar{u}_x$  in the  $x$ -direction are given in Table 5.3, in which the data for the reference conditions are in bold.

**Table 5.3: Mass flowrate versus Knudsen number for reference conditions except pressure level**

$Kn$	<b>0.054</b>	0.062	0.057	0.049	0.037	0.025	0.019
$\dot{m}$ ( $10^{-7} \text{ kg s}^{-1} \text{ m}^{-1}$ )	<b>2.99</b>	2.82	2.74	2.56	2.25	1.81	1.52
$\bar{u}_x$ ( $\text{m s}^{-1}$ )	<b>0.126</b>	0.102	0.092	0.075	0.051	0.028	0.018

Figure 5.6 shows that, as expected, the mass flowrate increases with  $Kn$  in the part of the slip flow regime covered by this study. The slope of the curve tends to decrease while  $Kn$  increases, which suggests that a maximal value of the flowrate could be reached for a Knudsen number of the order of  $10^{-1}$ , in agreement with the value found by Donkov et al. (Donkov et al. 2011). This will be discussed in Section 5.3.2 thanks to complementary DSMC simulations.

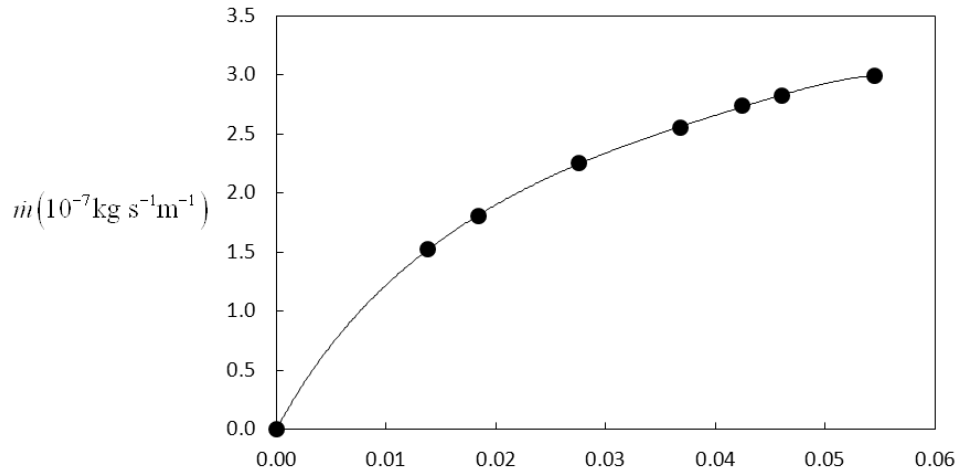


**Figure 5.6: Mass flowrate per unit of width versus Knudsen number**

Influence of the temperature difference

The influence of the temperature difference  $\Delta T$  between the two walls is studied by changing in the reference conditions the temperature of the two surfaces, while maintaining a constant mean temperature  $(T_c + T_h)/2 = 300 \text{ K}$ . The Knudsen number based on this mean temperature is then constant ( $Kn = 0.054$ ). Figure 5.7 shows that the mass flowrate increases almost linearly with the temperature difference  $\Delta T$ . The mass flowrate per unit of width increases of about  $2 \times 10^{-7} \text{ kg s}^{-1} \text{ m}^{-1}$  for a temperature increase of 100 K.

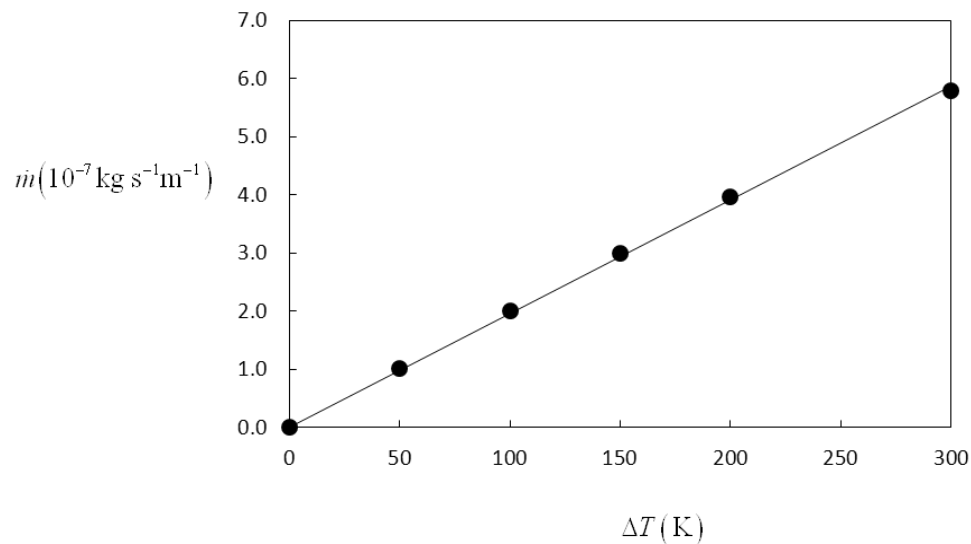


**Figure 5.7: Mass flowrate per unit of width versus temperature difference**

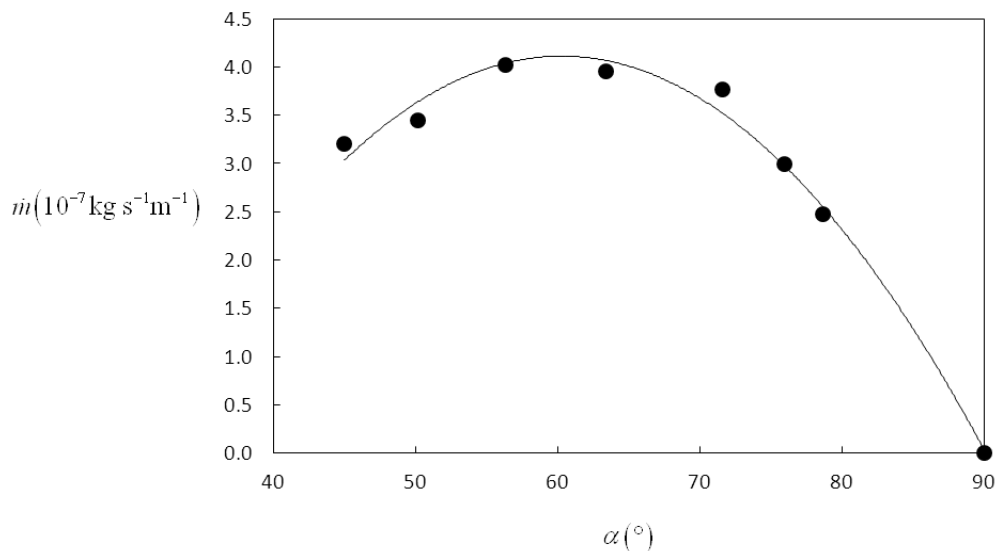
Influence of the ratchet angle

The influence of the ratchet angle  $\beta$  on the pumping effect is studied by varying the pattern length  $L$ , while keeping all other parameters of the reference conditions. The limit angle values  $\beta=0$  or  $\beta=90^\circ$  break the asymmetry of the structured surfaces and naturally lead to a zero net flowrate. As a consequence, a maximum value of the flowrate is expected for an optimal value of the angle. Simulations are performed with a pattern length  $L$  varying from 1.0 to 5.0  $\mu\text{m}$ , which corresponds to an angle  $\beta$  between  $45^\circ$  and  $79^\circ$ . Table 5.4 shows the values of the mass flowrate  $\dot{m}$  per unit of width and the corresponding mean velocity  $\bar{u}_x$  in the channel direction.

**Table 5.4: Mass flowrate per unit of width and mean velocity versus ratchet angle**

$L$ ( $\mu\text{m}$ )	1.0	1.2	1.5	2.0	3.0	<b>4.0</b>	5.0
$\beta$ ( $^\circ$ )	45	50	56	63	72	<b>76</b>	79
$\dot{m}$ ( $10^{-7} \text{ kg s}^{-1} \text{ m}^{-1}$ )	3.20	3.44	4.02	3.96	3.77	<b>2.99</b>	2.48
$\bar{u}_x$ ( $\text{m s}^{-1}$ )	0.175	0.153	0.178	0.166	0.156	<b>0.126</b>	0.107

As expected, an optimal value of the angle is found, close to  $\beta=60^\circ$ , with a mean velocity of the order of  $0.17 \text{ m s}^{-1}$ . The decrease of the flowrate is significant when the angle deviates from its optimal value (Fig. 5.8); for example a decrease of  $7^\circ$ , from  $\beta=79^\circ$  to  $\beta=72^\circ$ , results in an increase of the mass flowrate of 52 %.

**Figure 5.8: Mass flowrate per unit of width versus ratchet angle**

Influence of the distance between the walls

The influence of the wall gap  $h$  on the mean velocity and mass flowrate is now analyzed with all other parameters corresponding to the reference conditions. Figure 5.9 shows that the mass flowrate  $\dot{m}$  increases with  $h$  and tends toward a limit value of the order of  $4.5 \times 10^{-7} \text{ kg s}^{-1} \text{ m}^{-1}$ . This limit results from the decrease of the local tangential temperature gradient  $\partial T / \partial s$ , directly linked to a decrease of the normal gradient  $\partial T / \partial n$ , as the distance  $h$  between the walls increases.

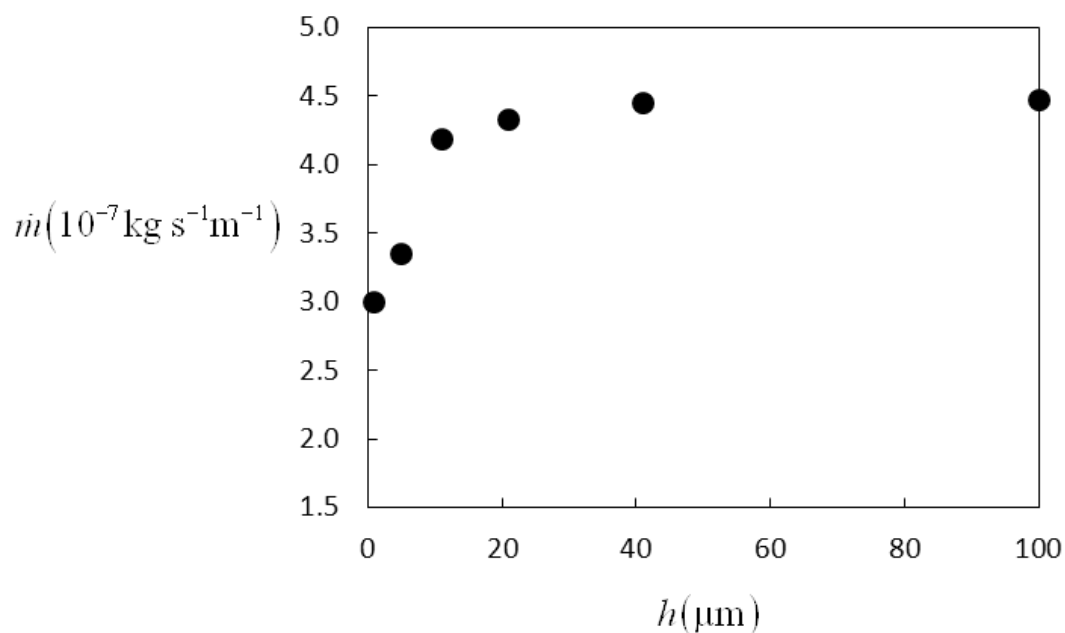


**Figure 5.9: Mass flowrate versus distance between channel walls**

This results in a strong decrease of the mean velocity, as illustrated in Fig. 5.10. In this figure, the mean velocity is compared with the estimation proposed by Würger (Würger 2011). A similar trend is observed. The calculation of Würger, however, overestimates the mean velocity value even if it provides a correct order of magnitude estimation.

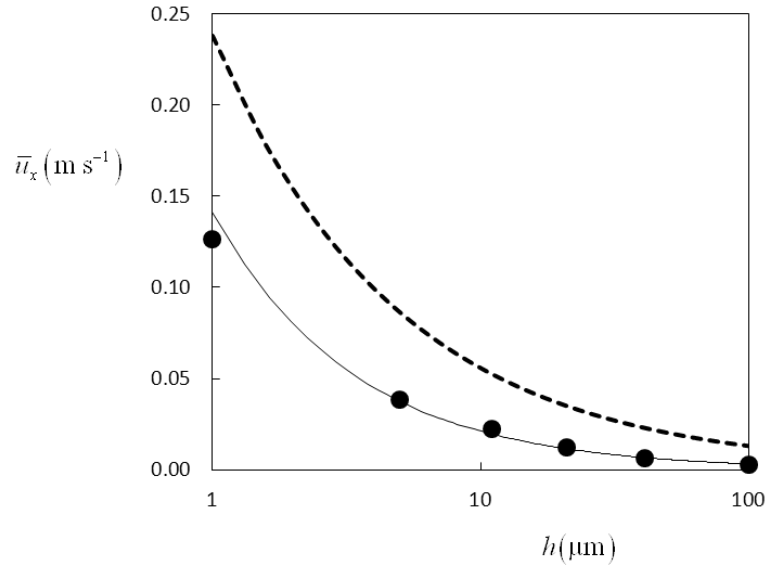


**Figure 5.10: Mean velocity versus distance between channel walls (•) and comparison with the estimation from (Würger 2011) (dashed line)**

In order to see if the pumping effect is significant, it is compared to an isothermal pressure-driven flow in a plane microchannel of depth  $h$ , in the same operating conditions (pressure and mean temperature). The pressure gradient  $dP/dx$  required for generating the same flowrate is given in the last line of Table 5.5. If a 1 mm long microchannel is considered, the pressure difference between its inlet and outlet is  $\Delta P = 2.29$  kPa for a gap  $h = 1 \mu\text{m}$ , which remains significant, but this value dramatically decreases as  $h$  increases:  $\Delta P = 3.21$  Pa for a gap  $h = 11 \mu\text{m}$ . As a consequence, in this latter case, the thermal pumping effect would be cancelled by any small pressure drop observed upstream or downstream to the micropump unit.

**Table 5.5: Mass flowrate per unit of width, mean velocity, pressure gradient required for an equivalent pressure-driven flow and heat flux at the wall versus distance between the walls**

$h$ ( $\mu\text{m}$ )	1	5	11	21	41	100
$\dot{m}$ ( $10^{-7} \text{ kg s}^{-1} \text{ m}^{-1}$ )	<b>2.99</b>	3.35	4.18	4.33	4.45	4.47
$\bar{u}_x$ ( $\text{m s}^{-1}$ )	<b>0.126</b>	0.038	0.023	0.012	0.007	0.003
$dP/dx$ ( $\text{Pa m}^{-1}$ )	<b><math>2.29 \times 10^6</math></b>	$2.62 \times 10^4$	$3.21 \times 10^3$	$4.87 \times 10^2$	$6.75 \times 10^1$	$4.70 \times 10^0$
$q$ ( $\text{W m}^{-2}$ )	<b><math>1.19 \times 10^6</math></b>	$3.98 \times 10^5$	$1.98 \times 10^5$	$1.08 \times 10^5$	$5.65 \times 10^4$	$2.35 \times 10^4$

The dramatic decrease of pumping efficiency as the distance between the walls is increased is also due to the fact that, as the walls are moved away, the pumping effect is more localized close to the walls. This point is illustrated in Fig. 5.11, which shows the profile of velocity magnitude  $\|\mathbf{u}\|$  along a cross section of the channel ( $y^* = y/h$ ) at a distance  $x = 0.45L$  from the ratchet tip. As the distance between the walls increases, the profile flattens and the velocity rapidly decreases far to the walls.

In practice, the design of the pump requires then a small  $h$  value, together with a high number of stages, i.e. a long micro-structured channel, in order to preserve the pumping efficiency of the thermal micropump: the flowrate does not depend on the number of stages but the effect of a counter-pressure decreases as the number of stages increases, up to become negligible.

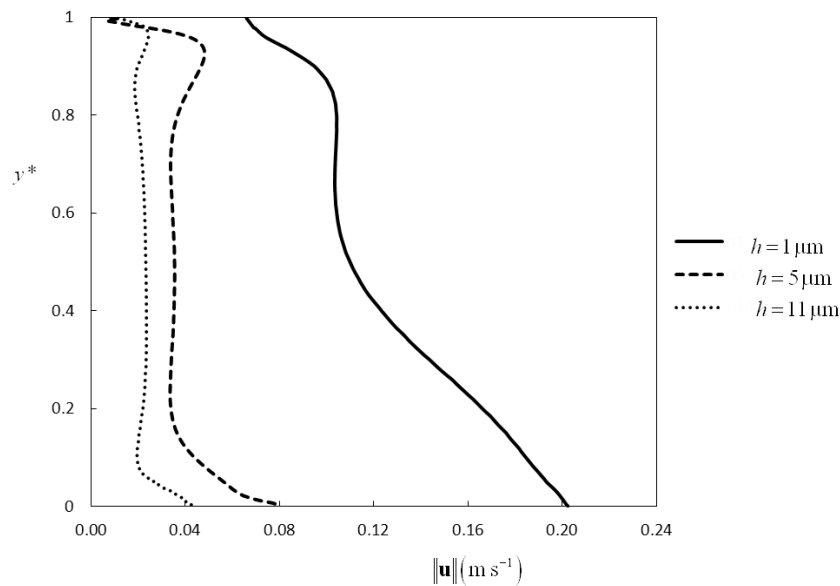


**Figure 5.11: Profiles of velocity magnitude in the cross-section  $x = 0.45 L$  for different distances between the two ratchet walls**

On the other hand, reducing the distance between the walls results in a rapid increase of the heat flux  $q$  leaving the hot wall. For the smallest distance,  $h = 1\mu\text{m}$ , the required heat flux is  $q = 119 \text{ W cm}^{-2}$ , which is rather high but remains acceptable compared with heat fluxes usually observed in micro heat exchangers, of the order of several hundreds of  $\text{W cm}^{-2}$  (Kandlikar et al. 2005). Regarding the global efficiency of the device, Knudsen pumps are devices with high entropy generation and the

thermal power required for generating a given flowrate is typically  $10^6$  higher than the mechanical power required for generating the same flowrate by a pressure difference. But if the above described single-stage micropump is compared to a classic Knudsen micropump made of two reservoirs connected by a single microchannel, it can be easily calculated that the thermal energy consumption in the classic pump can be much higher than in the ratchet device, due to conjugate heat transfer from one reservoir toward the other reservoir through the solid wall. Thus, the ratchet design can be an attractive alternative to more classic designs of thermally-driven micropumps.

### 5.3. DSMC Simulation

DSMC simulations have been realized in order to characterize the performances of the ratchet pump at higher rarefaction levels.

#### 5.3.1. Problem statement

The studied configuration which consists of two hot and cold ratchet walls with misaligned identical saw-tooth patterns is shown in Fig. 5.12.

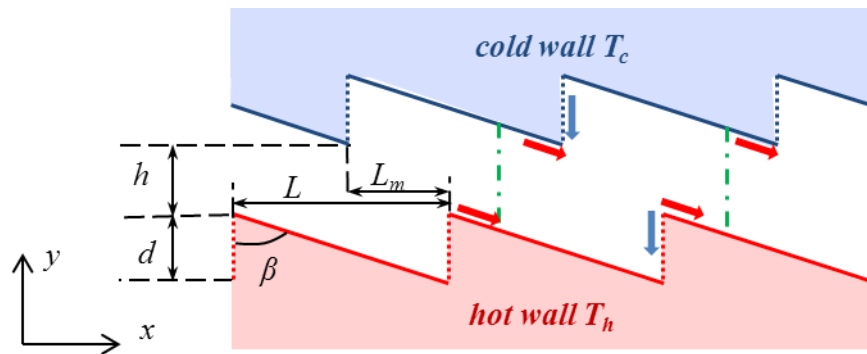


Figure 5.12: Configuration and geometric parameters

The ratchet surfaces have a periodic pattern with a length  $L$  in the  $x$ -direction and a height  $d$  in the  $y$ -direction, resulting in an angle  $\beta = \arctan(L/d)$ . Periodic boundary conditions are implemented at the inlet and outlet, the positions of which are indicated by the green dot-dashed lines in Fig. 5.12. The distance  $h$  between the walls is defined from the planes of the ratchet tips. The gap in the  $x$ -direction between the two facing patterns is defined by the length  $L_m$ . The model geometry is close to the third configuration previously studied and shown in Fig. 5.2c. In order to simplify

the mesh generation and reduce the computational time, a sharp angle at the intersection of the segments is adopted in the DSMC study, instead of the finite curvature introduced in previous studies to take into account realistic micro fabrication constraints. The Knudsen number is defined as Eq.(5.1).

A multi-block mesh is adopted to simplify the grid generation. The whole calculation domain is divided into several blocks according to the geometry, i.e. three subdomains are used for the configuration shown in Fig. 5.12. Each geometry domain is discretized by using uniform quadrilateral cells, with a typical cell size which is smaller than  $1/3$  of the mean free path. A Hard Sphere (HS) model and the No Time Counter (NTC) scheme are used in the collision algorithm.

The macroscopic quantities are calculated by averaging the microscopic values of the test molecules on a given sampling cell over a large number of time steps. The sampling cell includes 4 collision cells, in each of which about 40 test molecules are arranged in the present simulations. Therefore the sampling size is defined as the product of the number of test molecules per cell, the number of collision cells in a sampling cell and the number of time steps during which the sampling is performed. Due to the very low macroscopic velocity of the gas flow, the simulations are carried out with a large sampling size of  $10^8$ .

Regarding boundary conditions, each surface is assumed isothermal. The well-known Maxwell's specular-diffuse model is applied, according to which a fraction  $(1-\alpha)$  of the molecules is reflected specularly while the remaining fraction  $\alpha$  is reflected diffusely in accordance with the Maxwellian velocity distribution. This dimensionless coefficient  $\alpha$  is the so-called accommodation coefficient, as the Maxwell boundary condition does not distinguish the tangential momentum and energy accommodation coefficients. The accommodation coefficients for vertical walls and inclined walls are noted  $\alpha_v$  and  $\alpha_l$ , respectively.

### 5.3.2. Reference configuration

A reference configuration is considered for further discussion. In this reference configuration, the geometric parameters of the ratchet are  $L = 4 \mu\text{m}$ ,  $h = d = 1 \mu\text{m}$  and  $L_m = L/2$ . The reference temperatures of the hot and cold walls are  $T_h = 375 \text{ K}$  and  $T_c = 225 \text{ K}$ , respectively. A completely diffuse reflection boundary condition is considered for all walls in the reference configuration, i.e.  $\alpha_v = \alpha_l = 1$ .

Since two dimensional simulations are implemented in this work, a reasonable width of  $20 \mu\text{m}$  in the  $z$ -direction is considered when the mass flowrates are calculated. The influence of the temperature difference, the Knudsen number, the accommodation coefficients and geometric parameters, i.e. the ratchet angle  $\beta$  and the misalignment gap  $L_m$ , is analyzed in the following sections.

### 5.3.3. Temperature distribution and flow characteristics

As a consequence of the geometry and boundary conditions, the dominated temperature gradient is perpendicular to the surfaces, in contrast with conventional thermal transpiration flows generated by an imposed tangential temperature gradient along the walls. However, due to the ratchet geometry, the normal temperature gradient close to the walls is not uniform and results in a tangential temperature gradient and a corresponding thermal stress in the gas along the ratchet surface. Figure 5.13 shows the tangential temperature gradients along the inclined and the vertical walls of the ratchet surfaces for  $Kn = 0.184$ . It is found that strong temperature gradients appear near the tips of the ratchet and sharply decrease getting away from the tips. Therefore the main thermally-driven flow is generated near the tips as shown by arrows. The red arrows (Fig. 5.13a) show flows generated by the inclined walls (solid lines) and the blue ones (Fig. 5.13b) correspond to the flows due to vertical walls (dotted lines). The general trend and the order of magnitude of the temperature gradient along the inclined wall are comparable with the analytical results provided by Eq. (6) in (Würger 2011) and a mean flow in the  $x$ -direction is expected from Fig. 5.13. The temperature gradient along the vertical wall is omitted in the simplified analytical model of Würger; however, around the tips of the ratchet, the temperature varies more rapidly along the vertical segments than along the inclined segments. As a consequence, the flow generated by the vertical walls, shown by the blue arrows, is stronger than the flow due to the inclined walls. It results in a two-dimensional flow rather than in a uniform flow in  $x$ -direction, as predicted in (Würger 2011). Finally, the actual flow field is a result of the combination of these local thermally-driven flows.

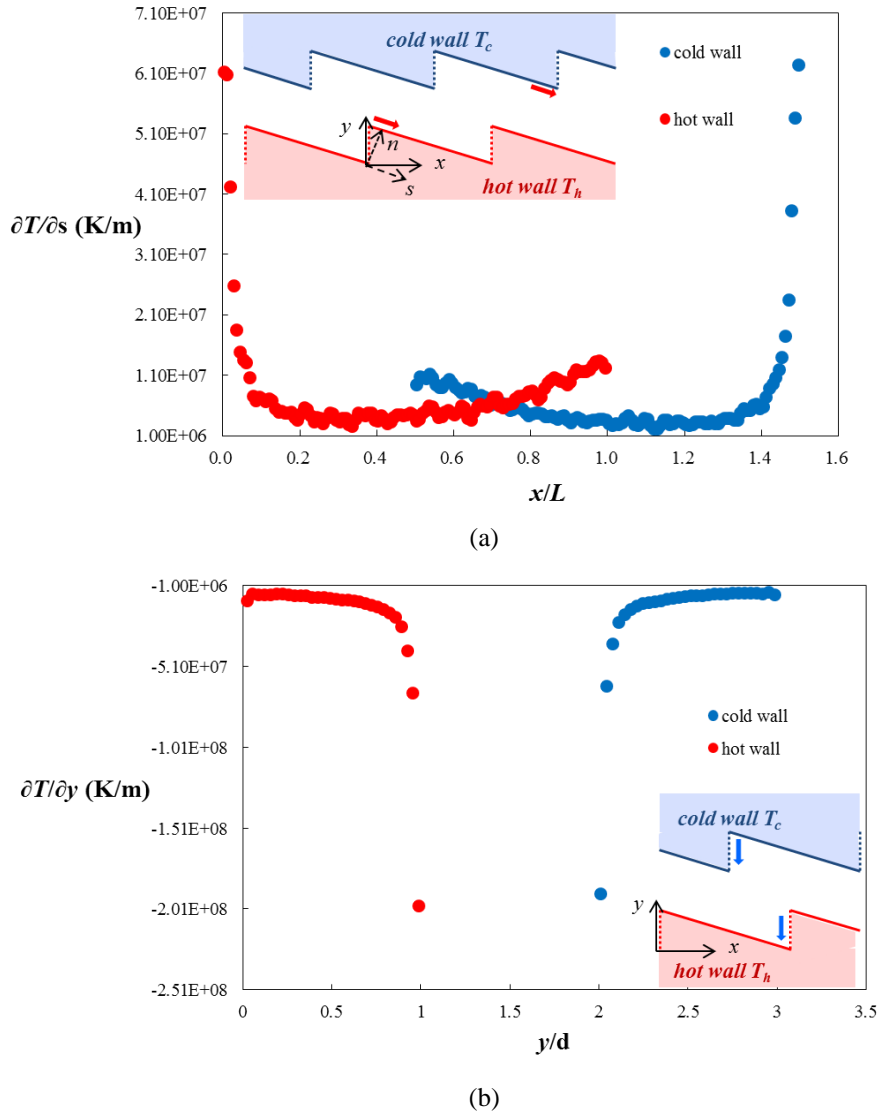


**Figure 5.13: Tangential temperature gradients in the gas close to the ratchet surfaces for the reference case at  $Kn = 0.184$  along the a) inclined walls, b) vertical walls**

Figure 5.14 presents the velocity vectors and the iso-contours of velocity magnitude. It is found that the larger velocity appears near the tips of the ratchet, which are at the origin of the flow. The vertical walls have a partial but significant contribution to the flow in the  $x$ -direction, especially at the upper ratchet surface. The vertical walls also lead to the generation of vortices which strongly reduce the mean mass flowrate in the  $x$ -direction. Consequently, the final flow pattern and the net flowrate observed in the  $x$ -direction closely depend on the strength of the two local thermally-driven flows, which are related to geometric parameters, operating

conditions such as temperature differences, pressure, as well as surface conditions, e.g. accommodation coefficients values.

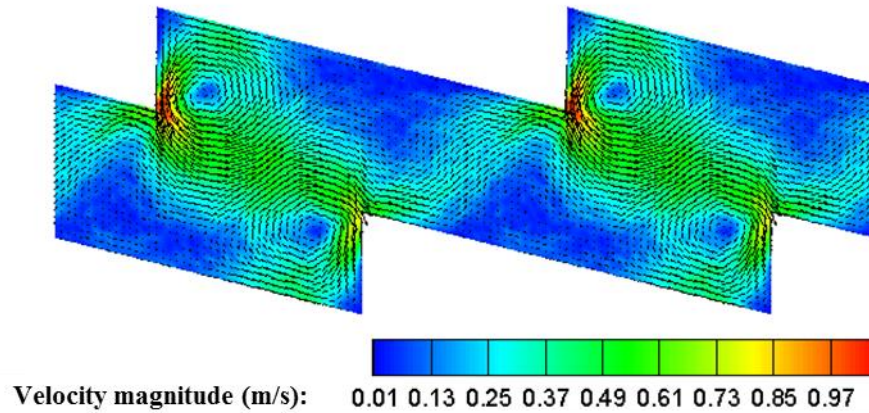


**Figure 5.14: Velocity vectors and iso-contours of velocity magnitude for the reference case at  $Kn = 0.16$**

As shown in Fig. 5.14, the flow induced by the temperature difference between the two ratchet surfaces is much more complex than in a simple classical thermal transpiration flow. It is interesting to discuss the effect induced by this configuration. As the temperature gradient is not imposed directly on the surfaces, the flow induced by the temperature field is a secondary effect which is different from a typical thermal transpiration flow or a typical thermal-stress flow. In the slip flow regime, it could be considered as a kind of thermal transpiration flow due to the modified temperature field induced by the first-order temperature jump at the wall, which is the reason why very similar temperature and velocity fields are obtained by DSMC and from the Navier-Stokes equations associated with first-order slip boundary condition in the previous section. However, the thermal stress effect due to the non-uniform temperature gradient also plays a role in the flow. As indicated in Sone's book (Sone 2007), this flow should be in the opposite direction of the thermal transpiration flow. Comparing the velocity field (Fig. 5.14) obtained by DSMC with the results from CFD (Fig. 5.4) which does not take into account thermal stress, DSMC reveals a third circulation zone near the lower surface which is likely due to the thermal stress effect. The competition between thermal transpiration flow and thermal stress flow has recently been analyzed for a thermally driven cavity flow (Mohammadzadeh et al.

2015), but the present geometry and flow structure are more complex and it is here difficult to uncouple the two kinds of flows.

The temperature difference between the two surfaces is the main factor controlling this thermally-driven flow. Thus, the influence of the temperature difference  $\Delta T$  is studied by changing the temperature of the two surfaces while maintaining a constant mean temperature  $T_0 = 300$  K. Figure 5.15 shows that the mass flowrate linearly increases with the temperature difference  $\Delta T$ . Even for a small temperature difference  $\Delta T = 50$  K, a significant mass flowrate of  $7.69 \times 10^{-13}$  kg s<sup>-1</sup> is obtained, which is measurable with a good accuracy for pressure driven (Bergoglio et al. 2015) as well as for temperature driven gas microflows (Rojas-Cárdenas et al. 2013).

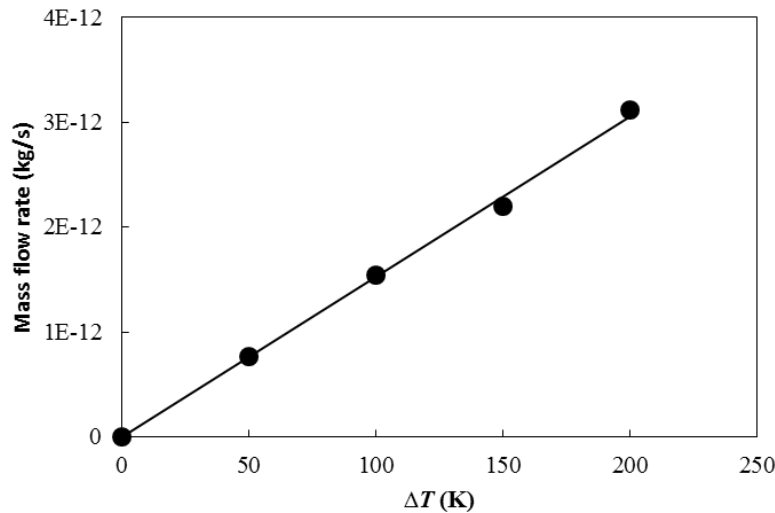
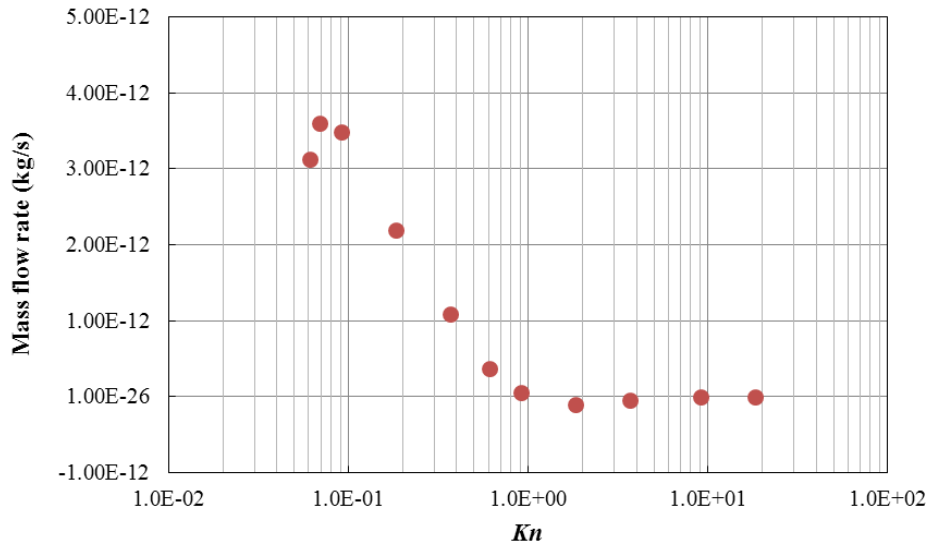


Figure 5.15: Mass flowrate for different temperature differences

### 5.3.4. Influence of the Knudsen number

The influence of the Knudsen number is investigated by considering different initial densities. Figure 5.16 shows the obtained mass flowrate by DSMC (red points) versus the Knudsen number. A maximal value of the mass flowrate is reached at a Knudsen number of about 0.07. For larger Knudsen numbers, the mass flowrate decreases rapidly and becomes 100 times smaller than its higher value at  $Kn = 0.92$ . It is found that the mass flowrates are negative in the Knudsen number range [1.0; 10.0], which indicates that the mean flow in the full transition and early free molecular regimes is in the opposite direction compared to the flow in the slip and

early transition regimes. A minimal value of the mass flowrate appears at  $Kn \approx 1.1$ . The values of the mass flowrate in the opposite direction are much lower because of a lower mean density reached for larger Knudsen numbers.



**Figure 5.16: Mass flowrate versus Knudsen number**

Nevertheless, the opposite flow is clearly observed by checking the mean velocity across the vertical faces (green dot-dashed lines in Fig. 5.12) where the periodic boundary condition is imposed, as shown in Fig. 5.17. The maximal mean velocity is found at  $Kn = 0.184$  and the minimal value is observed at  $Kn = 1.84$ . The maximal and minimal values of the mass flowrate (Fig. 5.16) and of the mean velocity (Fig. 5.17) are not observed for the same values of the Knudsen number, due to the influence of the density which depends both on the local pressure and temperature.

#### Comparisons between DSMC and CFD results

Now, the mass flowrates obtained by the DSMC (home code) are compared to the results obtained by CFD as well as to those obtained by the open source code *dsmcFoamStrath* (see Fig. 5.18). In addition to the results obtained in Section 5.2.2, another group of CFD results obtained using the classical Maxwell boundary condition is presented. Both DSMC codes give a maximal mass flowrate near  $Kn = 0.07$  but the CFD simulations fail to predict the decrease of mass flowrate and capture this maximal value. The CFD calculated mass flowrates are larger than the DSMC ones. Different factors can explain the discrepancies observed between DSMC and CFD results.

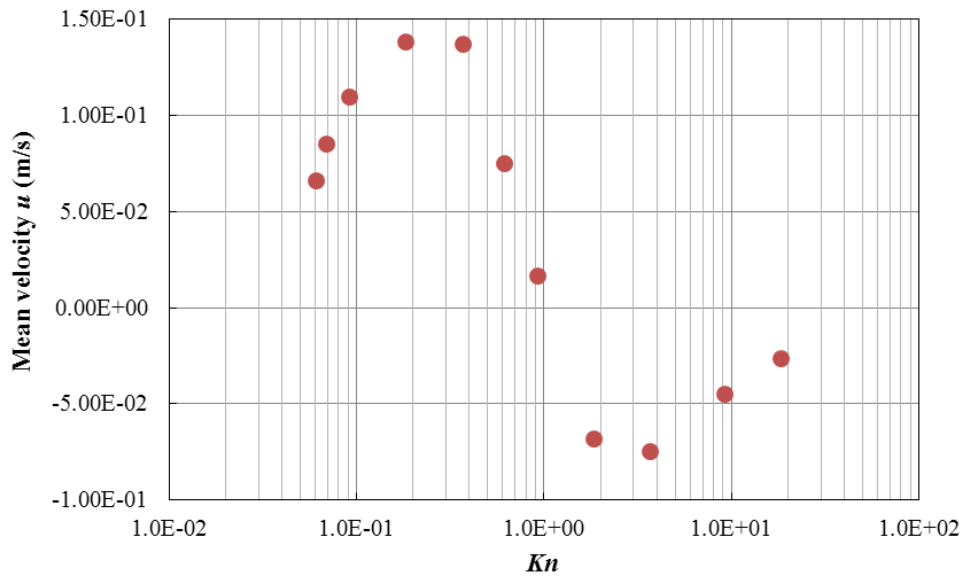


Figure 5.17: Mean velocity versus Knudsen number

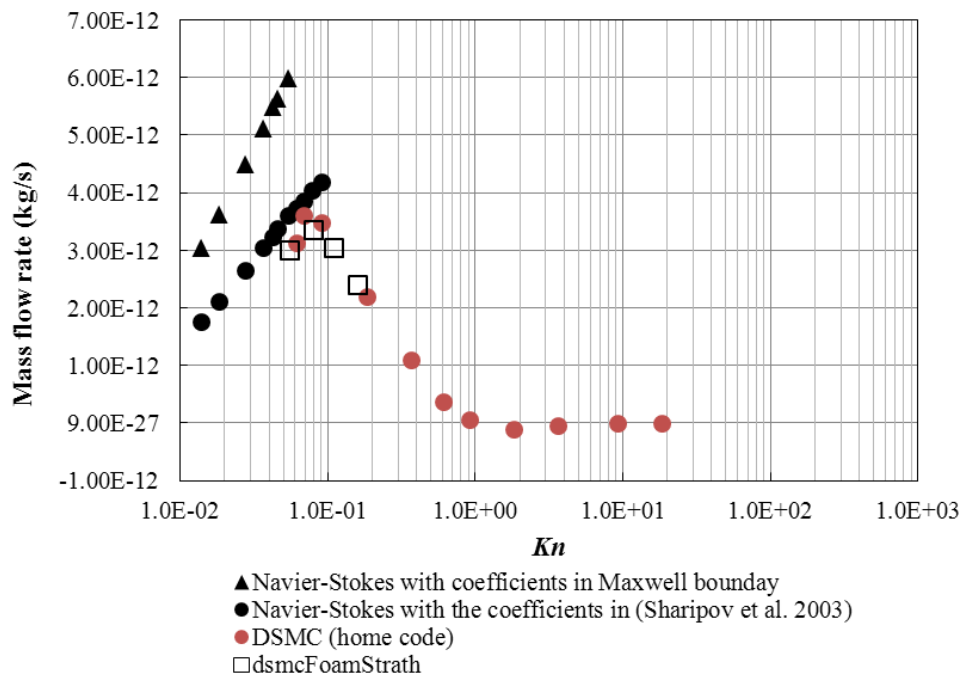


Figure 5.18: Comparison of mass flowrates obtained by DSMC and CFD

Firstly, the geometric configurations simulated by CFD and DSMC have some small differences. As mentioned before, a sharp angle at the intersection of the segments is considered in the DSMC study, instead of the finite curvature introduced in CFD studies. Several CFD simulations were carried out to roughly estimate the influence of the simplifying assumption which consists in neglecting the radius of

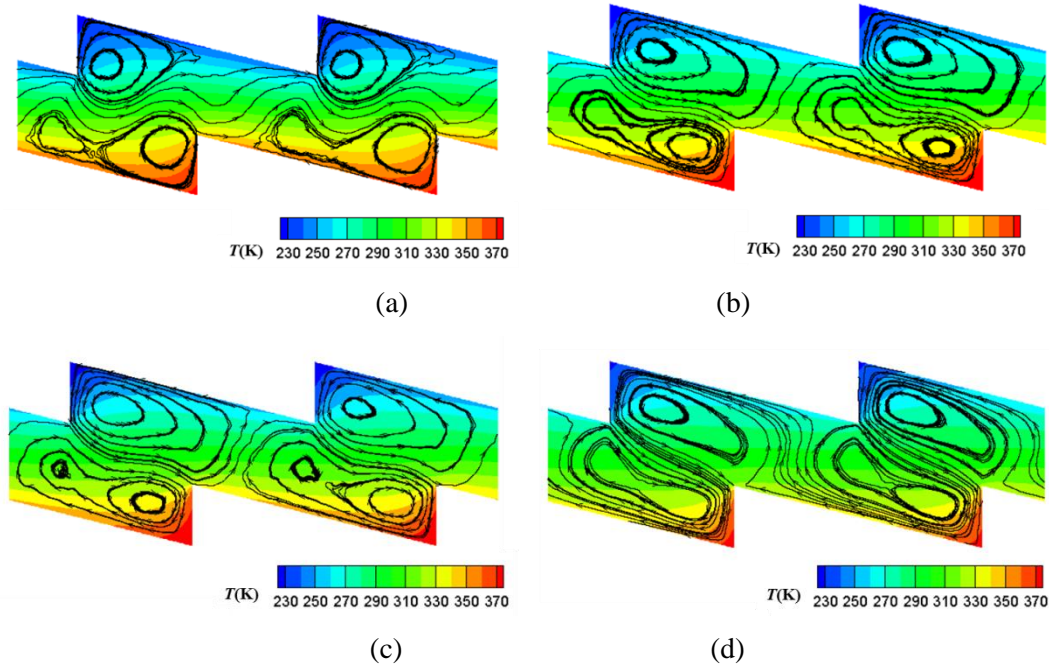
curvature at the tip. It was found that the mass flowrate obtained with sharp angles increases of about 15 % to 30 % compared to the case of a radius of curvature  $r = 50$  nm, and that this increase depends on the Knudsen number and temperature difference. As shown in Section 5.3.3, the strong tangential temperature gradients appearing around the tips are the principal factors driving the main flow. Therefore, the influence of the shape of the ratchet tips and of their radius of curvature, which are key factors for the design and fabrication of a micropump, will be studied in detail in a future work.

Secondly, CFD results strongly depend on the coefficients of the velocity slip and temperature jump boundary conditions, namely the velocity slip, the thermal slip and the temperature jump coefficients. There is a large deviation between results obtained by classical Maxwell boundary conditions and by the boundary condition with the coefficients recommended in (Sharipov 2003). The main difference comes from the thermal slip coefficients: 0.75 in Maxwell boundary conditions and 1.175 suggested by Sharipov, which are associated to different expressions of the mean free path. Besides, for small Knudsen numbers, more test molecules in each cell and a higher number of time steps are necessary to limit the statistical error in DSMC calculations. However, for a sampling size ranging from  $2 \times 10^8$  to  $4 \times 10^8$ , the maximal fluctuation on the mass flowrate is around 2 % at  $Kn = 0.184$ , 5 % at  $Kn = 0.092$  and reaches 10 % at  $Kn = 0.069$ . Nevertheless, the decrease of the mass flowrate from its maximal value in the slip regime when  $Kn$  decreases is clearly captured by DSMC simulations.

#### Velocity and temperature fields analysis

In Fig. 5.19, the streamlines and the iso-contours of temperature magnitude are displayed for several representative cases corresponding to  $Kn = 0.184, 0.613, 0.920$  and  $1.840$ . It can be seen that the isotherms have a complex distribution, due to the ratchet geometry and the low conductivity of the gas. The tangential temperature gradient near the structured walls is evidenced. On the one hand, the higher the value of the Knudsen number is, the more strongly the temperature of the gas near the walls deviates from the temperature of the walls and the smaller the temperature variations within the gas are. On the other hand, for larger Knudsen numbers, the temperature field near the inclined walls around the tips is more homogenous and is closer to the average temperature as shown in Fig. 5.19d,

while the obviously large temperature gradient along the vertical wall is kept. It probably reduces the effect of the inclined wall in the competition between the flows generated by inclined and vertical walls, which results in a vortices growth as the Knudsen number increases.



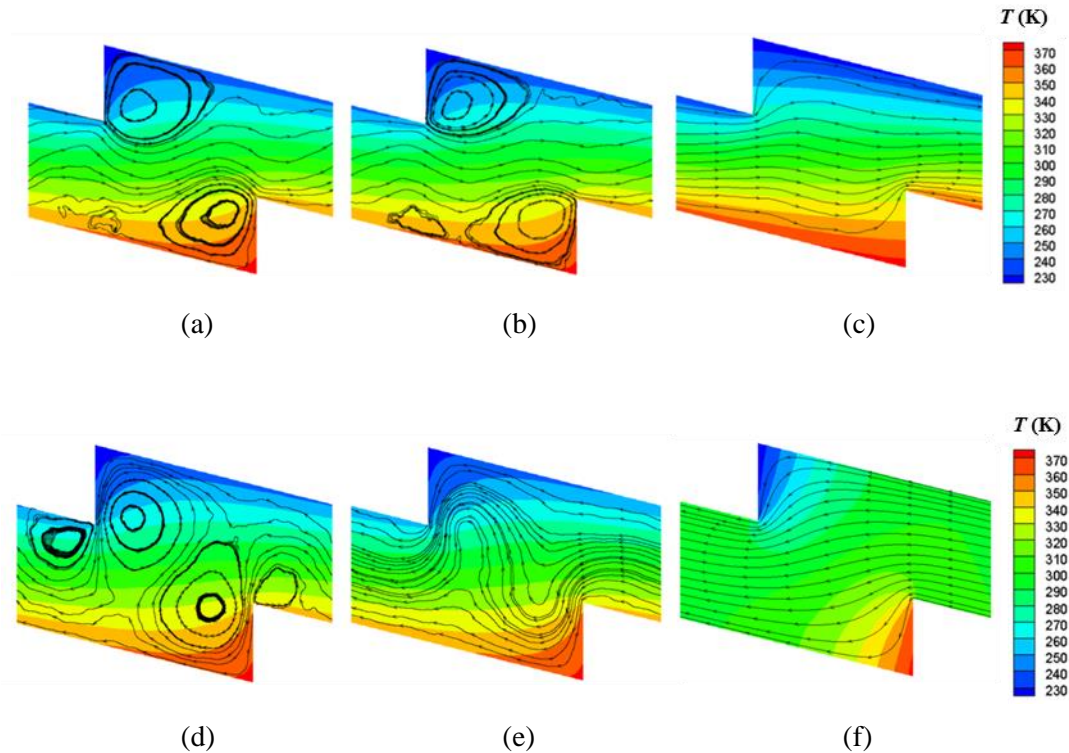
**Figure 5.19: Streamlines and iso-contours of temperature for different values of the Knudsen number: a)  $Kn = 0.184$ , b)  $Kn = 0.613$ , c)  $Kn = 0.920$  and d)  $Kn = 1.840$**

Figure 5.19 shows totally different flow patterns at  $Kn = 0.184$  and  $Kn = 1.840$ . Two vortices appear in the corners of the ratchets and maintain a flow in the  $x$ -direction in the center of the channel for  $Kn = 0.184$  and the lower vortices can contain two secondary vortices. Up to  $Kn = 0.920$ , the main flow is still a rather simple wavy flow going from left to right along a line which curvature increases with  $Kn$  due to the increasing place occupied by the vortices. At  $Kn = 1.840$ , the vortices are so stretched that they block the main flow in the  $x$ -direction, leading to a more complex serpentine flow in the opposite direction, from right to left.

### 5.3.5. Influence of the accommodation coefficients

In order to separately analyze the effects of the vertical and inclined walls, different accommodation coefficients on the vertical walls and inclined walls are now considered. The temperature iso-contours and the streamlines are shown in Fig. 5.20 for various values of the accommodation coefficients  $\alpha_v$  and  $\alpha_l$ . For a quantitative

analysis, the calculated mass flowrates are listed in Tables 5.6 and 5.7. The competition between the flows generated by the vertical and the inclined walls is clearly shown by the streamlines in Fig. 5.20.



**Figure 5.20: Temperature contours and streamlines for  $Kn = 0.184$  and different values of the accommodation coefficients  $\alpha_v$  and  $\alpha_i$  :**

- a)**  $\alpha_v = 0.9$ ,  $\alpha_i = 1$ ; **b)**  $\alpha_v = 0.8$ ,  $\alpha_i = 1$ ; **c)**  $\alpha_v = 0$ ,  $\alpha_i = 1$ ;  
**d)**  $\alpha_v = 1$ ,  $\alpha_i = 0.9$ ; **e)**  $\alpha_v = 1$ ,  $\alpha_i = 0.8$ ; **f)**  $\alpha_v = 1$ ,  $\alpha_i = 0$ .

When the accommodation coefficient  $\alpha_v$  decreases (Figs. 5.20a to 5.20c), which corresponds to a smaller effect of the vertical walls, the two vortices become smaller and more fluid can flow between them. When the inclined walls are completely diffusive ( $\alpha_i = 1$ ), whatever the value of the accommodation coefficients  $\alpha_v$  on the vertical walls, the flows is generated in the positive  $x$ -direction. Conversely, when  $\alpha_i$  is reduced, two additional vortices are generated near the tips of the ratchet (see Fig. 5.20d for  $\alpha_i = 0.9$  to be compared with the reference case of Fig. 5.19a for which  $\alpha_i = 1$ ) and the net flowrate becomes negative. The vortices disappear when the accommodation coefficient  $\alpha_i$  is reduced to 0.8 (Fig. 5.20e) and a flow with a larger mass flowrate, whose magnitude increases as  $\alpha_i$  decreases, is pumped from right to

left. The extreme cases are shown in Fig. 5.20c and Fig. 5.20f, considering a specular reflection on the vertical walls or on the inclined walls, respectively. Comparing the flows in Fig. 5.20, it can be seen that the surfaces with the smaller accommodation coefficients have a weaker effect in the competition between the flows generated by the inclined walls and the vertical walls. In the extreme cases, smooth flows are generated either by the vertical walls (Fig. 5.20f) or by the inclined walls (Fig. 5.20c), but in opposite directions. However, the flow observed in Fig. 5.20f ( $\alpha_v = 1; \alpha_l = 0$ ), generated by the vertical walls, is much stronger than the flow generated by the inclined wall in Fig. 5.20c ( $\alpha_v = 0; \alpha_l = 1$ ), as shown in Tables 5.6 and 5.7. It can be concluded that the flow patterns and the mass flowrates are very sensitive to the local accommodation coefficients.

**Table 5.6:** Mass flowrate [ $\times 10^{-12}$  kg/s] for different values of the accommodation coefficient  $\alpha_v$  and full accommodation on the inclined walls ( $\alpha_l = 1$ ).

	$\alpha_v = 1$	$\alpha_v = 0.9$	$\alpha_v = 0.8$	$\alpha_v = 0$
$\alpha_l = 1$	<b>2.18</b>	3.77	4.90	19.43

**Table 5.7:** Mass flowrate [ $\times 10^{-12}$  kg/s] for different values of the accommodation coefficient  $\alpha_l$  and full accommodation on the vertical walls ( $\alpha_v = 1$ ).

	$\alpha_l = 1$	$\alpha_l = 0.9$	$\alpha_l = 0.8$	$\alpha_l = 0$
$\alpha_v = 1$	<b>2.18</b>	-1.74	-6.08	-109.8

### 5.3.6. Influence of geometric parameters

#### Misalignment distance

The influence of the misalignment distance  $L_m$  is now studied. The height  $d$  of the ratchet and the gap  $h$  between the tips are kept constant but the minimum vertical distance  $h_0$  between the two inclined walls varies with  $L_m$ . Figure 5.21 presents the variations of the mass flowrate with the misalignment distance  $L_m$  and the corresponding data are provided in Table 5.8. It is observed that the worst pumping result is obtained for  $L_m = 1 \mu\text{m}$ , i.e. for  $L_m/L = 0.25$ , and that the strongest effect is obtained for  $L_m$  close to 3, i.e. for  $L_m/L$  in the range [0.6 - 0.9]. The curve in Fig. 5.21 is not symmetric due to the asymmetry of the ratchet, which induces a flow

with a preferential direction. Actually,  $L_m$  and  $h_0$  can be considered as the characteristic lengths controlling the thermal transpiration flow generated by the vertical and inclined walls, respectively. On the one hand, for small values of  $L_m$ , the flow generated by the vertical walls is strong and vortices are stretched, which strongly reduces the net flowrate in  $x$ -direction, as shown in Figs. 5.22a and 5.22b. On the other hand, for higher values of  $L_m$ , the vortices are more compact and the flow generated in  $x$ -direction is higher as illustrated by Figs. 5.22c and 5.22d. It is found that the maximal reached mass flowrate is 11 times larger than the minimal one. This dramatic increase is obtained by a simple translation of  $2.5 \mu\text{m}$  of one of the surfaces and only requires a heat flux increase of 1 %. In other words, controlling the relative position of one wall vis-à-vis the facing wall could be a smart way for a fine tuning of the pumping level.

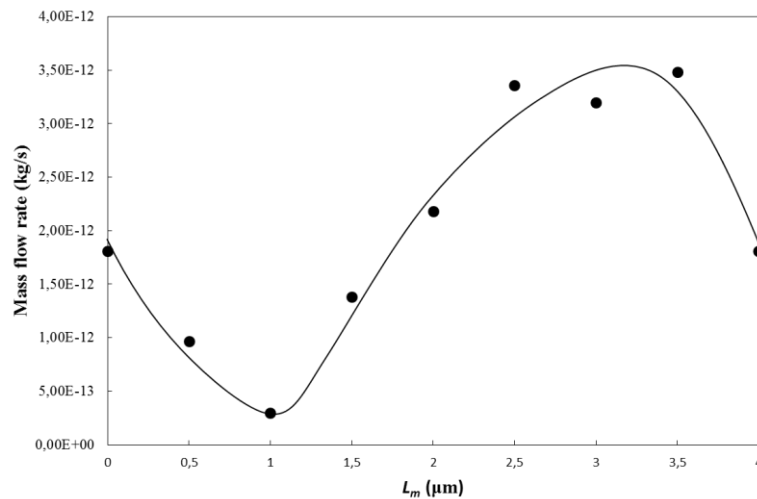
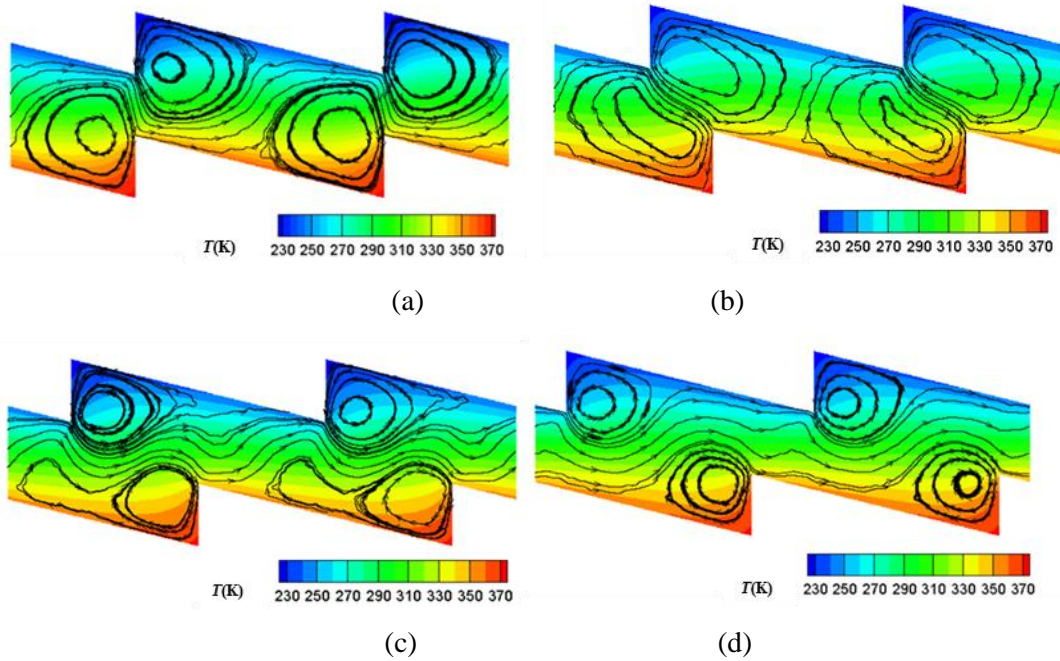


Figure 5.21: Mass flowrate versus misalignment distance  $L_m$  ;

$$Kn = 0.184, L = 1 \mu\text{m} \text{ and } d = h = 1 \mu\text{m}$$

Table 5.8: Mass flowrate ( $\times 10^{-12}$  kg/s) for different misalignment distances

$L_m$ ( $\mu\text{m}$ )	0/4	0.5	1	1.5	2	2.5	3	3.5
$h_0$ ( $\mu\text{m}$ )	1	1.875	1.75	1.625	1.5	1.375	1.25	1.125
Mass flowrate	1.81	0.97	0.30	1.38	2.18	3.38	3.20	3.48



**Figure 5.22: Temperature iso-contours and streamlines for different misalignment distances;  $Kn=0.184$ ,  $L=1\ \mu\text{m}$  and  $d=h=1\ \mu\text{m}$ .**

a)  $L_m = 0$ ; b)  $L_m = 1\ \mu\text{m}$ ; c)  $L_m = 2\ \mu\text{m}$ ; d)  $L_m = 3\ \mu\text{m}$

### Ratchet angle

The influence of the ratchet angle is now studied by varying the pattern length  $L$ , while keeping all other parameters at the reference conditions. Simulations are performed with a pattern length  $L$  varying from 1.0 to 6.0  $\mu\text{m}$ , which corresponds to an angle between  $38.7^\circ$  and  $80.5^\circ$ . Figure 5.23 presents the mass flowrate obtained for different ratchet angles in this range and Table 5.9 provides the precise data. An optimal angle corresponding to a maximal flowrate is found close to  $55^\circ$ , which is in good agreement with the optimal angle of  $60^\circ$  obtained from CFD simulations (Fig. 5.8). The decrease of the flowrate is significant when the angle departs from its optimal value.

**Table 5.9: Mass flowrate ( $\times 10^{-12}$  kg/s) for different values of the ratchet angle  $\beta$**

$L\ (\mu\text{m})$	0.6	0.8	1.0	1.2	1.6	2.0	3.0	4.0	5.0	6.0
$\beta\ (^\circ)$	31.0	38.7	45.0	50.2	58.0	63.4	71.6	76.0	78.7	80.5
$\dot{m}$	3.62	4.09	4.18	4.39	4.29	3.52	2.70	2.18	1.97	1.73

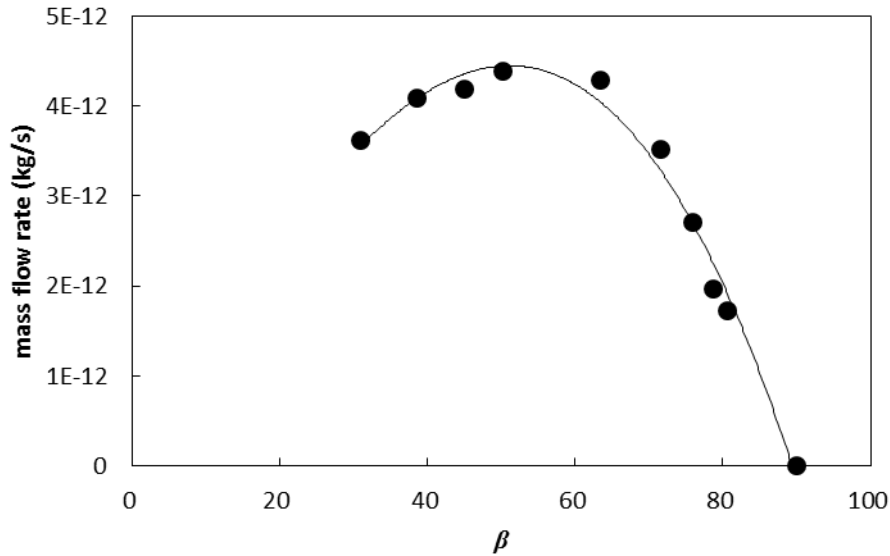
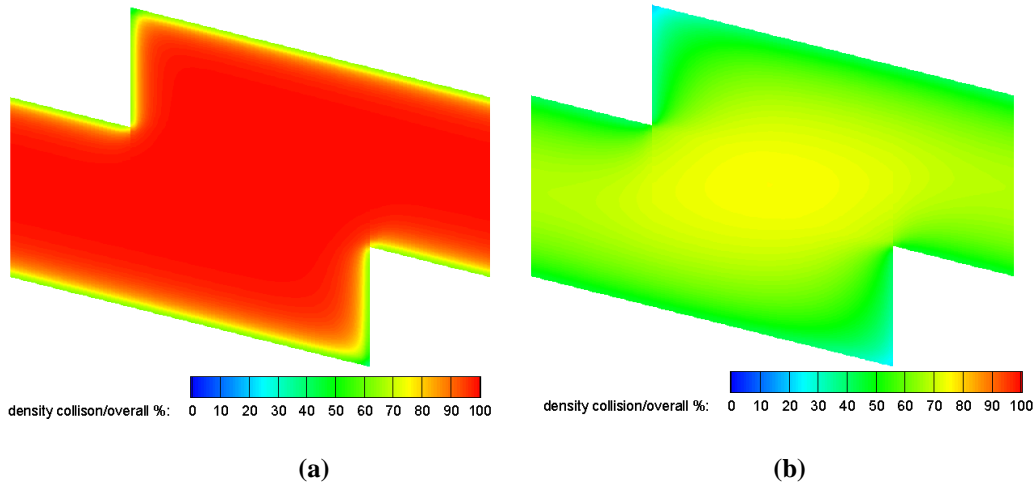


Figure 5.23: Mass flowrate for different values of the ratchet angle  $\beta$ .  $Kn = 0.184$ ,  
 $L = 1 \mu\text{m}$  and  $d = h = 1 \mu\text{m}$

### 5.3.7. Decomposition solution into ballistic and collision parts

The decomposition of the DSMC solution into the ballistic and collision parts as described in Chapter 2 is applied to analyze the thermal transpiration flow between two ratchet surfaces. The ballistic part is the result of the summation of molecules arriving from walls with no intermediate intermolecular collision while the molecules experiencing at least one intermolecular collision contribute to the collision part. Intuitively, the density ratio of the two parts can bring out the role played by the walls on the rarefied flow. Figure 5.24 presents the density fraction of the collision part to the overall density for two typical Knudsen numbers ( $Kn = 0.184$  and  $Kn = 1.840$ ) that correspond to the cases (a) and (d) in Fig. 5.19. For the smallest Knudsen number, the collision part density fraction has a lowest value of about 40 % near the walls and rapidly increases to 95 % across a layer of about  $0.3 \mu\text{m}$  thickness. For  $Kn = 1.840$  the lowest value of the collision part density fraction is about 25 % in the two corners of the ratchets surfaces where some molecules are probably blocked, colliding with the surfaces and thus increasing the density fraction of the ballistic part. The collision part density fraction gradually increases from the walls to reach about 75 % in the center of the channel. This shows that the whole domain is influenced by the walls in such rarefied conditions, while, for a lower rarefaction level, the collisions with walls will affect only a small layer of the flow.



**Figure 5.24: Density fraction of the collision part to overall density**

(a)  $Kn = 0.184$  (b)  $Kn = 1.840$

The streamlines and contours of velocity magnitude for the ballistic and collision parts are shown in Fig. 5.25. The streamlines of the ballistic and collision parts are completely different compared to the overall velocity field shown in Fig. 5.19, which is the summation of the two parts. For the largest Knudsen number,  $Kn = 1.840$ , the streamlines of the ballistic and collision parts have similar patterns but with velocities in opposite directions as shown in Figs. 5.25(b) and (d). The ballistic streamlines are directed from walls towards the channel center while the collision streamlines are directed from the channel center towards the walls. For both rarefaction levels, all streamlines of the ballistic part gather to a sink in the center of the channel while all streamlines of the collision part originate from a source in the same region. However, the patterns are very different for the two studied Knudsen numbers. For the lowest rarefaction level, the two singular points are not coincident, resulting in strongly dissymmetric flow patterns for both parts. Contrarily, for the highest Knudsen number, the patterns of the ballistic and collision parts are very similar, with a high degree of symmetry relative to the sink and source points which are apparently at the same position in the channel. In addition, one can note that in the case  $Kn = 0.184$ , the velocity magnitudes for the ballistic (Fig. 5.25a) and collision (Fig. 5.25c) parts of the flow are about one or two orders of magnitude higher than the overall velocity (Fig. 5.14). The maximal ballistic velocity is found near the hot wall where the collision velocity also reaches its maximum value.

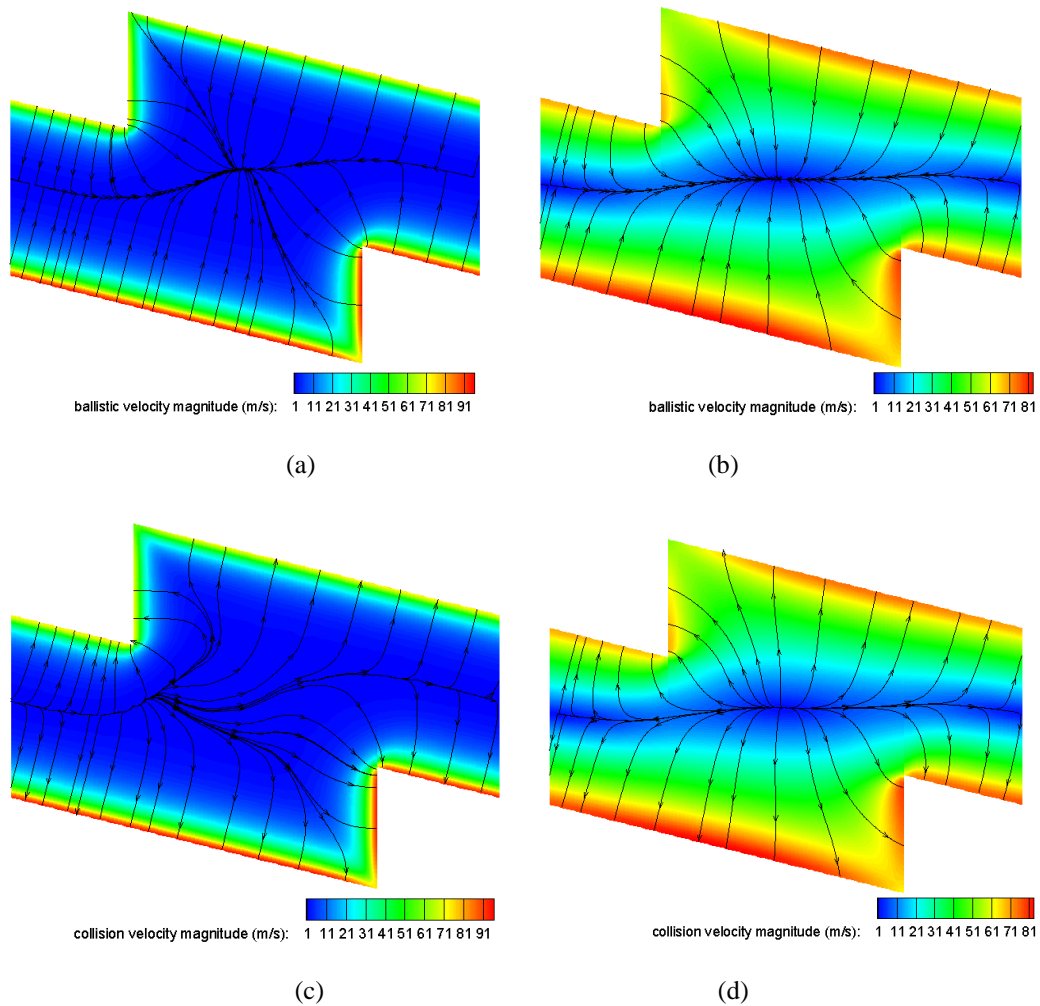


**Figure 5.25: Streamlines and contour of velocity magnitude;**

**a) ballistic part  $Kn = 0.184$  , b) ballistic part  $Kn = 1.84$  ,**

**c) collision part  $Kn = 0.184$  , d) collision part  $Kn = 1.84$**

## 5.4. Summary

In this chapter, a novel configuration of Knudsen pump, which only requires isothermal hot or cold walls and is consequently much easier to control than a classic pump with temperature gradient along a surface, has been investigated by CFD simulations based on a continuum approach and by DSMC calculations. The pumping element consists of two facing isothermal ratchet surfaces at different temperatures. A net mass flowrate generated by the asymmetric saw-tooth-like surfaces was observed and the operation of this new type Knudsen pump has been numerically proved. The influence of the main geometrical parameters and operating conditions, such as Knudsen number and temperature difference, has been studied and a rough guideline for designing a prototype has been drawn.

In particular, it has been shown that:

- The pumping is observed in the slip flow regime and can be simulated by the Navier-Stokes equations with appropriate velocity slip and temperature jump boundary conditions.
- The pump can work even when all surfaces are diffusive and does not require a specific pattern alternating specular and diffusive regions. However, the mass flowrate is very sensitive to the values of the accommodation coefficients, especially the accommodation coefficient of the inclined surfaces.
- A reasonable angle of curvature at the edges of the ratchet is compatible with the pumping phenomenon.
- The pumping is significant only if the distance between the walls remains small, typically of the same order of magnitude as the ratchet depth.
- For the studied configuration, a maximal mass flowrate is reached for a Knudsen number close to 0.07 and for higher rarefaction, the flowrate decreases rapidly as the Knudsen number increases. A net flow is generated in the opposite direction for  $Kn \in [1.0 ; 10]$ .
- The net flowrate and the local flow pattern also depend on the geometric design, such as ratchet angle and misalignment distance. The misalignment of the two ratchet patterns has a dramatic effect on the resulting flowrate. In addition, an optimal angle of the ratchet, close to  $60^\circ$ , allows a maximum flowrate.

However, all the simulations presented here are 2D. In practice, the material of the lateral walls and the assembly technology will have to be carefully considered in order to avoid a large conductive heat flux between the two micro-structured surfaces through the lateral walls. Additional 3D simulations taking into account conjugate heat transfer will be necessary to estimate the performance limitations of actual pump designs.

## References

- Bergoglio, M., Mari, D., Chen, J., et al. (2015). "Experimental and computational study of gas flow delivered by a rectangular microchannels leak." *Measurement* 73: 551-562.
- Donkov, A. A., Tiwari, S., Liang, T., et al. (2011). "Momentum and mass fluxes in a

- gas confined between periodically structured surfaces at different temperatures." *Physical Review E* 84(1): 016304.
- Hardt, S., Tiwari, S. and Baier, T. (2013). "Thermally driven flows between a Leidenfrost solid and a ratchet surface." *Physical Review E* 87(6): 063015.
- Kandlikar, S., Garimella, S., Li, D., et al. (2005). *Heat transfer and fluid flow in minichannels and microchannels*, Elsevier.
- Linke, H., Alemán, B. J., Melling, L. D., et al. (2006). "Self-Propelled Leidenfrost Droplets." *Physical Review Letters* 96(15): 154502.
- Mohammadzadeh, A., Rana, A. S. and Struchtrup, H. (2015). "Thermal stress vs. thermal transpiration: A competition in thermally driven cavity flows." *Physics of Fluids* 27(11): 112001.
- Ok, J., Lopez-Oña, E., Nikitopoulos, D., et al. (2011). "Propulsion of droplets on micro- and sub-micron ratchet surfaces in the Leidenfrost temperature regime." *Microfluidics and Nanofluidics* 10(5): 1045-1054.
- Rojas-Cárdenas, M., Graur, I., Perrier, P., et al. (2013). "Time-dependent experimental analysis of a thermal transpiration rarefied gas flow." *Physics of Fluids (1994-present)* 25(7): 072001.
- Sharipov, F. (2003). "Application of the Cercignani–Lampis scattering kernel to calculations of rarefied gas flows. II. Slip and jump coefficients." *European Journal of Mechanics - B/Fluids* 22(2): 133-143.
- Sone, Y. (2007). *Molecular Gas Dynamics, Theory, Techniques, and Applications*. Boston, USA, Birkhauser Boston.
- Würger, A. (2011). "Leidenfrost Gas Ratchets Driven by Thermal Creep." *Physical Review Letters* 107(16): 164502.



## Chapter 6

# Experimental study of thermal transpiration flow through a micro-tube

---

In this chapter, a new experimental set-up for investigating a thermal transpiration flow through a single micro-tube is presented. The experimental apparatus has been designed to be adaptable for investigating other configurations as well as Knudsen compressors. First, the experiment set-up is described in details. Then the experimental procedure is introduced. Finally, the experimental results are shown and discussed with comparison to theoretical data.

### **6.1. Description of the experiment set-up**

As shown in Fig. 6.1, the experimental set-up is composed of four main parts: (i) the test section, where the microsystem, such as a micro-tube or a Knudsen pump, can be connected; (ii) the measurement ring section, composed of two reservoirs coupled to capacitance diaphragm pressure gauges (CGA and CGB) and thermocouples (TA and TB); (iii) the temperature control system, consisting of a heater made of a constantan wire, a Peltier module and its controller, three thermocouples (T1, T2, T3) and a power supply; and (iv) the accessories section, composed of a turbomolecular pump, supply gas tanks and the acquisition system.

One of the most important features of this set-up is that the tested microsystems are easily interchangeable. In order to implement this feature, several general interfaces were designed for connecting a micro-tube/channel or a Knudsen pump. Each element in the system is connected to other neighbor elements by standard ISO KF16 flanges as shown in Fig. 6.2a. Besides, several parts of the set-up are also adjustable, in particular with the aim of reducing or increasing the volume of system. Moreover, the independent and miniaturized temperature control system can provide desired local temperatures at any place on the microsystem.

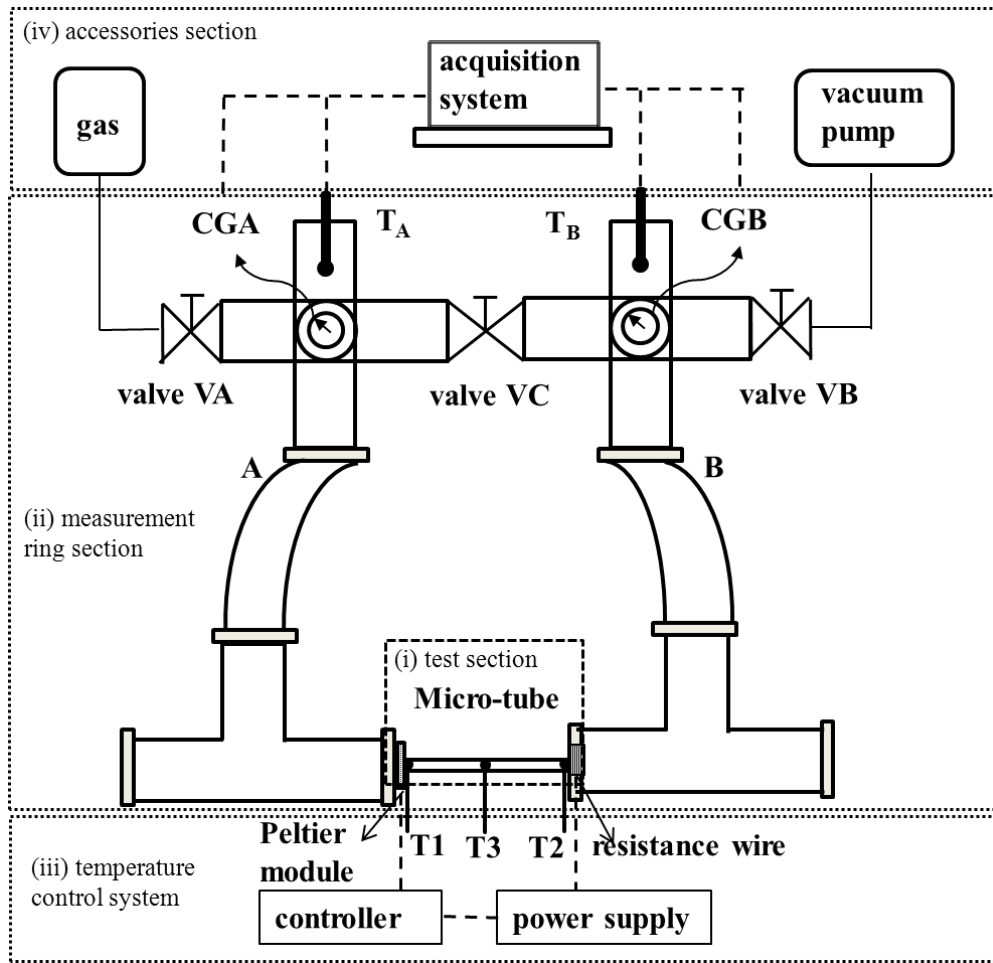


Figure 6.1: Schematic diagram of the experimental set-up

### 6.1.1. Test section

In the present study, a glass micro-tube is connected as shown in Fig. 6.1. The micro-tube is glued to KF16 socket flanges by a special glue (see Fig. 6.2a). The low outgassing of the glue compounds was approved by NASA and it could work under a wide temperature range of 0-400°C. The glue has a high thermal conductivity which can efficiently reduce the possible non-uniform temperature distribution in the ends of the micro-tube placed inside the flanges, which extend beyond the region of interest where the temperature gradient should be controlled, and in which parasite thermal transpiration must be avoided.

The diameter of the tube is measured by an optical 3D Alicona InfiniteFocus Measurement System. Figure 6.2b shows a photo of one end of the tube. Diameters at both sides have been measured and the values are  $503.14 \pm 2.04 \mu\text{m}$  and

$504.80 \pm 1.80 \mu\text{m}$ . The average value  $D = 503.79 \mu\text{m}$  is used in the following analysis. The effective length where the temperature gradient is imposed is  $L = 52.01 \text{ mm}$ .



Figure 6.2: (a) Glass microtube glued to KF16 socket flanges;  
(b) Photo taken by the Alicona System for the measurement of the inner diameter

### 6.1.2. Measurement ring

The measurement ring section consists of two reservoirs, two pressure gauges (CGA and CGB), two thermocouples (TA and TB) and three valves VA, VB and VC. Each so-called reservoir includes a T-junction, a flexible tube and a 5-way cross, all parts being in stainless steel (see Fig. 6.3).

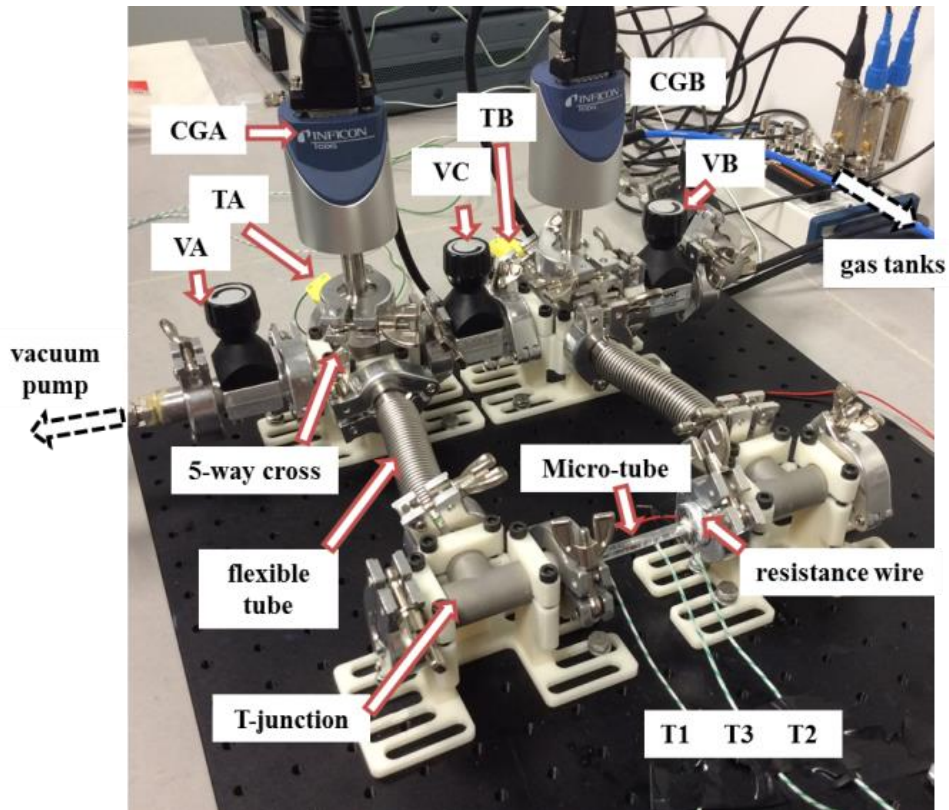


Figure 6.3: Photo of the experimental set-up

The whole circuit can be outgassed using an Oerlikon Turbolab80 turbomolecular vacuum pump, and can be supplied with gas from a high-pressure tank, via valves VB and VA. The steps of vacuum-pumping and gas-filling are repeated several times in order to be sure that the gas remaining inside the set-up is only the operating gas. After the pressure is set to the desired value, valves VA and VB are kept closed during the whole test. Valve VC between the two reservoirs plays an important role in the experiments of thermal transpiration flow. Its main role is to balance the pressures in both reservoirs at the beginning of the test keeping it open and to launch the measurement process at the time it is closed.

#### Pressure measurement

The variations of pressure in both reservoirs are monitored by two Inficon capacitance gauges which are connected to the top of the reservoirs and placed in a vertical position. The full scale of the pressure gauges is 1333.32 Pa, the resolution is 0.015 % of the full scale and the precision is 0.2 % of the reading. Their ideal operating temperature is 25 °C. In the present set-up, there is only a small area near the hot side of the tube kept at a relative high temperature; thus, the temperature of both reservoirs can be considered close to the ambient temperature of 295 K, which is also close to the ideal operating temperature of the pressure gauges. This configuration should avoid any possible parasite thermal transpiration flow inside the gauges fittings.

#### Volumes of the reservoirs

The volumes  $V_1$  and  $V_2$  of the reservoirs are measured by a simple method based on the thermodynamic equilibrium process introduced in (Rojas-Cárdenas 2012). Two stages are performed, during which the whole system is kept at the ambient temperature. In the first stage, different pressures ( $P_A$ ,  $P_B$ ) are initially set for the two reservoirs with valve VC closed. Then valve VC is opened and a final thermodynamic equilibrium state is achieved when an equal pressure  $P_e$  is measured in both reservoirs. Considering the mass conservation law, the following equation can be obtained:

$$P_A V_A + P_B V_B = P_e (V_A + V_B). \quad (6.1)$$

The second stage is similarly performed based on the thermodynamic equilibrium between reservoir B and reservoir A, the latter being connected to a standard tank with a known volume  $V_{ref}$ . The relationship which links the initial pressures ( $P'_A$ ,  $P'_B$ ) to the final equilibrium pressure  $P'_e$  is then:

$$P'_A(V_A + V_{ref}) + P'_B V_B = P'_e(V_A + V_B + V_{ref}). \quad (6.2)$$

The volume  $V_{ref} = 486.47 \pm 0.25 \text{ cm}^3$  of the reference tank is measured by comparing the weight of the empty tank with the weight of the tank filled by water. Combining Eqs. (6.1) and (6.2), the volumes  $V_A = 117.30 \pm 2 \text{ cm}^3$  and  $V_B = 115.92 \pm 2 \text{ cm}^3$  are deduced. In the present experiments,  $V_B$  is the volume of the reservoir connected to the hot side of the tube.

#### Valve between the two reservoirs

As previously mentioned, the valve between the two reservoirs is open at the beginning of the experiments in order to keep the balance of pressures in both reservoirs and then it is closed to measure the pressure variation in both reservoirs due to the thermal transpiration flow. At the time when valve VC is closed, the volume of the ring can be changed a bit due to a small volume difference inside the valve between its open and closed states. If this volume is not negligible, the valve inevitably compresses the gas when it is closed. In the present set-up, no compressible effect was captured by the pressure gauges when the working pressure was below 200 Pa and an increase of about 0.2 Pa was measured for an operating pressure of 500 Pa.

### **6.1.3. Temperature control and measurements**

#### Heating and cooling

The heating resistance is a constantan wire coiled around the KF16 socket flange at one end of the tube. The heating temperature can be controlled by a fine tuning of the current intensity through the wire. A copper block equipped with two Peltier modules can be directly put on the other side of the glass tube when cooling is needed. The Peltier modules are controlled by a power unit connected to a temperature sensor. Therefore the temperatures of cold and hot sides of the tube can be accurately controlled and they are measured by two thermocouples. Besides, the resistance wire as well as the Peltier modules are removable and the heating/cooling areas are small

(the diameter of the resistance wire is 0.1 mm and the area of the Peltier modules is  $1.2 \times 1.3 \text{ cm}^2$ ). The aim of these independent and local temperature control systems is to provide desired temperatures at any point of various microsystems. In our first experiments, one side of the tube is heated to  $T_h = 337.65 \text{ K}$  while the other side is just cooled by the ambient air at  $T_c = 295.65 \text{ K}$ .

*Temperature along the channel*

The temperature distribution along the channel is obtained by a theoretical model and experimental data provided by three thermocouples (T1, T2, T3 in Fig. 6.1) put at the two ends and in the middle of the micro-tube.

The two ends of the tube are kept at constant temperatures  $T_c$  and  $T_h$ . The temperature distribution  $T(z)$  along the tube depends on the material thermal properties and on heat losses from the tube to the environment. This problem can be simplified and described by the heat diffusion equation, considering 1-D conduction as a first approach:

$$\frac{d^2 T}{dz^2} + \frac{\dot{\Phi}}{\lambda_g} = 0 \quad (6.3)$$

where  $z$  is the tube axis direction,  $\lambda_g$  the thermal conductivity of the glass and  $\dot{\Phi}$  is a source term, which can be related to the heat rate  $\Phi_s$  leaving the surface of the tube as

$$\dot{\Phi} = -\frac{\Phi_s}{Sdz} = -\frac{hp_s(T - T_b)}{S} \quad (6.4)$$

where  $S$  is the cross-sectional area,  $p_s$  is the perimeter of the tube,  $h$  is the average heat transfer coefficient and  $T_b$  is the ambient temperature. Inner convection is neglected compared with outer convection, due to a much lower inner gas density and a much lower exchange surface area, as the tube is thick. Therefore the temperature distribution along the tube can be obtained as

$$T(z) = T_b + \frac{e^{CL}(T_h - T_b) - (T_c - T_b)}{e^{2CL} - 1} e^{Cz} + \frac{e^{2CL}(T_c - T_b) - e^{CL}(T_h - T_b)}{e^{2CL} - 1} e^{-Cz} \quad (6.5)$$

with  $C = \sqrt{hp_s / \lambda_g S}$ . It is found that the temperature distribution is not a linear nor a simple exponential function. Comparing the results from this simplified model with experimental values obtained by infrared camera imaging by Rojas-Cardenas in a similar configuration (Rojas-Cárdenas 2012), a good agreement is found for various temperature differences (see Fig. 6.4). The average heat transfer coefficient  $h$  for which a good fitting is found is  $15 \text{ W m}^{-2} \text{ K}^{-1}$ , which is a reasonable value.

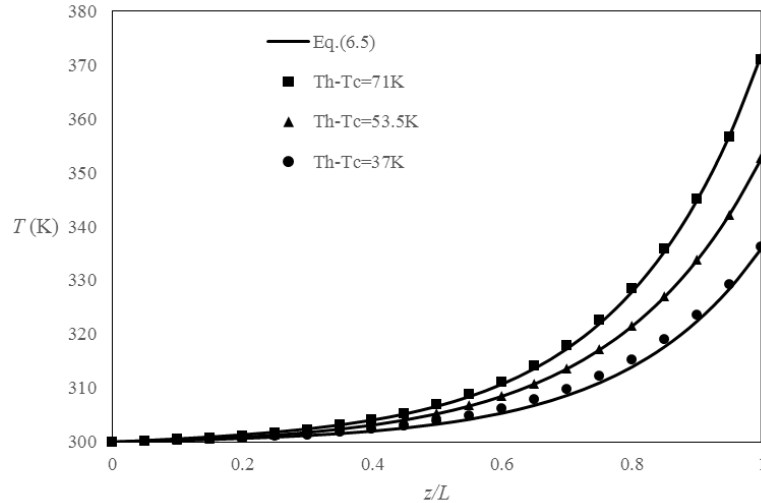


**Figure 6.4:** Temperature distributions along the channel obtained by the theoretical model compared with the experimental data from (Rojas-Cárdenas 2012)

In the experiments, the temperature distribution can be theoretically obtained by measuring the temperature of three points, at  $z=0$ ,  $z=L$  and  $z=z_3$ . The third point is used to fit the value of the average heat transfer coefficient  $h$ . The two thermocouples are fixed on the hot and cold sides of the tube and the third one is put in the middle of the tube, at  $z_3 = L/2$ . Figure 6.5 shows the temperature distribution calculated in the present experiments. The thermal conductivity of the glass tube is  $\lambda_g = 1.14 \text{ W m}^{-1} \text{ K}^{-1}$  and the deduced average heat transfer coefficient is  $h = 4.6 \text{ W m}^{-2} \text{ K}^{-1}$ . A smaller heat transfer coefficient  $h$  can be achieved by covering the glass tube with thermal insulation layers and the temperature distribution can then become closer to a linear one (see Fig. 6.5). On the other hand, the thermal insulation layers are also helpful to improve the efficiency of heating/cooling when the temperatures are far from the ambient temperature  $T_b$ .

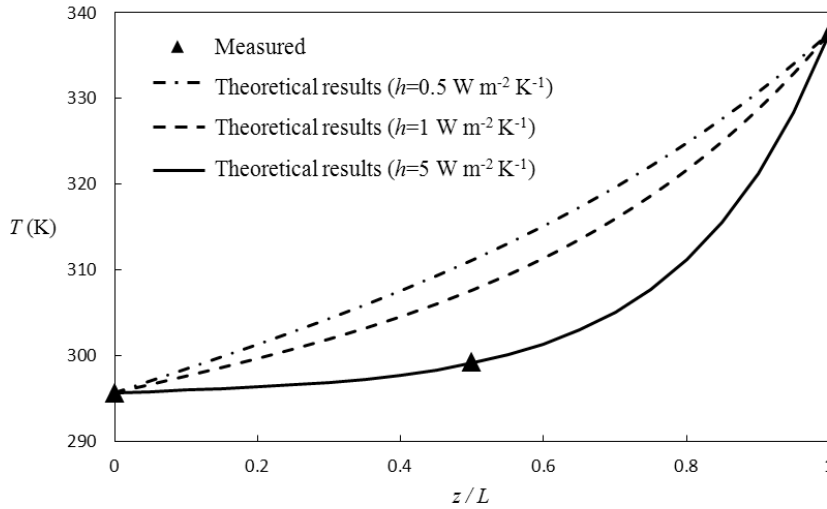


Figure 6.5: Temperature distribution along the tube obtained in present experiments

Temperature inside the reservoirs

The temperatures inside the two reservoirs are monitored by the two type K thermocouples TA and TB. Each thermocouple provides a measurement inside the reservoir by using a thermocouple feedthrough, as shown Fig. 6.6, which can be connected directly to reservoirs with the flange ISO KF16.

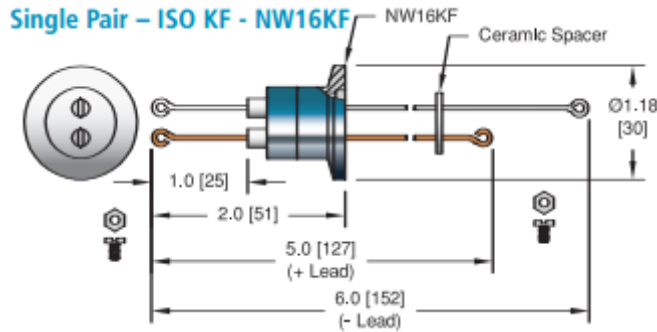


Figure 6.6: Thermocouple feedthrough

During the test, the temperatures of both reservoirs are kept constant at  $T = 297\text{ K}$ , which is slightly higher than the ambient temperature of  $T_b = 295.65\text{ K}$ . As shown in Figs. 6.1 and 6.3, a small zone near one side of the tube is heated and the neighboring T-junction is also at a relative high temperature due to conduction, but the flexible bellow connection between the T-junction and the cross-reservoir is long, which favors convective heat losses. Estimated by Eq. (6.5), the temperature difference

$T - T_b$  can decrease of about 90 % along the flexible tube. Therefore, the temperature near the pressure gauges is very close to the ambient temperature.

## 6.2. Measurement procedure

The measurement procedure includes the following steps:

1) In order to limit outgassing, the system is usually vacuumed for a long time (up to several days if the setup has been previously opened to atmosphere) with the heater activated. Several steps of vacuum-pumping and gas-filling should be combined to wash the inner surfaces. A minimum time pumping of 6 hours is performed before each test and the heater is continuously activated during a series of tests.

2) The desired pressure is set in the whole system. A certain period is required to reach thermal equilibrium in the system, during which valves VA and VB are closed and valve VC is open. During this period, a thermal transpiration flow takes place in the microtube from cold side to hot side but the pressures in both reservoirs are kept equal thanks to the open valve VC.

3) Leakage is quantified. The effect of leakage (combined to outgassing) cannot be neglected in this system. After reaching a thermal equilibrium state in the system, the pressures increase with a constant speed and the increasing rate is measured. It is noted that valve VC remains open during this step, and consequently the leakage rate measured in both reservoirs is the same. There is no good method to separately quantify the leakages in the cold and hot sides. We assume that they are equal and use the same value to correct the measured pressure variation in the following process. The leakage rate in the present experiments is of the order of  $8 \times 10^{-4} \text{ Pa/s}$ .

4) The measurement of thermal transpiration flow is launched by closing valve VC. The pressures in both reservoirs start to vary and a typical example of pressure variations is shown in Fig. 6.7. The pressure variation due to the leakage in Step 3 is subtracted from the measured values. Before closing of valve VC (for  $t < 0$ ), the pressures in both reservoirs are equal to  $P_0$  and the reference Knudsen number in the tube is defined at this pressure as

$$Kn_0 = \frac{k_2 \mu(T_0) \sqrt{RT_0}}{P_0 D}, \quad (6.6)$$

where  $T_0$  is the mean temperature and  $k_2$  is calculated based on the VHS model (see Table 2.1).

From  $t = 0$ , the pressure in the hot side reservoir increases whereas it decreases in the cold side reservoir. The pressures in cold and hot sides finally reach a stable value  $P_{cf}$  or  $P_{hf}$  and a pressure difference is generated. This pressure difference is the so-called thermomolecular pressure difference  $TPD = P_{hf} - P_{cf}$ .

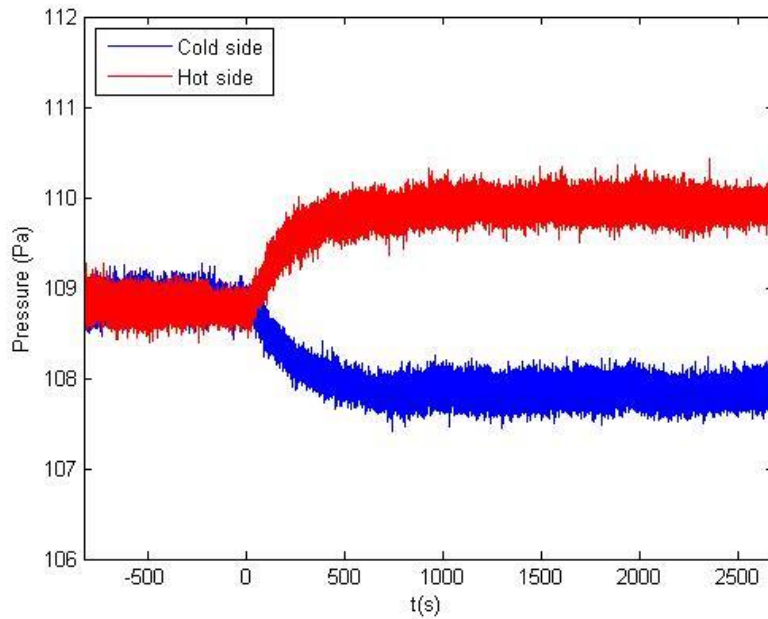


Figure 6.7: Typical example of pressure variations in the two reservoirs.

### 6.3. Results and discussion

#### 6.3.1. Final equilibrium state

The generated thermomolecular pressure difference is the most important parameter to characterize the final equilibrium state. Figure 6.8 shows the variations of  $TPD$  with the rarefaction parameter. The results obtained by (Rojas-Cárdenas 2012) are also presented in Fig. 6.8 as a comparison. In their work, a glass tube ( $L = 52.7 \pm 0.1$  mm,  $D = 485 \pm 6$   $\mu$ m) was connected between a hot reservoir and a cold reservoir. It is found that a maximal value of  $TPD$  is achieved at  $Kn_0 = 0.108$  for the present experiments. Moreover, the present results obtained for  $\Delta T = 42$  K

present the same trend than the experimental data (Rojas-Cárdenas 2012), and are well situated in-between their two curves obtained for  $\Delta T = 37\text{ K}$  and  $\Delta T = 53.5\text{ K}$ .

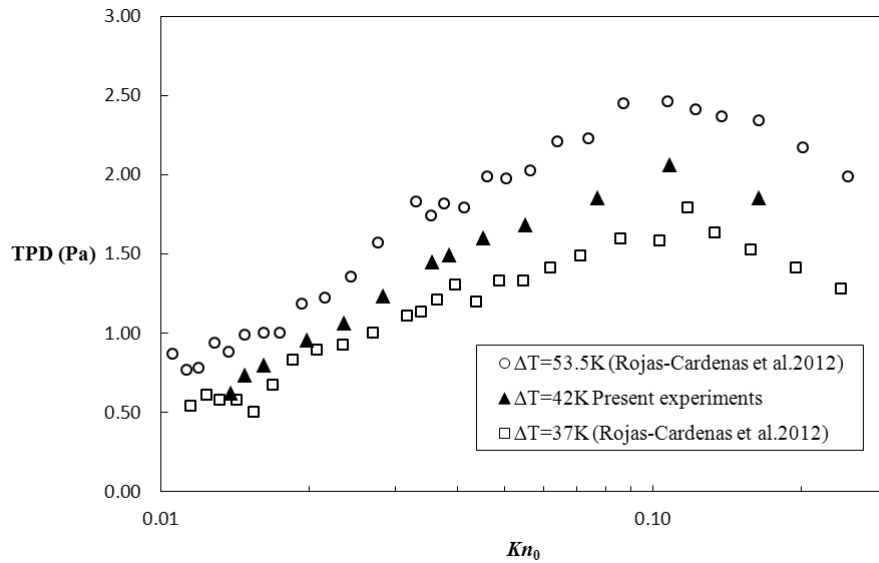


**Figure 6.8: Thermomolecular pressure difference obtained in present experiments compared with data from (Rojas-Cárdenas 2012)**

The experimental data obtained in the slip flow regime are compared with the analytical model presented in Section 2.2.2 (see Fig. 6.9). In the analytical model, it is necessary to give the viscous slip coefficient  $\sigma_p$  and the thermal slip coefficient  $\sigma_T$  and they are assumed to be, respectively, equal to 1.018 and 1.175, following the recommendations from Sharipov (Sharipov 2003).

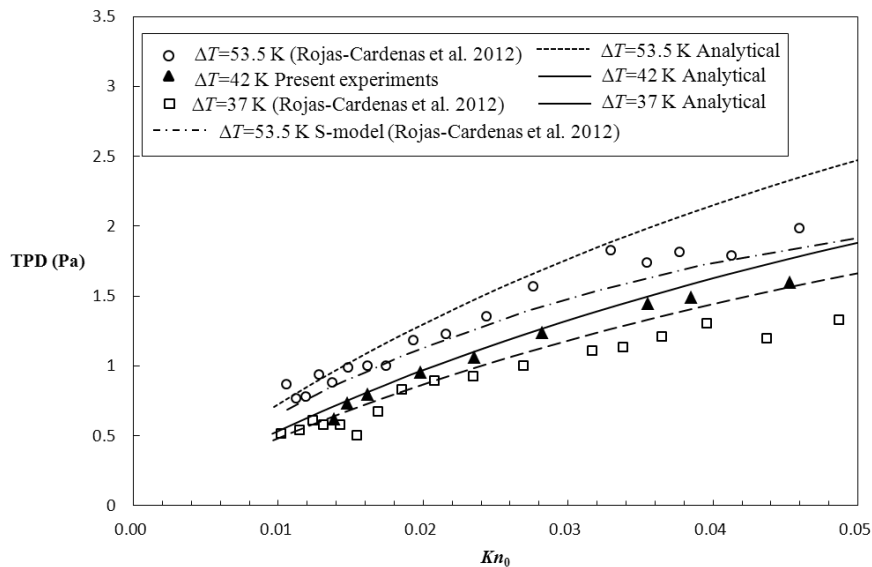


**Figure 6.9: Thermomolecular pressure difference in the slip flow regime compared with analytical and numerical results.**

The analytical model correctly predicts the variations of  $TPD$  and the values are slightly higher than the experimental data for all temperature differences  $\Delta T$  and higher than the kinetic results based on the S-model as well. However, the deviations between experimental data and analytical results are relatively small.

Furthermore, the analytical results depends on the viscous slip coefficient  $\sigma_p$  and on the thermal slip coefficient  $\sigma_T$ . In the present case, the influence of the viscous slip coefficient  $\sigma_p$  on the generated pressure difference is weak, e.g.  $TPD$  increases of 2.6 % when  $\sigma_p$  changes from 1.108 to 1.0 in the case  $Kn_0 = 0.108$ . If the viscous slip coefficient  $\sigma_p$  is set to zero,  $TPD$  only increases of 35 %. The real viscous slip coefficient  $\sigma_p$  and thermal slip coefficient  $\sigma_T$  for a given micro-tube and working gas can be extracted from experiments (Graur et al. 2009, Rojas-Cárdenas et al. 2015).

### 6.3.2. Analysis of the unsteady pressure variation process

In order to study the unsteady pressure variation process, a simplified theoretical model in the slip flow regime is presented here. We consider a micro-tube which is connected to two reservoirs at different temperatures. The mass flowrate through the tube of radius  $a$  can be calculated by Eq (2.24). Assuming as a first approximation that the pressure and temperature distributions along the tube are linear (we know it is not the case, but the linearization allows a simpler model which is finally rather accurate), Eq. (2.24) can be simplified as:

$$\dot{m}_h = -\frac{\pi a^4 \rho_0}{8\mu_0} \left(1 + 4\sigma_p \frac{\lambda_e}{a}\right) \frac{P_h - P_c}{L} + \sigma_T \frac{\mu_0 \pi a^2}{T_0} \frac{T_h - T_c}{L} \quad (6.7)$$

where the physical properties of the gas in the system are evaluated at the average temperature  $T_0$  and initial pressure  $P_0$  and  $\lambda_e$ ,  $\sigma_p$  and  $\sigma_T$  are defined in Section 2.2.1. For sake of simplicity, Eq.(6.7) is rewritten as:

$$\frac{dm_h}{dt} = \dot{m}_h = -C_1(P_h - P_c) + C_2, \quad (6.8)$$

where

$$C_1 = \frac{\pi a^4 \rho_0}{8\mu_0 L} \left(1 + 4\sigma_p \frac{\lambda_e}{a}\right), \quad (6.9)$$

$$C_2 = \sigma_T \frac{\mu_0 \pi a^2}{T_0} \frac{T_h - T_c}{L}. \quad (6.10)$$

The ideal gas equation of state can be written in the reservoir connected to the hot side (with subscript  $h$ ) as well as in the reservoir connected to the cold side (with subscript  $c$ ) in the form

$$P_h = \frac{m_h}{V_h} RT_h, \quad P_c = \frac{m_c}{V_c} RT_c, \quad (6.11)$$

where  $V_c$  and  $V_h$  are the volume of the reservoirs, and  $m_c$  and  $m_h$  are the mass of gas inside these reservoirs. Considering that the whole system is closed, the total mass  $m = m_c + m_h$  is constant and the following equation can be derived from Eq. (6.8):

$$\frac{dm_h}{dt} = -C_1 m_h R \left( \frac{T_h}{V_h} + \frac{T_c}{V_c} \right) + C_1 \frac{m RT_c}{V_c} + C_2. \quad (6.12)$$

Integrating Eq. (6.12), we can obtain

$$m_h = \exp \left( \ln C_3 - C_1 \left( \frac{RT_h}{V_h} + \frac{RT_c}{V_c} \right) t \right) + C_4, \quad (6.13)$$

where

$$C_4 = \frac{m RT_c}{V_c \left( \frac{RT_h}{V_h} + \frac{RT_c}{V_c} \right)} - \frac{C_2}{-C_1 \left( \frac{RT_h}{V_h} + \frac{RT_c}{V_c} \right)} = m_h \Big|_{t \rightarrow \infty} \quad (6.14)$$

and

$$C_3 = m_h \Big|_{t=0} - C_4 = m_h \Big|_{t=0} - m_h \Big|_{t \rightarrow \infty}. \quad (6.15)$$

The pressures in the reservoirs can then be calculated as:

$$\begin{aligned} P_h(t) &= \frac{m_h}{V_h} RT_h = \exp \left( \ln \frac{C_3 RT_h}{V_h} - C_1 \left( \frac{RT_h}{V_h} + \frac{RT_c}{V_c} \right) t \right) + \frac{C_4 RT_h}{V_h} \\ &= (P_{hf} - P_0) \left( 1 - \exp \left( -C_1 \left( \frac{RT_h}{V_h} + \frac{RT_c}{V_c} \right) t \right) \right) + P_0 \end{aligned} \quad (6.16)$$

$$\begin{aligned} P_c(t) &= \frac{m - m_h}{V_c} RT_c = -\exp \left( \ln \frac{C_3 RT_c}{V_c} - C_1 \left( \frac{RT_h}{V_h} + \frac{RT_c}{V_c} \right) t \right) + \frac{m - C_4}{V_c} RT_c \\ &= (P_{cf} - P_0) \left( 1 - \exp \left( -C_1 \left( \frac{RT_h}{V_h} + \frac{RT_c}{V_c} \right) t \right) \right) + P_0 \end{aligned} \quad (6.17)$$

where  $P_0 = (C_3 + C_4)RT_h/V_h$ ,  $P_{cf} = (m - C_4)RT_c/V_c$  and  $P_{hf} = C_4RT_h/V_h$ .

The above equations can help to analyze the following behaviors observed in the experiments:

1) For high values of  $t$ , the pressures in the two reservoirs tend to a constant value:  $P_{hf}$  in the hot-side reservoir and  $P_{cf}$  in the cold-side reservoir.

2) Introducing the characteristic time  $\tau$  defined as

$$\tau = \frac{1}{C_1 \left( \frac{RT_h}{V_h} + \frac{RT_c}{V_c} \right)}, \quad (6.18)$$

Eq. (6.16) can be rewritten as

$$\frac{P_h(t) - P_0}{P_{hf} - P_0} = 1 - e^{-t/\tau}. \quad (6.19)$$

At  $t = \tau$ , the pressure difference  $P_h(t) - P_0$  is at 63.2 % of the final pressure difference  $P_{hf} - P_0$ . At  $t = -\ln(0.005)\tau$ , this pressure difference reaches 99.5 % of its final value. For the case shown in Fig. 6.7, it is the case for  $t = 1117\text{s}$ , which is confirmed by Fig. 6.7. In the same way, Eq. (6.17) can be written as

$$\frac{P_c(t) - P_0}{P_{cf} - P_0} = 1 - e^{-t/\tau} \quad (6.20)$$

With the same characteristic  $\tau$  defined by Eq. (6.18).

Similarly, the experimental pressure variations in the cold-side and hot-side reservoirs were fitted by Rojas-Cardenas et al. (Rojas-Cárdenas et al. 2013) by exponential functions as follows:

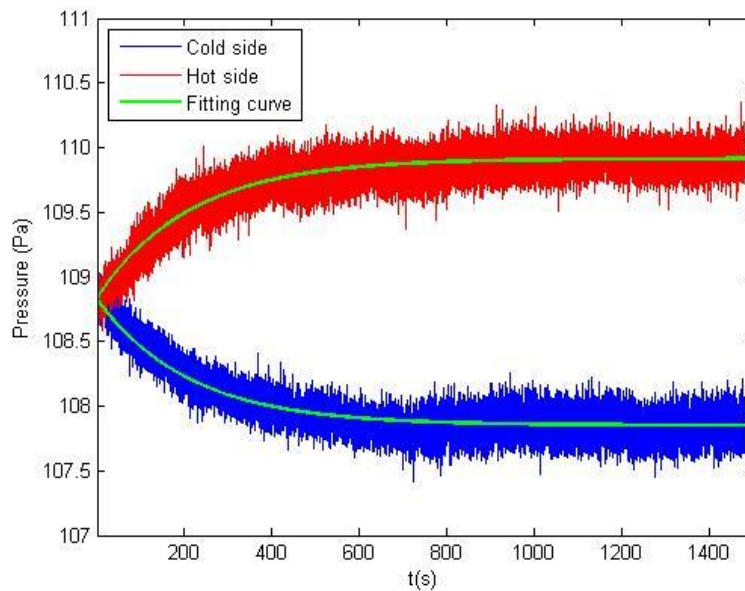
$$P_c(t) = P_0 + (P_{cf} - P_0) \left( 1 - e^{-t/\tau_f} \right), \quad (6.21)$$

$$P_h(t) = P_0 + (P_{hf} - P_0) \left( 1 - e^{-t/\tau_c} \right). \quad (6.22)$$

Coefficients  $\tau_f$  and  $\tau_c$  were two different parameters obtained by experimental fitting, made for several tests. The fitted Eqs. (6.21) and (6.22) proposed by (Rojas-Cárdenas et al. 2013) are in perfect agreement with the theoretical Eqs. (6.19) and (6.20) proposed above, which show that the characteristic time should be the same in both reservoirs. Although Rojas-Cardenas did not propose any theoretical formulation

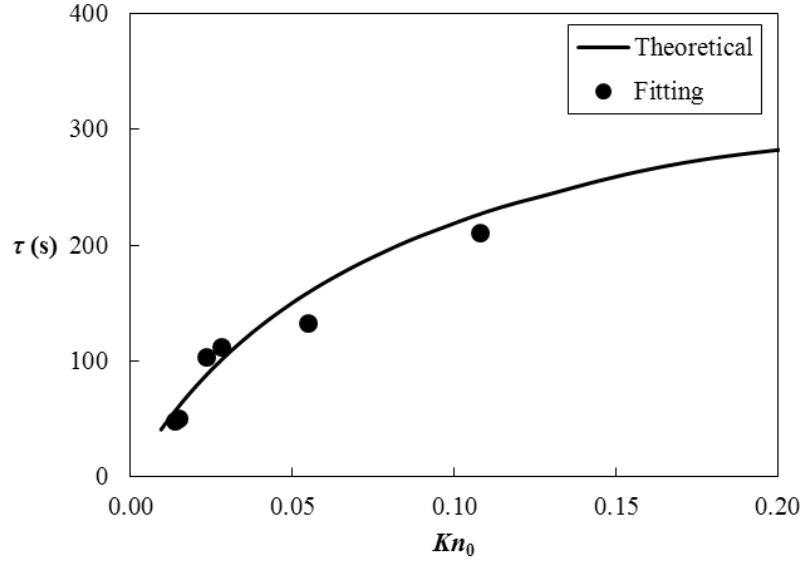
of the coefficients  $\tau_f$  and  $\tau_c$ , he demonstrated from the conservation of mass, that they should be identical, which is confirmed by the present model.

Figure 6.10 shows the experimental pressure variations compared with the data from Eqs. (6.21) and (6.22), i.e. with a fitted value  $\tau_{exp}$  of the coefficients  $\tau_f$  and  $\tau_c$ , as made in the work of Rojas-Cardenas et al., for initial conditions such as  $Kn_0 = 0.108$ . The theoretical value of  $\tau = 223.93$  s calculated by Eq. (6.18) is close to this fitted value  $\tau_{exp} = 210.75$  s, but both are larger than the characteristic time obtained by fitting by (Rojas-Cárdenas et al. 2013) in their own experiments, due to larger volumes of reservoirs in the present experimental set-up.



**Figure 6.10: Experimental pressure variations from  $t = 0$  to final equilibrium, compared with Eqs. (6.21) and (6.22)**

Figure 6.11 compares the theoretical –given by Eq. (6.18)– and fitted –obtained from experimental data and Eq. (6.19)– values of the characteristic time  $\tau$ . It is found that the theoretical characteristic time is in good agreement with the experimentally fitted value. For example, in the case  $Kn_0 = 0.028$ , the characteristic time calculated by Eq. (6.18) is  $\tau = 103$  s and the value extracted from exponential fitting of the experimental data is  $\tau_{exp} = 112$  s.



**Figure 6.11: Characteristic time obtained by the theoretical model and by fitting of experiment data.**

However, it should be noted that the characteristic time obtained by fitting is sensible to the range of data, especially in the slip flow regime. For small  $Kn_0$ , the pressure difference  $P_{hf} - P_0$  is small, typically in the range 0.39 to 0.82 Pa, compared to the absolute pressure  $P_0 = 416.4 \sim 848.3$  Pa, and the precision of the pressure gauges is 0.2 % of reading. As a consequence, the accuracy of fitting is strongly influenced by the fluctuations of the pressure signal.

3) The theoretical pressure versus time relationship is linear in a logarithmic plot, since

$$\ln(P_h - P_{hf}) = -C_1 \left( \frac{RT_h}{V_h} + \frac{RT_c}{V_c} \right) t + \frac{C_3 RT_h}{V_h} \quad (6.23)$$

The slope of the straight line is only associated with the viscous slip coefficient  $\sigma_p$ , via coefficient  $C_1$ , and the intercept at  $t = 0$  is associated with the initial conditions, the viscous slip coefficient and the thermal slip coefficient  $\sigma_T$ . The comparison of theoretical predictions of experimental results is shown in Fig. 6.12. It is observed that theoretical predictions are closely confirmed by experimental data.

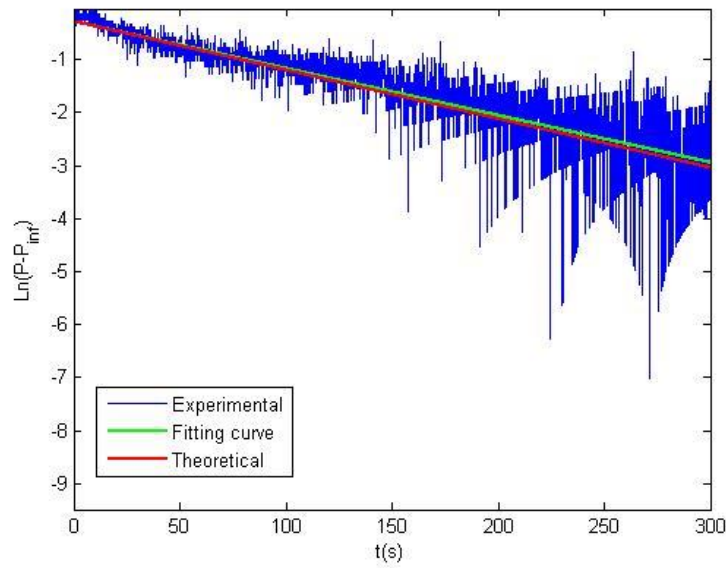
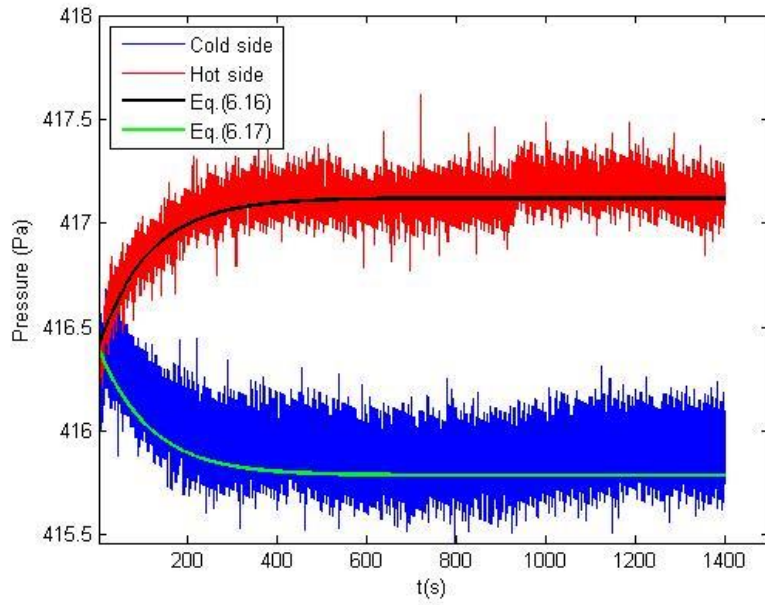


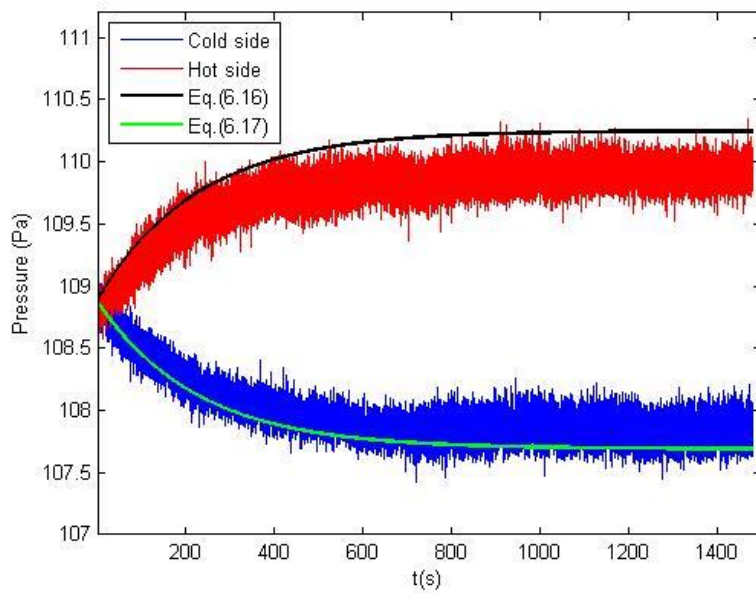
**Figure 6.12: Logarithmic pressure variation  $\ln(P_h - P_{hf})$  in the hot-side reservoir versus time**

4) The unsteady pressure variation process can be described by Eqs. (6.16) and (6.17). Figure 3.13 shows the experimental pressure variations compared with the data from (6.16) and (6.17) for  $Kn_0 = 0.108$  and  $Kn_0 = 0.028$ .

It is found that the theoretical results (without any experimental fitting) predict rather accurately the pressure versus time evolution, especially for the small Knudsen numbers (Fig. 6.13a). For higher values of the Knudsen number, the deviation with the experimental data is increased (Fig. 6.13b). This deviation is due to the limits of applicability of 1<sup>st</sup> order slip boundary conditions and may also partly result from the simplifying assumptions (mainly the linear temperature distribution hypothesis) of the theoretical model, .



(a)



(b)

**Figure 6.13: Experimental pressure variations from  $t = 0$  to final equilibrium, compared with theoretical results of Eqs. (6.16) and (6.17).  $Kn_0 = 0.028$  (a);  $Kn_0 = 0.108$  (b)**

#### 6.4. Summary

In this chapter, a new experimental set-up for investigating the thermal transpiration flow through a single micro-tube has been presented and the experimental data have been compared for small Knudsen numbers to theoretical model, assuming a slip flow regime. The experimental apparatus has been designed to be able to test other kinds of microchannels as well as Knudsen compressors.

The analytical model correctly predicts the variations of *TPD* and the calculated values are slightly higher than experimental results for all investigated temperature differences  $\Delta T$  as well as than kinetic results based on the S-model.

An analysis of the unsteady pressure variation process has shown that a simple theoretical analysis, based on the assumption of slip flow regime and linear temperature gradient along the tube walls, can accurately correlate experimental data.

In the near future, micro-tubes with different diameters and under various operating conditions and gas species will be analyzed by the experimental set-up.

#### References

- Graur, I., Perrier, P., Ghozlani, W., et al. (2009). "Measurements of tangential momentum accommodation coefficient for various gases in plane microchannel." *Physics of Fluids (1994-present)* 21(10): 102004.
- Rojas-Cárdenas, M. (2012). *Temperature Gradient Induced Rarefied Gas Flow*, Ecole Polytechnique Universitaire de Marseille.
- Rojas-Cárdenas, M., Graur, I., Perrier, P., et al. (2013). "Time-dependent experimental analysis of a thermal transpiration rarefied gas flow." *Physics of Fluids (1994-present)* 25(7): 072001.
- Rojas-Cárdenas, M., Graur, I., Perrier, P., et al. (2015). "A new method to measure the thermal slip coefficient." *International Journal of Heat and Mass Transfer* 88: 766-774.
- Sharipov, F. (2003). "Application of the Cercignani–Lampis scattering kernel to calculations of rarefied gas flows. II. Slip and jump coefficients." *European Journal of Mechanics - B/Fluids* 22(2): 133-143.



# Résumé

Cette thèse présente une étude numérique et expérimentale d'écoulements gazeux raréfiés confinés, induits par gradients thermiques. L'écoulement d'un gaz raréfié peut en effet être généré en appliquant uniquement un gradient tangentiel de température le long d'une paroi. Ainsi, sans gradient initial de pression, le gaz peut se déplacer de la région froide vers la région chaude. Ce phénomène, appelé transpiration thermique, est à la base du fonctionnement des pompes dites de Knudsen, capables de générer un pompage du gaz sans utiliser de pièces mécaniques mobiles. L'apport principal de ce travail est relatif à l'investigation numérique de l'écoulement de transpiration thermique dans trois nouvelles configurations de pompe Knudsen. Dans ce but, une méthode numérique de simulation d'écoulements dans le régime de glissement a été développée ; elle implémente des conditions aux limites de saut de vitesse et de température spécifiques dans un code CFD commercial. Parallèlement, un code DSMC a été mis en œuvre pour étudier des écoulements plus fortement raréfiés dans les géométries les plus complexes. Des écoulements de transpiration thermique générés dans des canaux courbés, dans des canaux convergents/divergents ou entre deux surfaces spécialement micro-texturées ont ainsi été étudiés. D'autre part, l'analyse expérimentale d'un écoulement de transpiration thermique dans un microtube de section circulaire a été réalisée sur un nouveau banc d'essais conçu pour être adaptable à diverses géométries de canaux ou de pompes Knudsen.

**Mots-Clés:** Microfluidique, micro-écoulements gazeux, transpiration thermique, pompe Knudsen, CFD, DSMC

